Alma Mater Studiorum – Università di Bologna

DOTTORATO DI RICERCA IN

Scienze ambientali: tutela e gestione delle risorse naturali

Ciclo XXIV

Settore Concorsuale di afferenza: 03/A1 - CHIMICA ANALITICA

Settore Scientifico disciplinare: CHIM/01 - CHIMICA ANALITICA

TITOLO TESI

Pyrolysis of peptides and proteins. Analytical study and environmental applications

Presentata da: **ALESSIO ADAMIANO**

Coordinatore Dottorato **Tutor**

PROF. ENRICO DINELLI **PROF. DANIELE FABBRI**

Esame finale anno 2012

1 Introduction

1.1 Proteins

Rigid materials such as horses hooves, or like flowing hair, smooth like silk, slimy and shapeless as the egg white, inert such as cartilage or reactive such as enzymes, are all made from the same components: amino acids and proteins. This variety of features is due to structures and forms that proteins can assume in order to fulfill functions for which they were designed and synthesized by organisms. Amino acids can be bonded together in huge molecules of more than thousands of amino acidic residues. The number of proteinogenic or standard amino acids is twenty, and each one of them can be placed in every position along the peptidic chain; so for a protein made up of 100 amino acids, a number of 20 raised to the power of 100 structures are possible. Considering that the largest known protein, more precisely one of its isoforms, is made of 34,350 amino acids [1], proteins are an enormous class of molecules that can afford many functions in organisms. For instance, some proteins represent the principal constituent of structural tissues like muscles, skin, nails or hairs. Others are assigned to the transfer of certain kinds of molecule from one site to another in a living system. Others act as reaction catalyst of biochemical reaction indispensable for the sustenance of life into organisms. In order to accomplish all of these tasks, proteins assume a great variety of forms; however, they can be classified into two main groups on the base of their tridimensional structure: fibrous proteins and globular proteins. The former class is made of water insoluble proteins, mainly of animal origin, and is in turn divided into three main categories:

- *Keratins*, which form protective tissues like skin, hairs, plumages, nails and claws in animals
- *Collagens*, which form connective tissues like cartilages, tendons and blood vessels
- *Silks*, as fibroin, mostly present in arachnids and in some life stages of certain insects (e.g. larval life stages, like silkworms).

Globular proteins are a completely different class of molecules, since they are mostly water soluble, of nearly spherical shape, which fulfill a variety of biological functions (are not structural like fibrous proteins). Differently from fibrous protein, globular proteins are also present in plant organisms. They can be divided into four main categories, which are:

- *Enzymes*, which act as biological catalysts.
- *Hormones*, which are chemical messengers responsible for regulating biological processes.
- *Carrier proteins*, like hemoglobin, which carry small molecules from one place to another inside the organisms, or membrane proteins which carry molecules from the outside to the inside of cells.

- *Storage proteins*, like albumins, which are used as food and energy reserves.

The tridimensional form influences the physical and chemical properties of proteins, and is usually critical in complex mechanisms of molecular recognition, as an example between an enzyme and its substrate, or between a membrane protein and a specific ion. Different spatial arrangements of proteins are due to several factors, starting from their amino acid compositions to the way protein surfaces interact between them. The analysis of proteins structure allowed to distinguish between several hierarchic structure of a single protein, which are:

- *Primary Structure*, which is the amino acidic sequence forming the protein
- *Secondary Structure,* which depends on the geometry of the peptidic bond and on the formation of hydrogen bonds among amino acids inside the same peptidic chain
- *Tertiary Structure,* which is determined by the tridimensional form of the protein (e.g, fibrous or globular protein)

The only way to determine experimentally the secondary and tertiary structure of a protein is to perform an X-Ray diffraction analysis on its crystals. Secondary structures can be in turn divided into four main forms:

- *α-helixes*, in which all the hydrogen bonds are approximately aligned on the main axis of the helix
- *β -sheets*, in which the same peptidic chain is folded several times and the so formed peptide chains are held together by hydrogen bonds
- *α -turns* and *β-turns*, which are structural motif where the C^{α} atoms of two residues separated by few (usually 1 to 5) peptide bonds are in close approach (< 7 Å), while the corresponding residues do not form a regular secondary structure element such as an alpha helix or beta sheet [2].

The organization of a peptidic sequence to give one of this structures is due to the specific sequence of amino acids (the primary structure) and to their geometry and interactions with the other units of the protein. More in detail, this correlation among primary and secondary structures results in the possibility to predict the latter from the former by summing the free energy for such interactions, to provide an approximation for the stability of a given structure [3]. Hence, to find the lowest free energy structure from the simple sequence of amino acids results into find the most stable self-assembly secondary structure. The tertiary structure is also considered to be largely determined by the biomolecules primary structure and several structure prediction software are reported in the

literature – both for secondary and tertiary structure – that use large computational resources like those afforded by either powerful supercomputers (Blue Gene or MDGRAPE-3) or distributed computing (such as Folding@home, the Human Proteome Folding Project and Rosetta@Home). However, most of this software does rely on the comparison with data bank recording all the known protein structure (Protein Data Bank, PDB) that were determined from XRD spectra of the crystallized proteins. Some high molecular weight proteins are in the form of subunits aggregate that change the tridimensional form of each subunit, determining the *quaternary structure* of the protein, in order to fulfill different functions. This is what happens in the case of actin (figure 1.1). Despite the fact that a single molecule of actin is in globular shape, two molecules of actin can interact to form a single fibril formed by two peptidic chains twisted together and bounded with myosin [4]. This mechanism is involved in cell motility through a dynamic process driven by polymerization and depolymerization, that is, the globular to fibrous actin transition, of which structural aspects have been recently elucidated [5].

Figure 1.1. Globular and fibrous structures of a single actin molecule and a couple of molecules coupled together to give a single fibril

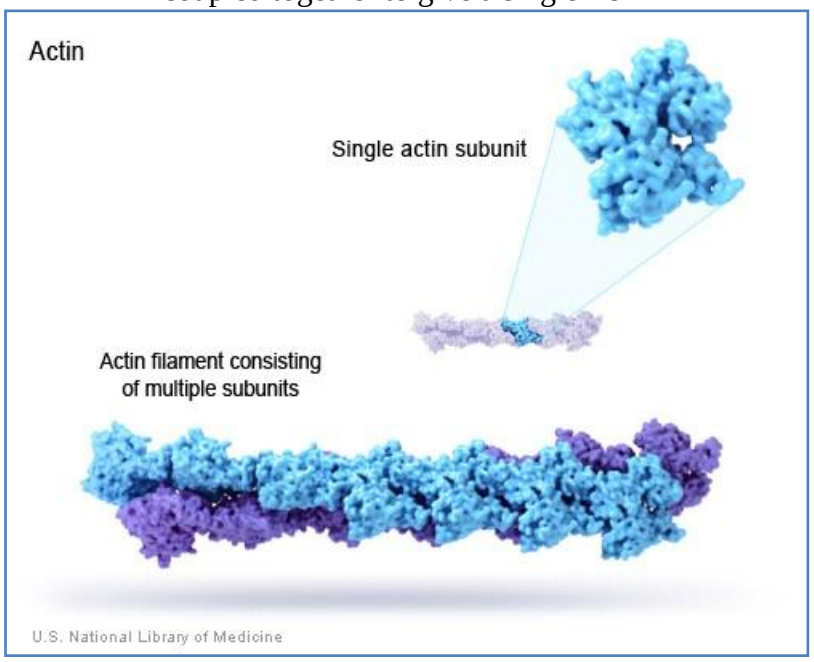

From http://www.daviddarling.info/encyclopedia

1.1.1 Intrinsecally unfolded protein or natively unfolded proteins

As a matter of fact, one of the fundamental principles in protein biology, chemistry and physics, is the structure–function paradigm for which every protein must have a certain structure in order to fulfill its function. High concentrations of strong denaturants (such as urea or guanidinium chloride)

lead to the complete disruption of all these interactions and, as a consequence, to the transformation of an initially folded protein molecule into a highly disordered random coil [6-9]. In other words, such conditions cause the complete unfolding of proteins. Reduce or completely shut down part of the conformational interactions (such as hydrogen bond or Van der Wals interactions) means that proteins will lose their biological activity, that is, they will be denatured. Denaturation is not necessarily accompanied by the complete unfolding of a protein, but rather results in the appearance of new structures with properties intermediate between those of the native and the completely unfolded states. However, a protein family of *natively unfolded proteins*, whose existence questions the paradigm structure-function, has been recently taken into account by the scientific community starting from the observation that a large proportion of gene sequences appear to code not for folded, globular proteins, but for long stretches of amino acids that are likely to be either unfolded in solution or adopt non-globular structures of unknown conformation [10].

Figure 1.2 3D structure of an intrinsically unfolded protein highly brunched [203]. From the figure are visible the terminations of several chains which can be N-terminal or C-terminal, affecting the possibility to use specific reactive (e.g. Sanger reactive) to detect the N-terminal amino acid.

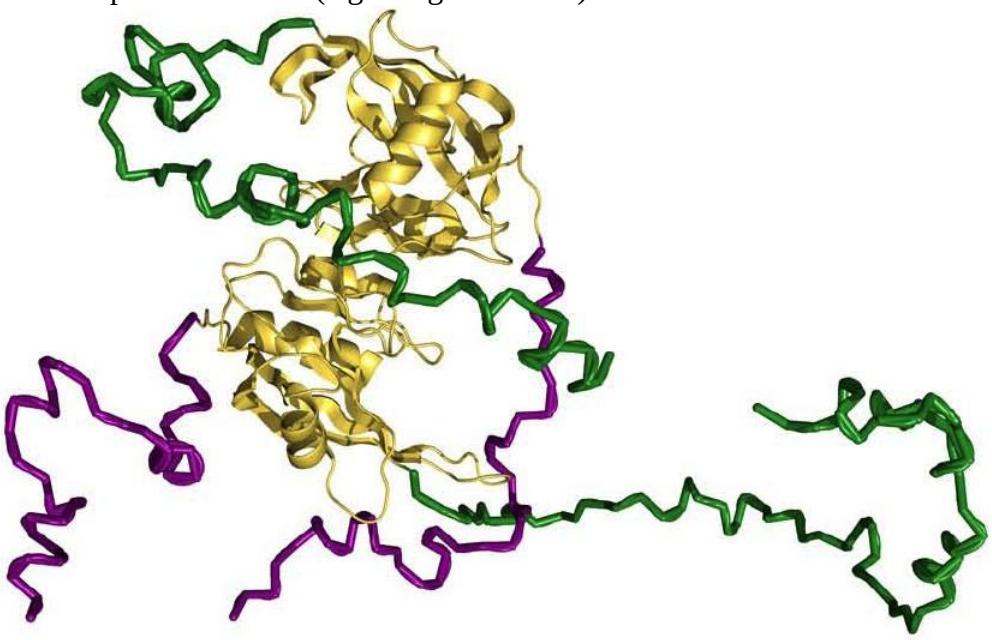

A rapidly growing set of proteins have been shown to be disordered or have profound disordered regions under physiological conditions. Native or intrinsically unfolded proteins are present in many organisms and were recognized to be involved in calcite and aragonite shell crystallization in some marine gastropods (like the pearl oyster *Pinctada fucata* and many species of the *Haliotis* genre) showing nuclein-like activity [11] and capacity to control the resulting crystal polymorph and atomic lattice orientation of the growing crystals. This properties were shown for proteins secreted by this

kind of organisms in order to regulate nacre crystallization, composed of tubular blocks of aragonite within an organic matrix that fill spaces between them [12]. The shell of bivalve mollusks was found to be composed of two distinct calcareous layers: the pigmented prismatic layer and the nacreous layer [13]. While the organic polymer matrix and the proteic composition of nacre in molluscan shell has been most extensively characterized [14], less is known about the interstitial organic sheet in the abalone species (*Haliotis* spp) which is reported to be unique to the abalone genre [11,15]. This interstitial nucleating sheet was known to be colored (green), auto-fluorescent and resistant to a wide range of denaturating agents and proteolytic enzymes. A characterization of this green polymeric interstitial sheet purified from the abalone shell was recently proposed by Falini G. et al. [16], who extracted several proteins from it. More in detail, an alkali digestion on the *Haliotis rufescens* shell was performed to extract proteins, showing the presence of a single peptide (data from polyacrylamide gel electrophoresis). All the attempts conducted to obtain information of the primary structure of GP, or even the N-terminal sequence, failed. In this work, Pyrolysis/GC-MS in the off-line configuration was used to supply information regarding the peptide molecular structure. Though this technique indicated the presence of peptide pairs of Pro with Gly, Ala, Val, Leu and Ile, it did not provide evidence of the presence of Tyr containing sequences, as suggested by the peptide amino acidic composition that reveals high content of proline, tyrosine and glycine. However, analytical pyrolysis was the only technique that provided useful information regarding the primary structure of the natively unfolded protein present in the inter-crystalline matrix of abalone shell.

1.1.2 Protein interaction with nanoparticles

Biomolecules can interact both with other macromolecules and with organic or inorganic solid surface. The interaction of proteins with solids surface has become a field of growing interest during the last years, not only for the understanding of fundamental biology phenomena, but also for high technologic applications [17, 18]. These two main topics are strictly related when speaking of nanotechnologies, which are nowadays used in a variety of technological applications including from food packaging [19] to DNA-based sensors. Nanoparticles are those particles having diameters of nanometer size (typically < 100 nm), spanning from nantoubes, nanowires, and nanofibers to fullerenes and quantum dots. Such definition includes a wide range of material with really different shapes and physico-chemical properties, as gold nanoparticles or tube nanocarbons. The increasing number of technological devices using this kind of material, hence the increasing exposure to them, posed a potential health problem for human population since nanoparticles are now applied in a series of consumer goods [20]. Growing concerns over the impact of such materials on health and the environment have initiated the first in-depth studies on the exposure effects to biological systems,

showing a high mobility of such materials in organisms or cells [21]. It must be taken into account that, beyond physico-chemical parameters of nanoparticles, toxicity was also demonstrated to be dependent on dose – in terms of critical concentration - and duration of exposure [22]. Toxic effects of nano-materials have been largely studied in the last years, and different attempts to find a correlation between adverse health effects and nanoparticles chemical composition, size and shape were made [23]. As instance, C.K. Eun and H. Myung have studied the toxicities of zinc, iron and silica nanoparticles both in vivo and in vitro [25], concluding that the low toxic effect shown by the nanoparticles was not dependent on the kind of nanoparticles or on the size, but was due to the presence of the inorganic particles themselves. On the other hand, a study made by L.K. Limach et al [21 b], in which silica nanoparticles doped with different concentrations of iron, manganese, cobalt and titanium were tested in vitro, showed chemical composition of nanoparticles to be a most decisive factor determining the formation of reactive oxygen species in exposed cells. Size-dependent cytotoxic effects were also highlighted by studies on silica amorphous nanoparticles [26] and gold nanoparticles [27]. However, the most known toxic effects due to nanoparticles exposure are that due to asbestos nanofibers. This material was in fact largely used for decades all over the word for its highly desirable properties, before the relationship between asbestos exposure and lung cancer or malign mesothelioma was discovered [28].

Figure 1.3. Silica nanoparticles imagines at transmission electron microscopy. Picture provided by Barbara Brunelli, Polytechnic University of Torino.

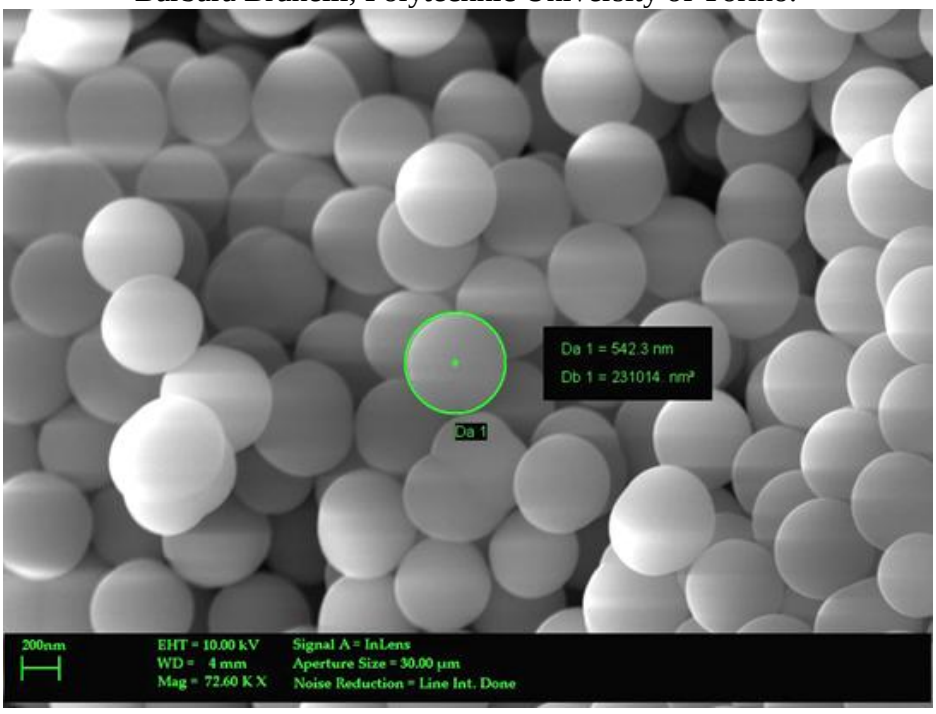

Although the role of oxygen reactive species in asbestos induced toxicity in vitro had already been discovered in the eighties [29], main aspects of the oncogenic mechanism involved are still debated [30]. Many questions arise also about the toxic effects of nanoparticles, whose dimension and uptake mechanisms by the organisms are similar. The main point seems to be the influence of the interaction protein/ nanoparticles on the exerted toxicity on cells and organisms. As an example, many contributions have been reported on the adsorption of proteins on silica nanoparticles, in order to elucidate the mechanism of protein adsorption or the interaction with cell membranes (made mainly of lipids and proteins). Bovine serum albumin (BSA) is a protein often used for studies having as main subject the investigation of nanomaterials disposition inside organisms and cell, and it is known to complex with nanomaterials such carbon nanotubes [31]. In a study by D Dutta et al [33] the importance of adsorbed proteins in guiding nanomaterials toxicity for carbon nanotubes and amorphous silica nanoparticles was investigate. This authors observed that the adsorption of BSA onto the tested materials increases the adsorption rate of the adducts inside the cell and the toxic potential for both silica and carbon adducts respect to single nanoparticles. In addition, the authors suggest that minor modification to albumin structure may result in recognition of albumin as a damaged protein form by hepatic scavenger receptors which, in attempt to eliminate the damaged protein, could "*significantly affect clearance of nanoparticles from blood and uptake into tissue*". Adsorption of proteins to solid surfaces and the conformational changes they undergo when adsorbed onto the surface of nanomaterials have been thoroughly characterized and monitored using a variety of different methods such as fluorescence, circular dichroism, infrared spectroscopy, atomic force microscopy, mass spectrometry, nuclear magnetic resonance and many others. Studies reported in the literature demonstrate that cellular responses to materials in a biological medium reflect the adsorbed biomolecule layer, rather than the material itself [34]. The nature of protein-solid surface has been shown to depend both upon nanoparticles and protein physico-chemical properties (size, superficial charge, tridimensional form, nanoparticles chemical composition). The lack of reference materials in the study field of nanoparticles toxicity brought to the development of well characterized-nanomaterials synthesis, as in the case of geoinspired synthetic chrysotile nanotubes which were deeply characterized to be proposed as a standard material to investigate asbestos interaction with biological systems [36]. In vitro toxicity tests on this material reported a remarkably difference from natural chrysotile [37] as it showed a certain degree of inactivity and so no toxic effects. Beside the absence of iron in synthetic chrysotile respect to natural one, this unexpected behavior is suggested to be also due to the regular shape and size of synthetic nanofibers. Since the Fe substitution to Si and/or Mg in the chrysotile structure can apparently determine asbestos health

hazard [38] and influence BSA or other protein adsorption on its surface, the study of this topic has become of major significance.

1.1.3 Proteins in algae

In the early 1950's, the increase in the world's population and predictions of an insufficient protein supply led to a search for new alternative and unconventional protein sources. Intense efforts have been made to explore new alternative protein sources as food supplements, primarily in anticipation of a repeatedly predicted insufficient future protein supply. Microbial protein in various forms has attracted particular attention because it is amenable to controlled intensive cultivation and is less dependent on variations in climate, weather, and soil. Algae are a traditional food complement for some people living in Mexico (*Spirulina platensis*) and in Chad (*Spirulina maxima*), as well as in Japan where most of the worldwide produced algae is consumed as health foods, food additives and feed supplements [39]. Nowadays, the commercial applications of algae for human nutrition are dominated by four strains: *Arthrospira*, *Chlorella, D. salina* and *Aphanizomenon flos-aquae* [40]. Microalgae can be also incorporated into the feed for a wide variety of animals ranging from fish (aquaculture) to pets and farm animals [40]. The 30% of the current world algal production is sold for animal feed applications and over 50% of the current world production of *Arthrospira* is used as feed supplement [39]. The potential merits of algae as a protein source are related to their ability to grow with carbon dioxide as the only carbon source and to be easily harvested; however, their growth is very slow, and the high investment costs for production in shallow artificial ponds yield lower profitability respect to open air cultivation systems [41]. Considering these features with the fact that some algae give biomasses suitable for biofuels production (e.g. lipid rich biomasses like that produced by *Nannohloropsis spp*), interest in microalgae-derived biofuels is on the rise triggered by crude oil price peaking, energy security, green-house gas emissions and competition for otherwise food-oriented agricultural commodities (e.g. sugar cane or *Zea mais* for the production of bioethanol) [42]. The potential of microalgae as a source of biofuels and as a technological solution for CO_2 fixation is subject to intense academic and industrial research. In table 1, a list of promising species for biodiesel production is reported. All this microalgae are characterized by a relative high amount of lipids and fatty acid that can be extracted and trans-esterificated with the same procedure from which biodiesel is obtained from classic energy-crops. Some algae are instead suitable for other type of biofuels production, like biohydrogen from *Chlamydomonas reinhardtii* [43] or synthesis of hydrocarbons from *Botryococcus braunii* [44]. Various conversion and extraction routes can be used for the production of liquid fuels from microalgae and biomass. For highly lipidic algae, lipid extraction, combined with transesterification for biodiesel production, allows the obtainment of a

biodiesel like fuel. Alternatively, especially for microalgae with low lipid content, or for residues from lipid extraction, thermochemical processes such as pyrolysis and hydrothermal treatment (HTT, on wet material) can produce liquid fuels by exploiting all biomass constituents, including protein [45]. This kind of treatment is supposed to produce more cost-effective biofuels since no extraction procedure is involved; however, thermal treatments produce a complex oil whose chemical composition need to be characterized. More in detail, less is known about the faith of proteins and their thermal degradation products during the thermal conversion of the biomass into an energy liquid, though proteins are known to be a great part of many algal biomasses on dry base. Only recently the attention was focused on protein fate during thermal treatments by some author [46] who characterized the nitrogen containing fraction of hydrothermal oil obtained by *Desmodesmus sp.* Another important issue involving protein in algae for biofuels production regards the recycle of nitrogen in the cultivation plants. The perspective of large scale production of microalgae for biofuel applications is motivated by the high productivity which can be reached [47, 48, 49]. Photo bioreactor productions of up to 150 tons ha^{-1} $year^{-1}$ have already been obtained and Chisti [48] suggested an upper value of 263 tons ha^{-1} $year^{-1}$. On the basis of an average composition of microalgae given by $CO_{0.48}H_{1.83}N_{0.11}P_{0.01}$ [50] the nitrogen and phosphorus requirement per unit of surface and per year can be estimated. This leads to a nitrogen amendment that varies from 8 to 16 tons N ha^{-1} $year^{-1}$. This means that microalgae intensive cultivation will involve huge quantities of nitrogen and phosphate for which environmental and economic impact may not be sustainable. A process to recycle nitrogen and phosphorus contained in algal waste after lipid extraction is therefore required in order to reduce the use of fertilizers. Anaerobic digestion can be an answer to this problem, since this biotechnological process can mineralize algal waste containing organic nitrogen and phosphorus, resulting in a flux of ammonium and phosphate that can then be used as a substrate for the microalgae [51]. Another way to minimize costs and recycle the biomass residues by means of pyrolysis is to obtain bio-char, a solid fraction produced by means of pyrolysis, in which great part of carbon, ashes and nitrogen was shown to be retained [43], in order to obtain a set of potential carbon-negative bio-fuels. Bio-char is in fact a value-added product that can be utilized as fuel or chemical adsorbent with high energy content and reactivity.

Table 1.1. Suitable microalgae species for biodiesel production [204].

Microalgal species	Lipid content (% Wg/Wg)	Lipid productivity (mg / L^{-1} d^{-1})	Natural habitat
Botryococcus spp	25.0-75.0	-	Fresh water
Chaetoceros calcitrans	14.6-39.8	17.6	Fresh water
Chaetoceros muelleri	33.6	21.8	
Chlorella emersonii	25.0-63.0	10.3-50.0	Fresh water
Chlorella protothecoides	14.6-57.8	1214	
Chlorella pyrenoidosa	2	-	
Chlorella sorokiniana	19..-22.0	44.7	
Chlorella vulgaris	5.0-58.0	11.2-40.0	
Chlorella spp	10.0-57.0	18.7-42.1	
Chlorococcum spp	19.3	53.7	Fresh water
Dunaliella primolecta	23.1	-	Fresh water
Dunaliella salina	6.0-25.0	116	
Dunaliella tertiolecta	16.7-71.0	-	
Dunaliella spp.	17.5-67.0	33.5	
Ellipsoidion spp.	27.4	47.3	Fresh water
Haematococcus pluvialis	25	-	Fresh water
Isochrysis galbana	7.0-40.0	-	Sea water
Isochrysis spp.	7.1-33.0	37.8	
Nannochloris spp.	20.0-56.0	60.9-76.5	Sea water
Nannochloropsis oculata	22.7-29.7	84.0-142.0	Sea water
Nannochloropsis spp.	12.0-53.0	60.9-76.5	
Neochloris oleoabundans	29.0-65.0	90.0-134.0	Sea water
Pavlova salina	30.9	49.4	Sea water
Pavlova lutheri	35.5	40.2	
Phaeodactylum tricornutum	18.0-57.0	44.8	Sea water
Scenedesmus obliquus	11.0-55.0	-	Fresh water
Scenedesmus quadricauda	1.9-18.4	35.1	
Scenedesmus sp.	19.6-21.1	40.8-53.9	
Spirulina platensis	4.0-16.6	-	Sea water

1.2 Pyrolysis

Pyrolysis is a method for thermochemical conversion of biomass into a liquid fuel, called bio-oil, biocrude or tar. Fast pyrolysis has been shown to be a facile and inexpensive method to produce high yields of liquids (pyrolysis oil) from lignocellulosic biomass; however, most pyrolysis oils are low quality fuels that are immiscible with hydrocarbons because, like their parent biomass, they are highly oxygenated. In fact, bio-oil is a complex mixture containing various organic compounds which are formed by thermal degradation of cellulose, hemicellulose, lignin and other bio-molecules originally present in feedstock. These compounds affect fuel characteristics and eco-toxicological risks of the bio-oil. For instance, acidic components (e.g. acetic acid and phenols) are mainly

responsible of corrosion, polyhydroxylated compounds (e.g. levoglucosan) affect solubility in conventional fuels and reactive aldehydes affect long-term stability and aging of the pyrolysis liquid. Pyrolysis of different crops has been widely investigated over the last decades. For such a complex matrices, a rapid and reliable analytical methodology capable to provide preliminary chemical information on the pyrolysis product yield and composition is therefore desirable. For this purpose, the contribution of analytical pyrolysis combined with on-line GC separation (Py-GC) – a simple and reliable micro-scale model of the fast pyrolysis process – is well recognised to gather insights and preliminary information on potential compounds derived from bio-oil. This is also valid for bio-oil produced from biomass with high protein content. Protein amount inside raw biomasses does not appear to be a major factor in the ratio of pyrolysis oil, bio-char, and noncondensable gas pyrolysis products or the distribution of biomass carbon into those products [52]. However, the presence of protein was shown to have a large effect on the fate of oxygen contained within the biomass, which can be converted to water or can remained bound to carbon in oxygenated organics in the pyrolysis oil. The presence of proteins in the raw biomass is suggested to facilitate deoxygenating mechanism of the bio-oils through reactions of nucleophilic amine groups with electrophilic groups, which result into release of water, improving the characteristics of bio-oils such as heating value, pH and thermal stability. The number of studies regarding thermochemical conversion of protein rich biomasses is increasing. As already mentioned, algae are now considered to be the most promising for the production of bio-fuels, due to the emerging possibilities to cultivate them in marginal areas unsuitable for agricultural purposes (e.g. desert and seashore lands), in non-potable water or even as a waste treatment purpose, using far less water than traditional crops and do not displacing food crop cultures [53]. Recently, the route of pyrolysis for the production of feedstock and fuel from red and brown marine macroalgae was also evaluated in a study by Yoon Ju Bae et al [54]. The protein content of these algae, including various amino acids, ranges from 7-16 % for red algae and from 21–47% of weight on dry base for brown algae. Since thermal treatments are largely recognized as being the most rapid and inexpensive methods for biofuels production from such biomasses, the understanding of proteins and amino acids thermal degradation and the characterization of their pyrolysis products has become a central issue. Analytical pyrolysis, which is based on the controlled thermal degradation of the sample, is well established as a technique for the direct and reproducible analysis of macromolecules of natural origin. There have been several reports of production of pyrolysis liquids from higher protein or nitrogen containing feedstocks including algae biomass [55] chicken litter [56] and other biomasses, though none have focused on the differences in chemical or physical characteristics related to the presence of the nitrogen. Though several studies on pyrolysis of amino acids are reported [57-60], no reviews are available in the current literature on the pyrolysis

of different proteins. Thermal behavior of amino acids and protein was shown to be dependent upon temperature [61] and on peptidic bonds [62]. For example, at low temperatures (200–300 ◦C), low molecular weight heterocyclic compounds are generally observed [57, 58], although at pyrolysis temperatures above 500 ◦C, polynuclear aromatic compounds (PACs) including nitrogen containing PACs are observed [63]. However, there have been no systematic studies on the effects of pyrolysis conditions, such as temperature, residence time, and the structure of the substrate, on the product distribution. Common reactions of amino acids under pyrolysis are dehydration, decarboxylation and deamination, although the extent of these reactions is dependent on structure [64].

2,5-diketopiperazine or DKPs have been reported as typical pyrolysis products of proteins and were exploited as specific markers of proteins in complex matrices analysed by Py-GC-MS for applications in forensic science [96, 200], archaeology [176] and biology [198]. DKPs are the simplest cyclic dipeptides retaining the side chain of the parent amino acids that could be separated and detected by conventional GC-MS technique. On this ground pyrolysis followed by GC-MS analysis was proposed almost forty years ago as a method of protein sequencing [89]. The same approach with modern MS techniques was recently revisited and extended to cyclic oligopeptides produced by pyrolysis of linear peptides ([91] and references therein). It is worth noting that among the 210 possible DKPs resulting from the combination of any two of the 20 common protein amino acids, very few have been detected in thermally treated proteins.

1.3 DKPs

Cyclic dipeptides of natural α-amino acids corresponding to 2,5-diketopiperazines (DKPs) are naturally occurring substances isolated from living organisms, or have been purposely synthesised as potential drug candidates due to their biological activity [70,71]. Their structure contains two hydrogen bond accepting centers and two hydrogen donating sites, which are often necessary for potential interactions with biological systems (figure 1.4).

Figure 1.4 DKPs structure. R_1 and R_2 indicate the lateral chains of the parent amino acids.

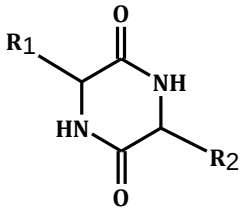

On the other hand, they are conformationally restrained by the presence of a six-membered ring with side chains that are orientated in a spatially defined manner, allowing to make easy and accurate

conformational predictions of their structure. In contrast to classical linear peptides, DKPs are very stable to hydrolysis and proteolysis, a very important feature when designing potential lead structures [206]. DKPs comprise a novel family of signaling compounds, identified in cell-free supernatants of several gram-negative cultures. Bacteria communicate with each other by a process termed "quorum sensing" (QS), and diffusible, low-molecular-weight chemicals, like DKPs, are used as the communication languages. The peculiar heterocyclic system found in several natural products constitutes a rich source of new biologically active compounds [72]. The wide spectrum of their biological properties points to various therapeutic possibilities [66]. The precise role played by DKPs in bacterial cell-to-cell communication has yet to be established. Interesting biological properties were observed for cyclic peptides containing tyrosine, such cyclo(L-Phe-L-Tyr) [67]. Studies showed that some DKP are able to bind m-opioid receptors [68]. An additional example of the recognition and metabolisation of cyclic dipeptides by enzymes was demonstrated with tyrosine hydroxylase, which catalyses the limiting step in catecholamine biosynthesis [71]. Due to their chiral, rigid and functionalised structure, DKPs can bind to a large variety of receptors with high affinity, giving a broad range of biological activities. The combinatorial use of natural and unnatural amino acids can give rise to a library of compounds that may contribute to an understanding of the structural requirements for receptor interactions, allowing the validation of molecular targets and opening new perspectives for drug discovery processes [67]. Simple DKPs have been shown not only to exist alone or as a part of larger more complex molecules, but also to be enzymatically synthesized in several members of the protist and plant kingdom. Although cyclic dipeptides are ubiquitous in nature, very few of these molecules have been tested and only four are known to exhibit any biologic activity in mammals. These include cyclo(His-Pro), cyclo(Leu-Gly), cyclo(Tyr-Arg), and cyclo(Asp-Pro) [69]. Among them, only cyclo(Hyp-Pro) has been shown to be present in mammals. However, there are several molecules containing a six member ring like that of 2,5-diketopiperazine, whose biological activity has been largely investigated, like the gliotoxins and sporidesmins (which showed antiviral properties) and bycyclomicin (antibiotic properties). In table 1.2 is reported a list of natural occurring DKPs.

Table 1.2 Natural occurring DKPs.

Diketopiperazine	Species	Family
cyclo(Pro-Leu)	*Rosellina necatrix*	Fungus
	Aspergillus fumigates	Fungus
cyclo(Pro-Val)	*Rosellina necatrix*	Fungus
	Aspergillus ochraceus	Fungus
	Metarrhizum ansiopha	Fungus
cyclo(Pro-Phe)	*Rosellina necatrix*	Fungus
cyclo(Phe-Phe)	*Pennicillum nigricans*	Fungus
	Streptomyces noursei	Fungus
cyclo(Ala-Leu)	*Aspergillus niger*	Fungus
cyclo(Pro-Tyr)	*Alternaria alternata*	Fungus
cyclo(Ser-Ser)	*Streptomyces orchidaceus*	Actinomycetes
cyclo(Pro-Trp)	*Pennicillum brevicompactum*	Fungus
cyclo(Ala-N-methyl-Leu)	*Beauveria nivea*	Fungus

Some of the chemical properties of 2,5-diketopiperazines are very interesting for medicinal chemistry, such as resistance to proteolysis and mimicking of peptidic pharmacophoric. Groups, substituent group stereochemistry (defined and controlled in up to four combinations), conformational rigidity, and donor and acceptor groups for hydrogen bonding (favoring interactions with biological targets). Favorable pharmacodynamic and pharmacokinetic characteristics are acquired by the compounds through these properties, leading to promising agents for the development of new drugs [72 b,74]. Diketopiperazines are privileged structures for the discovery of new lead compounds by combinatorial chemistry and are considered ideal for the rational development of new therapeutic agents [1,2].

Besides to be deliberately bio/synthesised, DKPs are unintentionally formed upon thermal treatment of organic matter containing amino acids, peptides or proteins. For instance, several DKPs were detected in foodstuff and beverages such as coffee [75] and cooked meat [76,77] where they are believed to be responsible of their bitter taste. DKPs were detected among the hundreds of compounds in the water-soluble condensate of cigarette smoke [6]. Furthermore, DKPs were assumed to be precursors of toxic nitrogen-containing gases from the pyrolysis and combustion of biomass containing proteins [92,79], and were identified as main nitrogen-containing compounds in the oil obtained from pyrolysis and liquefaction of microalgae [43,46]. Investigations based on analytical pyrolysis, especially when combined with gas chromatography and/or mass spectrometry (Py-GC-MS, Py-MS), have largely contributed to our knowledge on the thermal formation of DKPs from amino acids and related compounds. Py-GC-MS studies showed that DKPs could be produced from the pyrolysis of single α-amino acids [57,60]. Derivatized DKPs were detected when pyrolysis

of α amino acids was conducted under methylating [80-82] or silylating [58] conditions. The condensation in the melt of amino acids into the corresponding dipeptides, that in turn underwent cyclisation with elimination of water, was proposed to explain the pyrolytic production of DKPs from amino acids [62,84]. The formation of DKPs from several dipeptides was observed in mass spectrometers [84] and then investigated by Py-GC-MS [83]. A systematic study on the thermal formation of DKPs from peptides was conducted by Voorhees and co-workers by Curie-point Py-MS of glycyl dipeptides from the natural 20 amino acids [85] and other dipeptides [86] as well as of oligopeptides with 3-6 amino acid residues [87]. This latter work confirmed that DKPs could be formed from the cyclisation reactions of internal amino acids joined through a peptidic bond. Notably most of them contained the Pro residue [76]. This is probably due to the fact that Pro promptly yields DKPs upon heating [59] and DKPs from Pro are considered rather stable [70]. Py-GC-MS studies confirmed that the formation of DKPs was found to be favored from dipeptides containing Pro [83]. These authors showed that the DKP formation was favored when Pro was the N-terminal group in the case of Pro-Val, probably because the bulky side chain inhibited the back reaction leading to the peptide. Most of the above quoted studies dealt with DKPs from neutral amino acids. There are few detailed investigations on the occurrence of DKPs from the thermal cyclisation of peptides containing Pro and an amino acid with an ionisable side chain [88]. Results from Py-MS analysis of glycyl dipeptides suggested that the formation of DKPs could be inhibited when the amino acid is one of the five amino acids described as the most hydrophilic that is aspartic and glutamic acids, asparagine, arginine, lysine [85]. This observation might explain the fact that the DKPs identified in foods contained chiefly non polar residues [75-77]. However, it should be pointed out that DKPs with a polar/ionisable side chain might elude GC-MS detection unless properly derivatised. Silylation has not been widely investigated in the case of DKPs [89], probably because the insertion of the bulky TMS group into a hindered DKP is difficult to achieve [81]. On the other hand, the thermal degradation products of amino acid containing a polar chain, such as glutamic acid, are largely studied since they are ubiquitous in proteins and their pyrolysis products were proven to be toxic on human [63].

2. Aim of the thesis

The scope of this thesis was the development of a quali-quantitative analytical method in off-line pyrolysis focused on protein thermal degradation products for applications in different research fields of environmental interests. Particular attention was given to cyclic dipeptides, 2,5-diketopiperazines abbreviated as DKPs, which are characteristic markers of the thermal degradation of proteins specific of adjacent amino acid sequences in the peptide chain. There are few methods reported in the literature regarding the analysis of DKPs thermally produced from proteins, therefore a procedure was developed based on analytical flash pyrolysis combined with gas chromatography-mass spectrometry (GC-MS). The procedure was developed through the analysis of model compounds: linear dipeptides and proteins such as albumin, collagen (chapters 3 and 4). The information gathered on the formation and GC-MS characteristics of DKPs were applied to determine DKPs in the pyrolysates of proteinaceous materials in studies regarding:

- Chemical characterization of third generation potential biofuels produced from the pyrolysis of microalgae biomass *(Botryococcus braunii*, *Nannochloropsis gaditana* and *Desmodesmus communis*).
- Protein surface interaction with nanomaterials (Bovine serum albumin interaction with stoichiometric synthetic chrysotile at different iron concentration).
- Collagen preservation in archaeological bones from Vicenne necropolis (Molise – Italy).
- Intrinsecally Unfolded Protein (IUP) in *Haliotis rufescens* (red abalone) shell .

The obtained results are reported and discussed in chapter 5.

Chapter 3

Development of analytical methods for proteins pyrolysis

3.1 Materials

Solvents:

- Acetonitrile (ACN) - Sigma Aldrich
- Ethyl acetate (EtAc) - Sigma Aldrich
- Methanol (MTL) - Sigma Aldrich
- Di-chloro-methane (DCM) - Sigma Aldrich
- Hexane (HEX) - Sigma Aldrich
- Acetone - Sigma Aldrich

Adsorbent phases:

- Silica gel
- Activated carbon
- XAD-2 resin (styrene/divinylbenzene – Supelco) 90 Å mean pore size
- XAD-4 resin (styrene/divinylbenzene – Sigma-aldrich) 40 Å mean pore size
- XAD-8 resin (methyl/methacrylate ester – Sigma-aldrich) 25 µm mean pore size

Standards:

- cyclo Gly-Leu - Sigma Aldrich
- cyclo Gly-Val - Sigma Aldrich
- cyclo Phe-Ser - Sigma Aldrich
- cyclo Ala-Ala - Sigma Aldrich
- sarcosine anhydride (SARC) - Sigma Aldrich
- 1,3 benzyl-oxo-piperazine (OPI) - Sigma Aldrich
- pyroglutamic acid - Sigma Aldrich

Linear dipeptides:

- Lysine-Proline-Lecuine (KPL) – synthesized
- Glutamic acid-Proline-Leucine (EPL) – synthesised
- Proline-Leucine (PE) – GenScript inc. (USA)
- Proline-Glutamine (PQ) – GenScript inc. (USA)

- Proline-Aspartic acid (PD) – GenScript inc. (USA)
- Proline-Asparagine (PN) – GenScript inc. (USA)
- Proline-Tyrosine (PY) – GenScript inc. (USA)
- Proline-Arginine (PR) – GenScript inc. (USA)
- Glutamic acid-Glutamic acid (EE) – GenScript inc. (USA)
- Aspartic acid-Aspartic acid (DD) – GenScript inc. (USA)
- Glutamic acid-Aspartic acid (ED) – GenScript inc. (USA)
- Aspartic acid-Glutamic acid (DE) – GenScript inc. (USA)
- Glycine-Aspartic acid (GD) – GenScript inc. (USA)
- Glycine-Glutamic acid (GE) – GenScript inc. (USA)
- Tyrosine-Tyrosine (YY) – GenScript inc. (USA)
- Glycine-Serine (GS) – GenScript inc. (USA)

Proteins

- Bovine Serum Albumin (BSA) – Sigma-Aldrich
- Collagen (COL) – Sigma-Aldrich
- Ovalbumin (OVA) – Sigma-Aldrich
- Lysozyme (LSZ) – Sigma-Aldrich

Reagents:

- Trimethylchlorosilane (TMCS) - Sigma Aldrich
- Pyridine (PDN) - Sigma Aldrich
- Triethylamine (TEA) - Supelco
- Imidazole (IMD) - Supelco
- bis-trimethysilyl trifluoracetamide (BSTFA) + 1% of tetramethyl-chloro-silane (TMCS)
- trimethyl-amonium-hydroxide (TMAH) – Sigma Aldrich
- Phosphate buffer pH = 7.4

Mineral phases:

- Synthetic chrysotile nanotubes
- Synthetic chrysotile nanotubes Fe doped at 0.57% and 1.78% (w_g/w_g %)

3.2 Instruments

Analytical pyrolysis

A pyroprobe model 1000 (CDS Analytical Inc.) was utilized in on-line (Py-GC-MS) and off-line pyrolysis experiments. Figure 3.1 depicts the procedure of off-line pyrolysis that was optimized as described in sections 3.3, 3.4 and 3.5.

Figur 3.1. Off-line pyrolysis

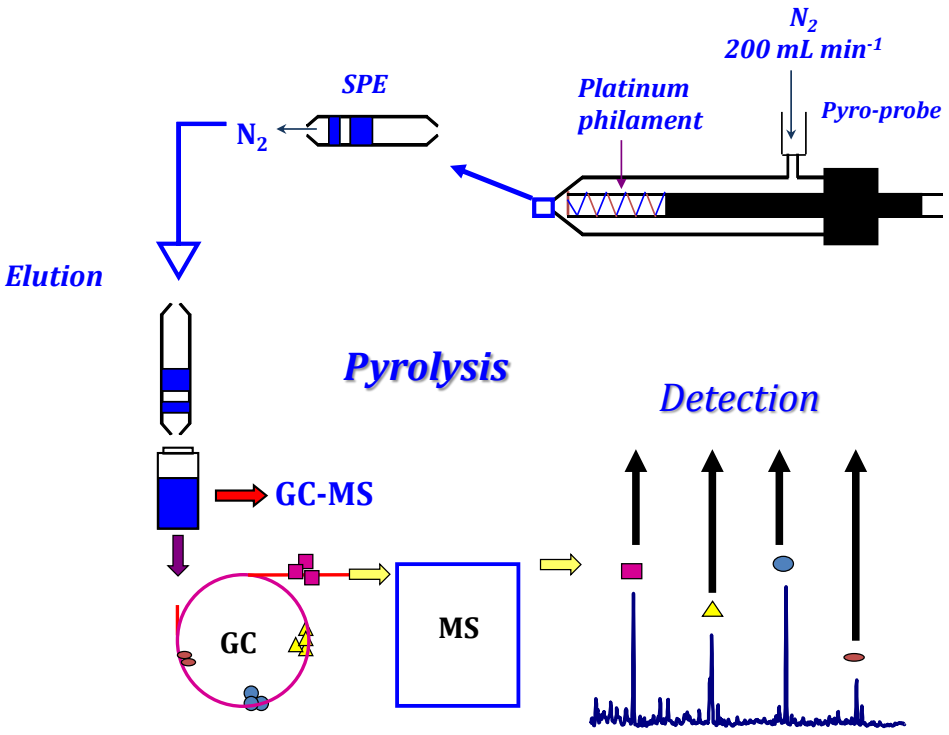

Bench scale pyrolysis reactor

The configuration of the fixed bed reactor set up for preparative pyrolysis consisted of a tubular quartz reactor (length: 650 mm, internal diameter: 37 mm) placed coaxially within a furnace refractory (Carbolite, Italy), equipped with a thermocouple, connected to the nitrogen inlet by means of pressure valve and a flow meter and connected downstream to an ice trap and a solvent trap (acetone) for trapping condensable compounds. The sample was uniformly placed onto a sliding quartz boat, the nitrogen flow was set at 1000 mL / min and the oven was turned on. As soon as the temperature inside the reactor reached the established value (500 °C, measured temperature), the sample was positioned into the central part of the oven for 5 min, then retrieved upstream in the colder part of the reactor. The bio-oil recovered in both traps was dissolved into acetone.

Elemental analysis

Carbon, hydrogen, and nitrogen content analysis was performed using a microelemental analyzer (LECO CHN-600), oxygen content of samples was calculated by difference between 100% and sum of carbon, hydrogen, nitrogen and ash.

FT-IR

FTIR spectra of samples in KBr disks were collected at room temperature by using a FTIR Nicolet 380 Thermo Electron Corporation working in the range of wavenumbers 4000–400 cm^{-1} at a resolution of 2 cm^{-1}. A finely ground, approximately 1% (w/w) mixture of the sample in KBr was pressed into a transparent disk using a hydraulic press and applying a pressure of 48.6 tsi (670.2 MPa).

TGA

Thermogravimetric investigations were carried out on dried samples using a TA instrument. Heating of samples (weight ranging from 1 to 5 mg) was performed in flowing nitrogen (100 cm^3 min^{-1}) using a ceramic crucible.

XRD diffractometer

X-ray powder diffraction patterns were collected using a PanAnalytical X'Pert Pro equipped with X'Celerator detector powder diffractometer using Cu Kα radiation generated at 40 kV and 40 mA. The diffraction patterns were collected within the 2θ range from 10° to 60° with a step size (Δ2θ) of 0.02° and a counting time of 1200 s. The instrument was configured with a 1/16° divergence and 1/16° antiscattering slits. A standard quartz sample holder 1 mm deep, 20 mm high and 15 mm wide was used.

3.3 Procedure optimization - methods

In the start up, the analytical method was developed on the pyrolysis of bovine serum albumin and proline-alanine. The pyrolysis was used both in on-line and in off-line configurations. For the former, several adsorbent phases together with different eluent phases and pyrolysis temperature were tested in order to achieve the highest recovery of pyrolysis products.

The tested eluent phases were:

- Methanol (MT)
- Di-chloro-methane (DCM)
- Acetonitrile (ACN)

The tested adsorbent phases were:

- Silica gel
- Activated carbon
- XAD-2 resin (styrene/divinylbenzene) 90 Å mean pore size
- XAD-4 resin (styrene/divinylbenzene) 40 Å mean pore size
- XAD-8 resin (methyl/methacrylate ester) 25 µm mean pore size

A thermocouple (Delta OHM HD 2108.1 - TersidS.r.l.) was used to measure the real temperature (Tm) inside the quarz tube placed into the platinum coil and pyrolysed at five set temperatures (Ts) in the 350°C-880°C range. The following calibration curve (figure 3.2) was obtained:

- Tm = 0.73 Ts + 60 (R2 = 0.998).

Figure 3.2. Curve obtained matching set temperatures with temperature detected by means of a thermocouple placed in a quartz tube (sample holder) filled with quartz wool.

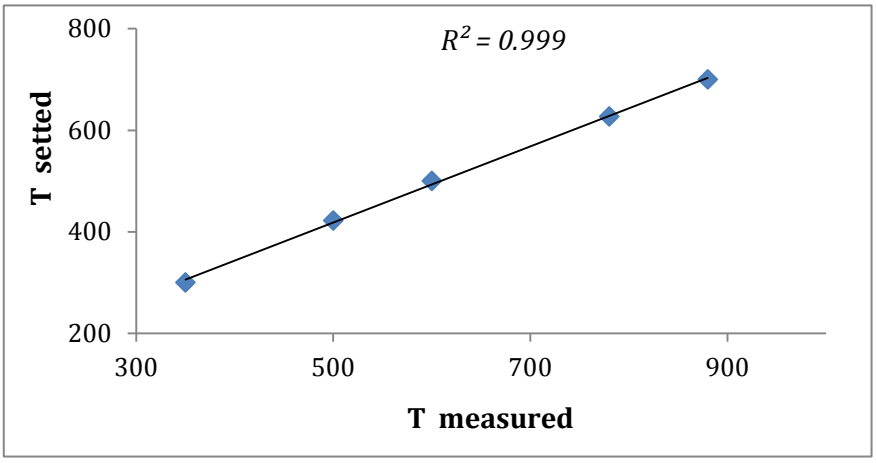

The solutions were collected, concentrated under a gentle nitrogen stream and spiked with sarcosine anhydride (internal standard) solution in acetonitrile before being analyzed in GC-MS.

Response factors were calculated by the formula :

Fr = Ax*Qsi/Asi*Qx)

Ax = Peak area of the standard 2,5-diketopiperazine (DKPs)

Asi = Peak area of the internal standard (Sarcosine anhydride)

Qsi = Quantity of internal standard

Qx = Quantity of the standard 2,5-diketopiperazine (DKPs)

The response factors were calculated for the underivatized and silylated DKPs (Rf / Rf silylated derivatives), from standard solutions of:

- Alanine anhydride (Rf = 2.5 / 1.3)

- cyclo (Glycine-Valine) (Rf = 3.0 / 1.2)
- cyclo (Glycine-Leucine) (Rf = 4.1 / 0.8)
- cyclo (Serine-Phenilalanine) (Rf = 5.0 / 1.5)

3.4 Model pyrolysis procedure (off-line)

In off-line experiments the pyrolyser probe containing the quatz sample tube was inserted into a glass pyrolytic chamber. The exit was connected through a Tygon tube to a cartridge containing an adsorbent phase. The apparatus was fluxed with a nitrogen stream (200 cm^3 min^{-1}) measured at room temperature and pressure for few seconds, then the sample (typically from 3 to 5 mg) was pyrolysed at the tested set temperatures for 100 s at the maximum heating rate (20 °C ms^{-1}) under nitrogen flux. After pyrolysis, the pyrolysis chamber was filled with 5 mL of eluent allowing the solution to pass slowly through the cartridge. The obtained solution was spiked with 0.1 mL of a 250 mg L^{-1} acetonitrile solution of internal standard and directly analysed. An aliquot (0.1 mL) of this solution was added with 0.1 mL of 250 mg of silylation internal standard, 50 μL of silylating agent and 50 μL of catalyst, then heated at 70-80°C for 3 hours.

Off-line GC-MS analysis

Sample solutions were injected under splitless conditions into the injector port of an Agilent 6850 gas chromatograph connected to an Agilent 5975 quadrupole mass spectrometer. Analytes were separated by a DB-5HT (Agilent Technology) fused-silica capillary column (stationary phase poly (5% diphenyl/ 95% dimethyl) siloxane, 30 m, 0.25 mm i.d., 0.25 μm film thickness) using helium as carrier gas (at constant pressure, 33 cm s^{-1} linear velocity at 200 °C), with the following temperature programs: from 50 °C to 300 °C (held 5 min) at 5°C min^{-1} for the underivatized solutions, and from 100°C (held 5 min) to 310°C at 5°C min^{-1}, for the silylated solutions. The injection port was maintained at 260°C. Mass spectra were recorded in the full scan acquisition mode under electron ionisation (70 eV) at 1 scan s^{-1} in the 35–650 m/z range.

3.5 Eluent and adsorbent phases test

Arbitrary pyrolysis set temperature (700°C) and adsorbent phase (XAD-2 cartridge) were chosen in the start up of the procedure optimization in order to identify the best elution phase for the BSA pyrolysis products. From 5 to 10 mg of pure BSA were pyrolysed as described above. Two pyrolysis (n=2) were performed for each tested solvent (ACN, MT and DCM). The cartridge was eluted with 5 mL of solvent and then an aliquot of the obtained solution was concentrated under a gentile nitrogen stream, spiked with internal standard and analysed in GC-MS. Quantitative analysis of DKPs was

achieved from underivatized solutions. The mean values (n=2 replicates) of the recovery yields for all the tested solvents are reported in table 3.1.

Table 3.1. DKPs yields obtained from pyrolysis at 700°C of BSA after elution with different solvents.. Values are reported as percent yields calculated as Wg_{dkp} / Wg_{sample} *100.

	ACN (n=2)		**MT (n=2)**		**DCM (n=2)**	
	(g/g %)	**RSD**	**(g/g %)**	**RSD**	**(g/g %)**	**RSD**
diketodipyrrole	0.04	18	0.03	8	0.04	20
cyclo(Pro-Ala) 1	0.07	15	0.05	35	0.06	15
cyclo(Pro-Ala) 2	0.08	12	0.03	29	0.05	13
cyclo(Pro-Gly)	0.08	18	0.04	34	0.06	5
cyclo(Pro-Val) 1	0.17	16	0.11	14	0.12	6
cyclo(Pro-Val) 2	0.21	17	0.12	18	0.14	6
cyclo(Leu-Leu)	0.10	12	0.06	27	0.07	5
cyclo(Pro-Pro)	0.05	14	0.02	26	0.03	4
cyclo(Pro-Ile)1	0.07	19	0.04	26	0.05	12
cyclo(Pro-Ile)2	0.03	12	0.02	25	0.02	20
cyclo(Pro-Leu)1	0.70	14	0.38	22	0.47	4
cyclo(Pro-Leu)2	0.51	7	0.42	22	0.49	5
TOTAL	**2.1**		**0.90**		**1.12**	

Since acetonitrile gave the highest yields together with acceptable RSD values (table 3.1), and no loss of analytes was noticed by comparison with on-line pyrogram of BSA, it was chosen as eluent phase. The second optimization step was focused on the adsorbent phase choice.

The same pyrolysis temperatures and parameters, excepted for ACN as eluent phase, chosen to test the solvent were used for the cartridge evaluation. The yields reported in table 3.2 indicate activated carbon was not a suitable material (no DKPs were detected), while silica provided lower values than all the tested XAD resins. In particular XAD-8 resin showed the greatest yields but the lowest precision (high RSD values especially for diketodipyrrole and cyclo(Pro-Ala)). At last, XAD 2 was selected also because was the less contaminated among the tested adsorbent phases (e.g. phenol, 2,4-di-tert-butyl was a common interferent).

Table 3.2. DKPs yields obtained from pyrolysis at 700°C of BSA and trapped with different adsorbent phases (elution with acetonitrile). Values are reported as percent yields calculated as Wg_{dkp} / Wg_{sample} *100.

	XAD-2 (n=2) (g/g %)	RSD	XAD-4 (n=2) (g/g %)	RSD	XAD-8 (n=2) (g/g %)	RSD	Silica (n=2) (g/g %)	RSD	Active carbon
diketodipyrrole	0.04	18	0.06	19	0.084	27	0.041	65	-
cyclo(Pro-Ala) 1	0.07	15	0.075	36	0.084	12	0	141	-
cyclo(Pro-Ala) 2	0.08	12	0.11	46	0.14	28	0.011	137	-
cyclo(Pro-Gly)	0.08	18	0.086	64	0.077	81	0	-	-
cyclo(Pro-Val) 1	0.17	16	0.2	29	0.26	16	0.1	25	-
cyclo(Pro-Val) 2	0.21	17	0.25	35	0.33	16	0.045	28	-
cyclo(Leu-Leu)	0.10	12	0.1	33	0.084	134	0.044	53	-
cyclo(Pro-Pro)	0.05	14	0.054	32	0.074	14	0.01	10	-
cyclo(Pro-Ile)1	0.07	19	0.055	84	0.041	15	0.029	7	-
cyclo(Pro-Ile)2	0.03	12	0.021	141	0.089	52	0.45	8	-
cyclo(Pro-Leu)1	0.70	14	0.65	36	1	12	0.38	26	-
cyclo(Pro-Leu)2	0.51	7	0.64	13	0.82	16	0.33	8	-
TOTAL	**2.1**		**2.0**		**3.1**		**1.4**		**0**

3.6 Pyrolysis temperature test

In order to maximize DKPs formation from protein pyrolysis, several pyrolysis temperature for several model compounds were tested. Three model compounds – a globular protein, a fibrous protein and a linear dipeptide – were pyrolysed in the pyrolysis temperature range of 300-700°C to evaluate the relation between DKPs formation and pyrolysis temperature. The model compounds on which this relation was investigated are:

- Bovine serum albumin (Sigma Aldrich)
- Collagen (Sigma Aldrich)
- Proline-Alanine dipeptide (sigma Aldrich)

The principal peaks of each pyrolysates pattern were quantify using sarcosine anhydride as internal standard and the response factor of cyclo(Glycine-Valine) (Fr = 3.0). The yields of DKPs are reported in figures 3.3, 3.4 and 3.5 respectively for collagen, albumin and Pro-Ala. The results show that the highest yields were obtained pyrolysing the samples at 500°C. Thus this pyrolysis temperature was selected in all the off-line experiments.

Figure 3.3. DKPs percent mass yields evolved from collagen pyrolysed at different temperatures

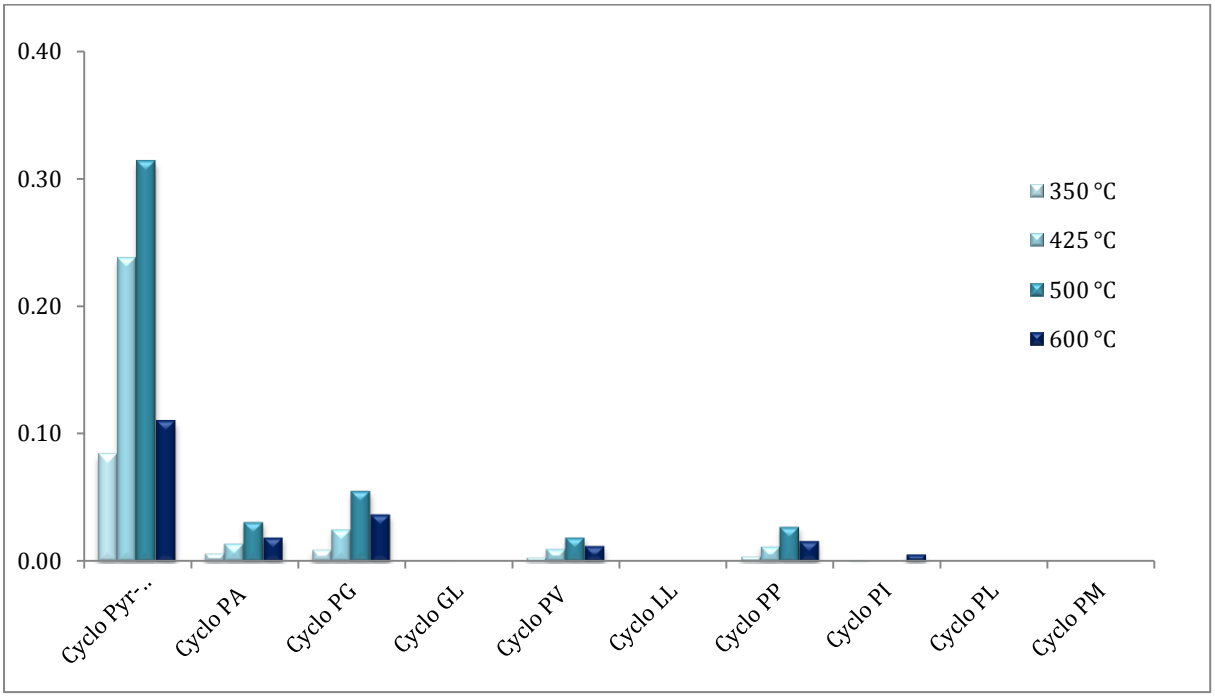

Figure 3.4. DKPs percent mass yields evolved from BSA pyrolysed at different temperatures

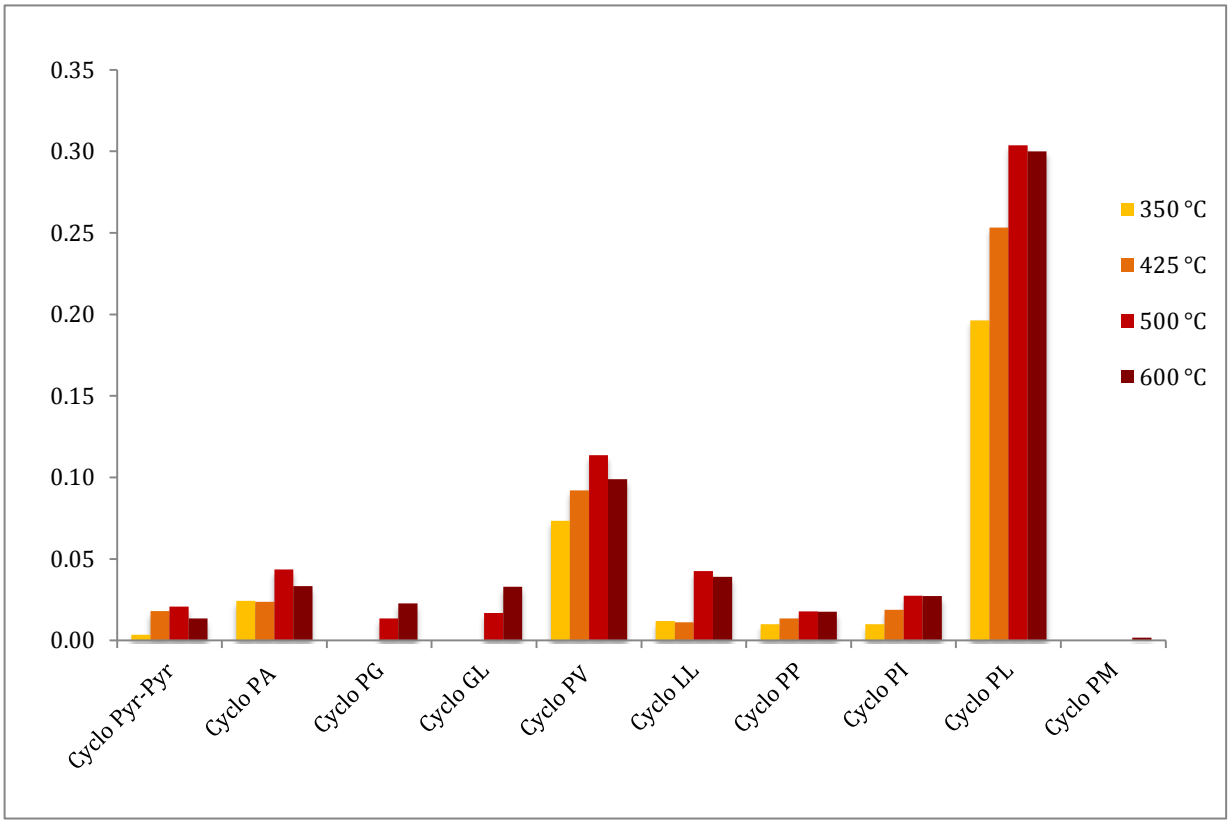

Figure 3.5. Cyclo(Proline-Alanine) percent yields obtained from the corresponding linear dipeptide by pyrolysis at different temperatures.

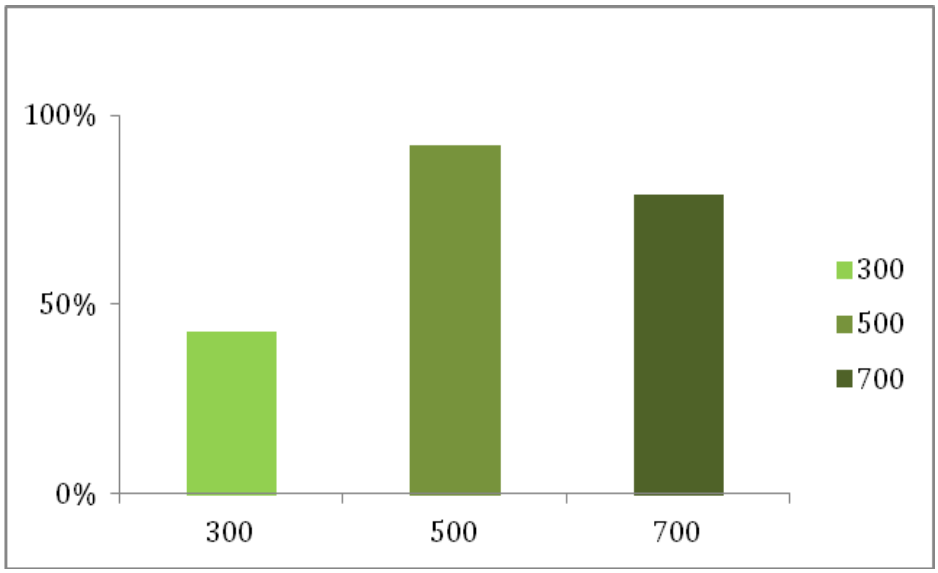

3.7 Final procedure

Off-line Py/GC-MS

Off-line pyrolysis experiments were carried out with a heated platinum filament coil of the pyroprobe model 1000 (CDS Analytical Inc.) utilising the apparatus previously described. About 3-5 mg of samples were pyrolysed at 500 °C (measured temperature) for 100 s at the maximum heating rate (20 °C ms-1) under nitrogen flux (200 mL min-1. All the pyrolyses were performed at the set temperature of 600°C in order to obtain an effective pyrolysis temperature of about 500 °C, a value which allowed to obtain the highest yields of cyclo(Pro-Ala) from the pyrolysis of the corresponding dipeptide and the highest proline containing DKP from pyrolysis of BSA. Pyrolysis products were trapped onto a XAD-2 resin (orbo-43) purchased from Supelco. After pyrolysis, the cartridge was eluted with 5 mL of acetonitrile. The solutions were collected, concentrated under a gentle nitrogen stream and spiked with 0.1 mL of 250 mg L^{-1} of sarcosine anhydride (internal standard) solution in acetonitrile before being analyzed in GC-MS. An aliquot (0.1 mL) was withdrawn from the solution and subjected to the derivatisation procedure for the conversion into the trimethylsilyl (TMS) derivatives, by adding 0.05 mL of 250 mg L^{-1} of 1-oxo-3-benzopiperazine (internal standard for silylation) in acetonitrile and 0.03 mL of N,O-bis-(trimethylsilyl) trifluoroacetamide (BSTFA) plus 1% trimethylchlorosilane (TMCS) and heating at 60 °C for 3 hours in a closed vial. The entire procedure was run in duplicate for each sample.

Off-line GC-MS analysis

Off-line pyrolysates were analyzed in GC-MS with the following temperature programs: from 50 °C to 300 °C (held 5 min) at 5°C min-1 for the underivatized solutions, and from 100°C (held 5 min) to 310°C at 5°C min-1, for the silylated solutions. The injection port was maintained at 260°C. Mass spectra were recorded in the full scan acquisition mode under electron ionisation (70 eV) at 1 scan s^{-1} in the 35–650 m/z range. Relative retention times (RRTs) were calculated with respect to internal standard as RRT = 1–($RT_{standard}$/RT_{DKP}). The RRT values changed within ± 15%.

3.8 Py-GC-MS (on-line)

In the on-line configuration it was not possible to develop an ad hoc silylation procedure since all the attempts of derivatising target analytes (DKPs) and standard cyclodipeptides failed. The pyrolysis apparatus consisted in a CDS 1000 pyroprobe with a platinum filament coil [74], directly connected to the injection port of a Varian 3400 GC coupled to a Saturn II ion trap mass spectrometer by means of a valved interface. Temperatures of split/splitless injector (split mode 1:150) and Py-GC interface were kept at 260°C and 300°C respectively. A Supelco SPB5 capillary column (30 mx0.32 mm I.D., 0.25 um film thickness), with stationary phase poly (5% diphenyl/ 95% dimethyl) siloxane, was used with a temperature programme from 50°C to 300°C (held for 300°C) at 5°C min^{-1} with helium as carrier gas. Mass spectra were recorded at 1 scan sec^{-1} under electron impact at 70 eV, mass range 45 to 300 m/z. In a typical experiment about 0.1 to 0.5 mg of sample were placed in a quartz tube and pyrolysed at 600°C for 20 seconds.

Chapter 4

Pyrolysis of model compounds

4.1. Pyrolysis of proline containing linear peptides

4.1.1 Pro-Glu

The GC-MS of the pyrolysate obtained from the dipeptide Pro-Glu (figure 4.1.1a) was characterized by a single predominant peak corresponding to compound # 41 (table 1). Its mass spectrum, reported in figure 4.1.2, exhibited a base peak at m/z 70 which was associated to the pyrrolidinium ion typical of Pro mass fragmentation. The intense ion at m/z 208 was attributed to the molecular ion consistently with its fragmentation pattern characterised by consecutive losses of three CO neutral molecules forming the ion peaks at m/z 180, 152 and 124. We postulated that the cyclo(Pro-Glu) (molecular mass 226 u) formed upon pyrolysis underwent a dehydration reaction through the attack of the N atom of the piperazine ring to the COOH group of the Glu side chain forming the tricyclic compound # 41 with molecular mass 208 u (figure 4.1.3, route i). This compound is formally a dehydrated cyclo(Pro-Glu). An alternative pathway leading to # 41 involves cyclisation of the Glu side chain of the linear dipeptide with formation of the oxyproline ring followed by cyclisation of the dehydrated dipeptide to give the corresponding DKP (figure 4.1.3, route ii). Reactions involving side chains containing a chemical functionality were often observed in conventional [58, 62] and reactive pyrolysis [81] of amino acids. The cyclisation of Glu side chain is a well known reaction leading to pyroglutamic acid (pyroGlu), while a tricyclic derivative corresponding to cyclo(pyroGlu-pyroGlu) is formed as thermally condensation product of pyroGlu [62]. The attribution of compound # 41 to the proposed structure was confirmed by complementary analytical techniques as described in the following section 4.1.2. Upon silylation, the pyrolysate solution produced a chromatogram still containing compound # 41 (figure 4.1.4a). In addition, the chromatogram was featured by an intense peak at lower retention times (# 72, see table 4.1.2). Its mass spectrum (figure 4.1.5) presented the molecular ion at m/z 280, which is 72 mass units heavier than that of compound # 41, thus corresponding to the addition of a TMS group. Therefore, we postulated that # 72 was the monosilylated derivative of # 41. In the absence of NH groups, the only acid protons capable to be replaced by the TMS group are those in α to the carbonyl group which could be involved in keto-enolic tautomerisation. Hence, the assigned attribution for # 72 was the TMS derivative of the enolic form of # 41 (figure 4.1.5). The mass chromatogram at m/z 370 revealed the presence of a small peak superimposed to that of the cyclo(Pro-pyroGlu). The corresponding mass spectrum reported in figure 4.1.5 was consistent with that of cyclo(Pro-Glu) with a molecular ion at m/z 370, and an ion

peak at m/z 355 (loss of methyl radical). The intense ions at m/z 239 (M+. – CH2COOTMS) and 225 (M+. – CH2 CH2COOTMS) could be assigned to the silylated cyclo(Pro-Ala) and cyclo(Pro-Gly) ions, respectively, which were rather common in the mass spectra of silylated DKPs (figure 4.1.5). However, the given assignment is provisional in the absence of an authentic standard. In fact, an alternative structural attribution would be possible: the linear dipeptide Pro-pyroGlu with the oxoproline ring formed from the condensation of the lateral chain (i.e. the disilylated Pro-pyroglutamic acid). It is worth noting that the structures of the silylated DKPs shown in figure 4.1.5 were depicted in the keto form with the TMS group bound to the N atom, which should be favoured over the O-TMS enolic form [90]. The occurrence of a small peak corresponding to the non-silylated DKP-like internal standard (1-benzyl-3-oxo-piperazine) is indicative to the difficulty in the quantitative trimethylsilylation of the cyclic amide of DKPs. This standard was utilised to check the efficiency of trimethylsilylation.

4.1.2 Identification of the hexahydrodipyrrolo[1,2-a:1',2'-d]pyrazine-3,5,10(10aH)-trione (cyclo(Pro-pyroGlu))

The fact that the pyrolysis of Pro-Glu produced a single predominant compound enabled the application of NMR analysis directly to the dipeptide pyrolysate. The results of extensive NMR experiments confirmed the structure proposed above corresponding to cyclo(Pro-pyroGlu). Figure 4.1.6 shows the preferred conformation useful for the following discussion of NMR data. In addition to the deshielded triplets at 4.55 and 4.21 ppm for the methine protons and the multiplet at 3.58 ppm, characteristic for each Pro DKP, the 1HNMR spectrum showed a triplet at 2.62 ppm attributable to two protons in vicinal position to an additional carbonyl group. Long range 1H /13C correlations allowed the assignment at 165.9 and 165.0 ppm for C-6 and C-12 (see figure 4.1.3 for carbon numbering) respectively, besides a singlet at 172.6 ppm for the third carbonyl group C-2. The relative configuration of the stereogenic centers was drawn from nOe data in the light of molecular mechanics (MM2) minimized conformations. Thus, the cis-relationship between H-5 and H-11 was established from the observation of the nOe enhancements by the relative NMR experiment. However the compound resulted optically inactive, and no cotton effects where observed in its CD spectrum, indicating its racemic nature. A further support for the composition C10H12N2O3 came from ESI-MS analysis. In particular, the spectrum recorded in negative ion mode by direct injection of a water/acetonitrile solution showed the pseudo-molecularion [M-H]- at m/z 207, which gave the ions at m/z 179 by the loss of a CO molecule, and at m/z 163 by elimination of a molecule of cyanic acid HNCO. In addition, the analysis in positive ion mode produced an intense signal at m/z 231, corresponding to [M+Na]+ ion, and minor ions at m/z 209 and 439, attributable respectively to

[M+H]+ and the cluster [2M+Na]+. Tandem fragmentation experiments on the latter ion gave the signal at m/z 231 by loss of a molecule of DKP, whereas the fragmentation of m/z 209 furnished the signal at m/z 181 attributable to [M+H-CO]+ ion. MS3 experiment on the latter ion gave m/z 70, attributable to [C4H8N]+ , typical of a Pro unit.

4.1.3 Pro-Gln

The MS pyrolysate of this dipeptide resulted similar to that obtained from Pro-Glu with a predominant peak due to compound cyclo(Pro-pyroGlu) (# 41, figure 4.1.1b). This is in accordance to the formation mechanism postulated above for Pro-Glu, with the difference that ammonia was eliminated from the Gln lateral chain in place of water from Glu. Smaller peaks due to cyclo(Pro-Ala) isomers (# 7, 8) were detected as minor products probably resulting from the homolytic chain scission of the lateral chain (the same peaks were detected at low levels also in the Pro-Glu pyrolysate). Diastereomeric isomers of DKPs are typically observed due to thermally racemisation of amino acids [59]. The identification of cyclo(Pro-Ala) was confirmed by the GC-MS analysis of the pyrolysate of the Pro-Ala dipeptide (mass spectrum in figure 4.1.2), while its formation from cyclo(Pro-Asp) is supported by the evidence that γ-hydrogen rearrangement reactions (McLafferty-type rearrangement) are typical of thermally treated DKPs [83]. Moreover, chain fragmentation reactions producing cyclic oligopeptides with shorter lateral chains were reported to occur at relatively low temperatures (around 200 °C) [91]. The assignment of cyclo(Pro-Pro) structure to compound # 24 is an indication that intermolecular reactions, such as condensation of amino acids or peptides with formation of new peptide bonds (Pro-Pro in this case), may occur prior to DKP formation. The occurrence of intermolecular condensation reactions of peptides subjected to (sub)pyrolysis has been recently demonstrated by MS studies [72]. In particular, it is known that pyrolysis of Pro produces the corresponding DKPs with high yields [59]. The consecutive elimination of dihydrogen from cyclo(Pro-Pro) might be responsible for the presence of the small peaks attributed to compounds # 17 and # 6. This is in line with the report that DKPs are thermally fragmented to different products associated to the loss of molecular hydrogen [83]. The chromatogram obtained for the silylated pyrolysate (not shown) resulted similar to that obtained from Pro-Glu, showing the peak due cyclo(Pro-pyroGlu) along with the TMS ether of its enolic form (# 41 and # 72, respectively). Therefore, compound # 41 (table 4.1.1) was characteristic from the pyrolysis of both Pro-Glu and Pro-Gln. The occurrence of a small peak exhibiting a mass spectrum with ions at m/z 73, 131, 226, 238, 354, 369 (# 76 in table 4.1.2) might support the formation of the disilylated cyclo(Pro-Gln). However, the intensity of this peak was too low for a reliable mass spectral interpretation.

4.1.4 Pro-Asp

The GC trace of the products evolved from the pyrolysis of Pro-Asp was characterised by rather weak peaks (chromatogram not shown). Among them, two peaks of isomeric cyclo(Pro-Ala)(# 7, 8) derived from the decarboxylation of the lateral chain and compound # 10 with a molecular ion at m/z 166 attributed to its dehydrogenated derivative are in accordance to fragmentation scheme of the cyclo(Pro-Ala) proposed in the literature [83]. Upon silylation, the GC-MS pattern changed significantly (figure 4.1.4b) and a series of peaks with mass spectra in accordance to the silylated cyclo(Pro-Asp) were revealed. The two peaks # 68 and # 69 displayed the same mass spectra (figure 4.1.5) characterised by an intense molecular ion at m/z 356, an ion peak at m/z 341 (loss of methyl radical) and at m/z 239 (loss of COOTMS radical) consistent with the two isomers of the persilylated cyclo(Pro-Asp). The smaller pair of peaks # 73 and # 74 eluting at higher retention times were assigned to the partially silylated derivatives of cyclo(Pro-Asp) according to their mass spectral pattern with ions at m/z 284 (molecular ion), 269 (M+. – CH3), 167(M+. – COOTMS), 73 (TMS+), 70 (pyrrolidinuim ion).Two smaller peaks eluting in the initial part of the DKP elution region (# 57 and # 58) were assigned to the silylated cyclo(Pro-Ala) by comparison with the GC-MS analysis of the silylated pyrolysate of the Pro-Ala dipeptide. The mass spectrum of one of the two isomers is reported in figure 4.1.5.

4.1.5 Pro-Lys

Pyrolysis of this peptide resulted in the formation of ion traces (figure 4.1.1c) characterised by a cluster of peaks displaying intense molecular ions at m/z 206 and 208 as exemplified in figure 4.1.2. The mass spectra of compounds # 26 and 27 exhibited intense ions at m/z 70 and m/z 154 (base peak) supporting the DKP ring from Pro. The molecular weight value of 208 u corresponds to the loss of the amino group from the lateral chain of the cyclo(Pro-Lys), with formation of a 1-butenyl substituent. The pyrolytic loss of the amino group from Lys residue was reported by Hendrickson and Voorhees [85] in the Py-MS of Gly-Lys dipeptide. Thus, the tentative assigned molecular structure was the pyrrolidino[1, 2a]-3,6-piperazinediones with a 4-butenyl lateral chain. The molecular ion fragmented into the m/z 154 ion through a Mc Lafferty rearrangement. These compounds were probably responsible for the presence of peaks # 66 and 67 in the chromatogram of the silylated pyrolysate shown in figure 4.1.4c. However, these DKPs were not observed in the pyrolysate of Lys-Pro-Leu (section 3.2.2). The mass spectra of the second pairs of isomers # 28, 29 with molecular weight 208 u (figure 4.1.2) were characterised by an intense molecular ion resulting not fully in accordance to an alkyl lateral chain that would tend to be eliminated forming an intense m/z 154 ion typical of alkylated pyrrolidino[1, 2a]-3,6-piperazinediones. Thus, a six-membered

cyclic structure was hypothesised according to the mass spectrum characterised by a series of peak ions at m/z 180, 152 and 124 corresponding to the loss of 28 u (CO or CH2CH2) from the molecular ion (figure 4.1.2). The loss of 70 u and 84 u giving the ions at m/z 138 and m/z 124 along with the intense ions at m/z 70 and m/z 80 were attributed to the occurrence of pyrrolidine and piperidine units, respectively. Subsequent dehydrogenation of these compounds should form the DKPs # 30, 31 and 32 with molecular weight 206 u. The position of the double bond in the proposed structure for # 31 is merely illustrative. Although their exact structure remained to be confirmed, these DKPs could be considered specific markers of Pro-Lys sequences since Lys is the only protein amino acid with a C4 lateral chain. The ion chromatogram of the silylated pyrolysate is shown in figure 4.1.4c. The occurrence of the peaks # 28-32 would support the occurrence of the piperidine ring with a tertiary nitrogen atom not amenable to silylation. The pair of peaks # 66/67 with same mass spectrum exhibiting an intense molecular ion at m/z 280 and the typical ions of the silylated DKP at m/z 209 and m/z 225 were assigned to the silylated Pro-based DKPs with a butenyl side chain. The region at high retention times was featured by two doublets of GC peaks, # 80/81 and # 84/85,(figure 4.1.4c) each displaying the same mass spectrum attributed to the persilylated and partially silylated cyclo(Pro-Lys), respectively. The structural attribution was in accordance to the mass fragmentation pattern. The mass spectrum of the persilylated cyclo(Pro-Lys), shown in figure 4.1.5, exhibited the molecular ion at m/z 441 which decomposed to the ions at m/z 426 by loss of methyl radical and m/z 354 by loss of TMS radical. The base peak at m/z 174 was associated to the CH2=N(TMS)2+ fragment which was a distinctive ion of the intact amino group of the DKPs. In fact, the same base peak at m/z 174 was observed in the mass spectra of peaks # 84/85, attributed to the disilylated cyclo(Pro-Lys) according to the occurrence of the ions at m/z 369 (molecular ion), m/z 364 (M+• – CH3) and m/z 269 (M+• – TMS)

4.1.6 Pro-Arg

The untreated pyrolysate of Pro-Arg (figure 4.1.1d) exhibited GC peaks associated to diketodipyrrole (pyrocoll), cyclo(Pro-Ala), dehydrocyclo(Pro-Pro) and cyclo(Pro-Pro). Degradation of the side chain of Arg probably gave rise to the peaks # 16 and # 18 exhibiting mass spectra similar to those of DKPs formed by condensation of Pro with an alkyl amino acid such as Val, Leu and Ile (table 4.1.2) characterised by fragment ions at m/z 70, 125 and 154 (base peak) and barely detectable molecular ions. A similar pair of compounds was reported by Stankiewicz from the pyrolysis of Pro-Arg [88]. The proposed structure was that of the Pro-based DKP with a propyl chain formed from the elimination of the guanidinium group (H2N-(C=NH)-NH2) from Arg. This compound was identified water soluble condensate of cigarette smoke [91].

The occurrence of the cyclo(Pro-Arg) could not be revealed in the silylated form. Nevertheless, the GC trace of the silylated pyrolysate of Pro-Arg exhibited a relatively intense peak at high retention times (# 77) attributed to the silylated DKP with a 4-aminopropyl side chain formally derived from cyclo(Pro-Arg) after elimination of the cyanamide group (H2N-CN) (that is the triTMS derivative of hexahydro-3-propylamino pyrrolidino[1, 2a]-3,6-piperazine-1,4-dione). The attribution was based on the following peak ions: m/z 427 (molecular ion), 412 (M+. – CH3), 354 (M+. – TMS) and 174 (base peak, CH2=N(TMS)2+).

4.1.7. Pro-Glu-Leu

The GC-MS of the resulting pyrolysate is shown in figure 4.1.7. The cyclo(Pro-pyroGlu) # 41 was revealed at high retention times, confirming that the dehydrated cyclo(Pro-Glu) is formed even when Glu is not the terminal amino acid and is joined through a peptide bond to an another amino acid. The corresponding DKP from Leu, i.e. cyclo(Leu-pyroGlu) could not be detected. The two intense peaks # 7 and # 8 were the isomeric cyclo(Pro-Ala) derived from the fragmentation of the side chain. The occurrence of peaks # 23 and # 25 atttributed to isomeric cyclo(Pro-Leu) derived probably from the thermal "scrumbling" of amino acids in the melt and formation of peptides [72]. These DKPs were identified as silylated derivatives after derivatisation of the pyrolysate (see table 4.1.2).

4.1.8. Lys-Pro-Leu

Pyrolysis of this tripeptide produced the deaminated cyclo(Pro-Lys) derivatives # 28, 29 and the dehydrogenated derivatives # 30-32 observed in the pyrolysate of Pro-Lys (ion traces not shown). The cyclo(Pro-Lys) isomeric pairs in the form of tri (# 80/81) and diTMS (#84/85) derivatives were identified in the pyrolysates after treatment with BSTFA (figure 4.1.8). These experiments confirmed the formation of cyclo(Pro-Lys) when Pro is not the terminal amino acid. The intense peaks # 62/63 corresponded to the silylated cyclo(Pro-Leu) isomers.

Table 4.1.1 GC-MS characteristics of DKPs evolved from the pyrolysis of peptide containing proline and protein samples (BSA: bovine serum albumin; COLL: collagen). RRT: retention time relative to sarcosine anhydride. Notes: identification by comparison with pure compound (1) and published mass spectra (2), [84]; (3), [94]; (4), [76]; (5), [97]; (6), [88]; (7), [89]; (8), [75]. Fabbri et al. (2012) [182].

#	RRT	*m/z*	DKP	Sample
1	-0.17	30, 71, 86,***114***	Gly-Gly[2]	COLL
i.s.	0.00	42, 57, 113, **142**	Sarcosine an.de[1]	Standard
2	0.053	**44**, 99, *142*	Ala-Ala[1]	Standard
3	0.137	57, 70, 85, **114** *(156)*	Gly-Val[1]	Standard
4	0.174	72, 113, 127, **156** *(198)*	Val-Val[2]	BSA
5	0.178	72, 113, 127, **156** *(198)*	Val-Val[2]	BSA
6	0.222	65, 93, 130, ***186***	Pyrocoll[3]	COLL
7	0.228	**70**, 97, 125, *168*	Pro-Ala[4]	ProAla
8	0.245	**70**, 97, 125, *168*	Pro-Ala[4]	ProAla
9	0.259	83, 98, **111**, *154*	Pro-Gly[4]	COLL
10	0.269	69, 70, **123**, *166*	Pro-Ala-H_2	ProAsp
11	0.276	56, 85, 99, **114**, 127,*(170)*	Gly-Leu[4]	BSA
12	0.297	**70**, 72, 125, **154**, *(196)*	Pro-Val[4, 5]	BSA
13	0.302	113, **156**, 170, *(212)*	Val-Leu	BSA
14	0.308	**70**, 72, 125, **154**, *(196)*	Pro-Val[4,5]	BSA
15	0.309	113, **156**, 170, *(212)*	Val-Leu	BSA
16	0.324	**70**, 125, **154**	Pro-Arg-(CN_3H_4)[6]	ProArg
17	0.333	70, 94, **191**, 192	Pro-Pro-H_2	ProArg
18	0.335	**70**, 125, **154**	Pro-Arg-(CN_3H_4)[6]	ProArg
19	0.338	70, 86, 125,**154,** (*210*)	Pro-Ile	BSA
20	0.341	70, 86, 125, **154,** (*210*)	Pro-Ile	BSA
21	0.343	86, 98, 113, **170**, *226*	Leu-Leu	BSA
22	0.345	86, 98, 113, **170**, *226*	Leu-Leu	BSA
23	0.345	**70**, 86, 125, 154(*210*)	Pro-Leu[4,5]	ProGluLeu
24	0.349	**70**, 96, 138, 166, ***194***	Pro-Pro[4]	COLL
25	0.350	**70**, 86, 125, 154,(*210*)	Pro-Leu[4,5]	ProGluLeu
26	0.350	70, 125, **154**, 166, *208*	Pro-Lys-NH_3	ProLys
27	0.353	70, 125, **154**, 166, *208*	Pro-Lys-NH_3	ProLys
28	0.363	70, 84, 152, 180, ***208***	Pro-Lys-NH_3	ProLys
29	0.366	70, 84, 152, 180, ***208***	Pro-Lys-NH_3	ProLys
30	0.367	70, 122, 150, 178, ***206***	Pro-Lys-NH_3/ H_2	ProLys
31	0.371	70, 122, 150, 178, ***206***	Pro-Lys-NH_3/ H_2	ProLys
32	0.401	70, **150**, 177, 178, *206*	Pro-Lys-NH_3/ H_2	ProLys
33	0.416	44, **91,** 127,*218*	Phe-Ala[7]	BSA
34	0.425	44, **91,** 127,*218*	Phe-Ala[7]	BSA
35	0.427	**70**, 86, 124, *210*	Pro-Hyp[3]	COLL
36	0.440	**70**, 86, 124, *210*	Pro-Hyp[3]	COLL
37	0.440	**91,** 113, 127, 155, *246*	Phe-Val[8]	BSA
38	0.441	70, 139, **154**, 167, *228*	Pro-Met[4]	BSA
39	0.445	70, 139, **154**, 167, *228*	Pro-Met[4]	BSA
40	0.448	**91,** 113, 127, 155, *246*	Phe-Val[8]	BSA
41	0.449	70, 96, 124, 152, 180, ***208***	Pro-pyroGlu	ProGlx
42	0.463	**91,** 113, 141, 204, *260*	Phe-Leu[8]	BSA

43	0.465	70, 91, **125**, 153, *244*	Pro-Phe[4,5]	BSA
44	0.468	**91,** 113, 141, 204, *260*	Phe-Leu[8]	BSA
45	0.475	70, 91, **125**, 153, *244*	Pro-Phe[4,5]	BSA
46	0.556	70, 107, **154**, *260*	Pro-Tyr[5]	ProTyr

Tabel 4.1.2 GC-MS characteristics of trimethylsilyl (TMS) derivatives of DKPs. RRT: retention time relative to the silylated 1-benzyl-3-oxo-piperazine (internal standard). Fabbri et al. (2012) [182].

#	RRT	IONS	DKP	TMS
47	-1.05	156, 171, 255, **271**, *286*	Ala-Ala	Di
48	-0.994	156, 171, 255, **271**, *286*	Ala-Ala	Di
49	-0.882	129, 142, 241, **257**, *272*	Gly-Ala	Di
50	-0.781	73, 100, 147, **243**, *258*	Gly-Gly	Di
51	-0.511	142, 170, 257, **285**, *300*	Gly-Val	Di
52	-0.384	156, **257**, 271, 299, *314*	Gly-Leu	Di
53	-0.295	73, 299, 313, **341**, *356*	Val-Leu	Di
54	-0.284	73, 299, 313, **341**, *356*	Val-Leu	Di
55	-0.233	212, **314**, 327, 355, *370*	Leu-Leu	Di
56	-0.214	212, **314**, 327, 355, *370*	Leu-Leu	Di
57	-0.217	70, 97, 170, 225,***240***	Pro-Ala	Mono
58	-0.139	70, 97, 170, 225,***240***	Pro-Ala	Mono
59	-0.114	70, 83, 183, 211, ***226***	Pro-Gly	Mono
60	-0.059	**73**, 197, 225, 253, 268	Pro-Val	Mono
61	-0.048	**73**, 197, 225, 253, 268	Pro-Val	Mono
i.s.	0.000	73, 91, **171**, 247, *262*	-	Mono
62	0.018	73, **226**, 239, 267, *282*	Pro-Leu	Mono
63	0.028	73, **226**, 239, 267, *282*	Pro-Leu	Mono
64	0.017	**73**, 243, 271, 347, *362*	Phe-Ala	Di
65	0.033	**73**, 243, 271, 347, *362*	Phe-Ala	Mono
66	0.056	70, 124, 226, 265, ***280***	Pro-Lys-NH_3	Mono
67	0.077	70, 124, 226, 265, ***280***	Pro-Lys-NH_3	Mono
i.s.	0.071	42, **91**, 99, 161, *190*	-	Non
68	0.201	73, 225, 239,341, ***356***	Pro-Asp	Di
69	0.203	73, 225, 239,341, ***356***	Pro-Asp	Di
70	0.196	70, 124, 156, **267**, *282*	Pro-Hyp	Mono
71	0.215	70, 124, 156, **267**, *282*	Pro-Hyp	Mono
72	0.223	73, 209, 225, **265**, *280*	Pro-Glu-H_2O	Mono
73	0.243	70, 73, 167, 269, ***284***	Pro-Asp	Mono

74	0.247	70, 73, 167, 269, ***284***	Pro-Asp	Mono
75	0.277	**73**, 225, 239, 355, *370*	Pro-Glu	Di
76	0.337	**73**, 131, 226, 238, 354, *369*	Pro-Gln	Di
77	0.357	311, 354, **174**, 412, *427*	ProArg-$C_2H_2N_2$	Tri
78	0.377	73, **179**, 225, 389, *404*	Pro-Tyr	Di
79	0.392	73, **179**, 225, 389, *404*	Pro-Tyr	Di
80	0.397	**174**, 297, 368, 426, *441*	Pro-Lys	Tri
81	0.400	**174**, 297, 368, 426, *441*	Pro-Lys	Tri
82	0.416	180, **179**, 226, 317, *332*	Pro-Tyr	Mono
83	0.432	180, **179**, 226, 317, *332*	Pro-Tyr	Mono
84	0.430	73, **174**, 296, 354, *369*	Pro-Lys	Di
85	0.431	73, **174**, 296, 354, *369*	Pro-Lys	Di

Figure 4.1.1 GC-MS traces (total ion) of the solutions obtained after off-line pyrolysis at 500 °C of linear dipeptides a: Pro-Glu; b: Pro-Gln; c: Pro-Lys; d: Pro-Arg. Peak numbers corresponds to compounds listed in table 4.1.1. Fabbri et al. (2012) [182].

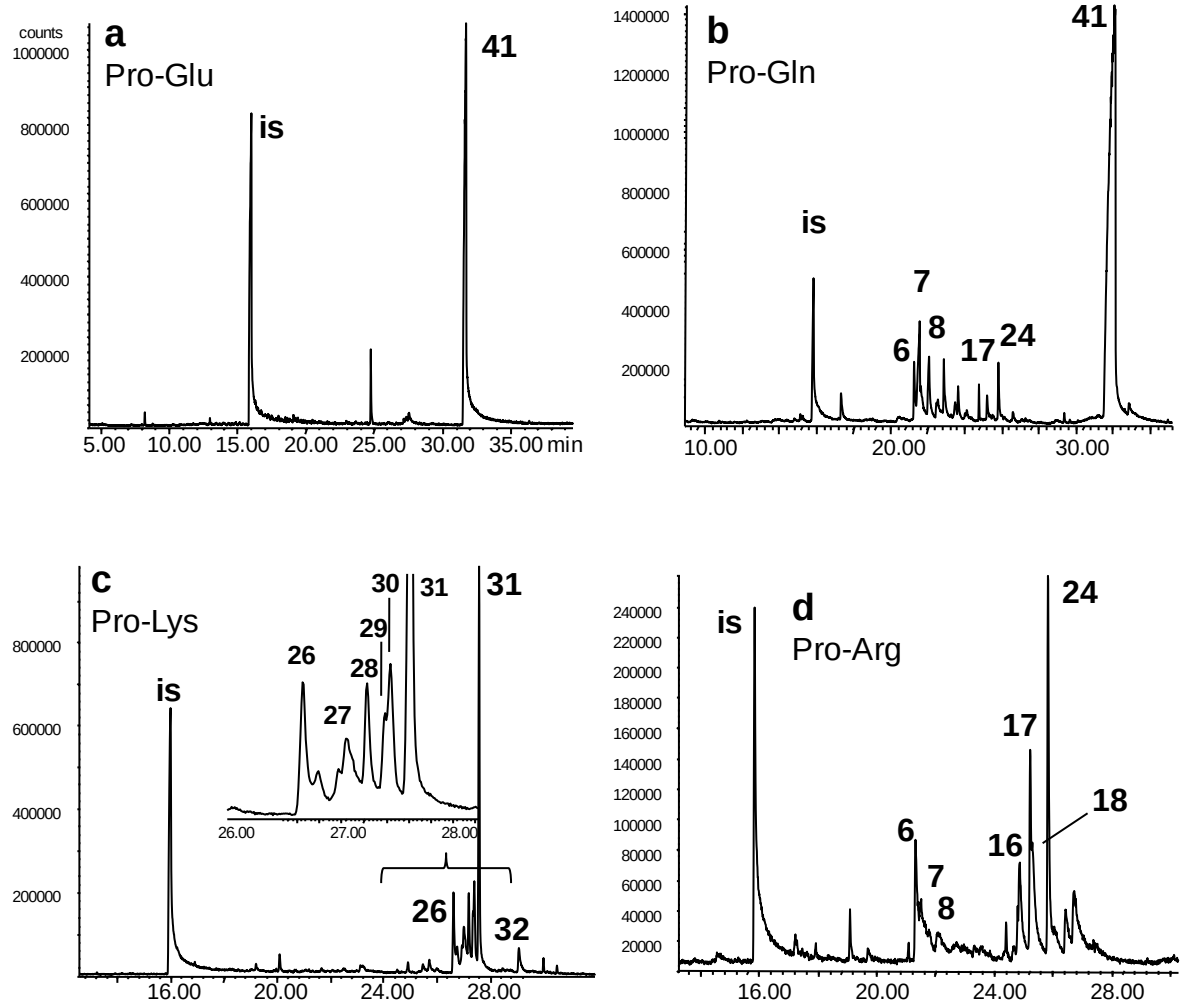

Figure 4.1.2 Mass spectra of selected 2,5-diketopiperazines (DKPs) with the assigned molecular structure. Numbers # correspond to compound numbering in table 4.1.1. Fabbri et al. (2012) [182].

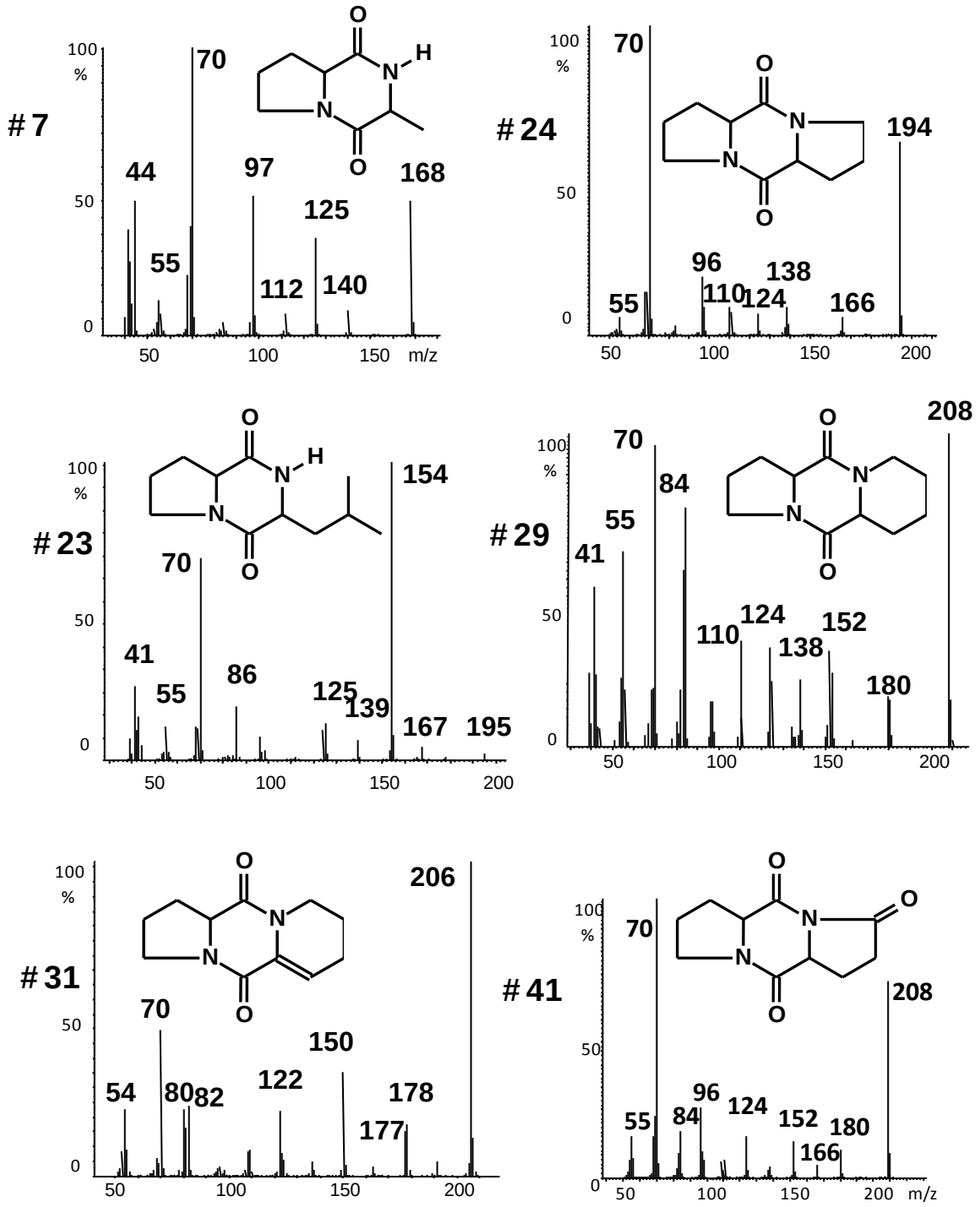

Figure 4.1.3 Proposed mechanism pathways (i) and (ii) leading to the dehydrated cyclo(Pro-Glu) (DKP # 41). Arbitrary atom numbering is for convenience. Fabbri et al. (2012) [182].

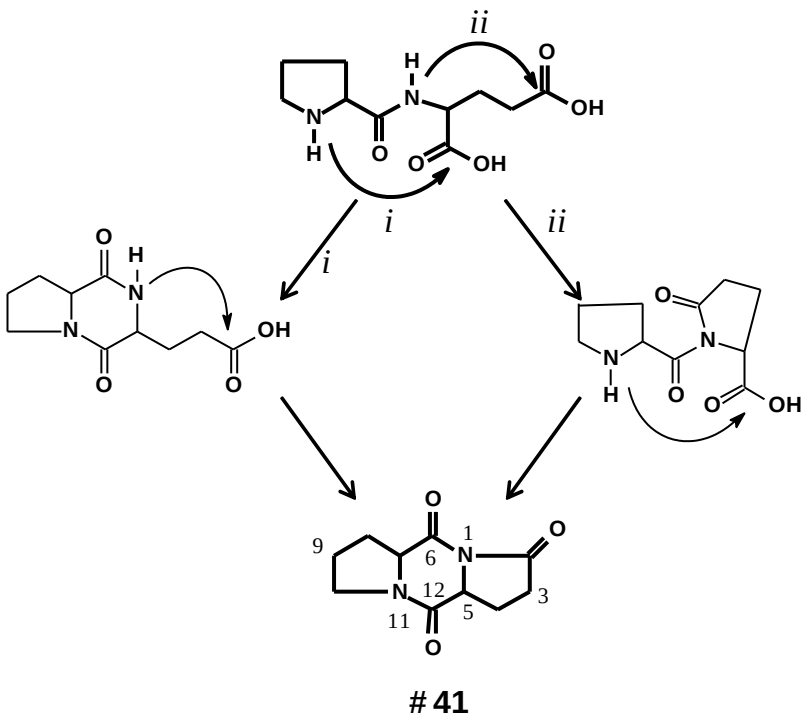

Figure 4.1.4 GC-MS traces (total ion) of the trimethylsilylated solutions obtained after off-line pyrolysis at 500 °C of linear dipeptides a: Pro-Glu; b: Pro-Asp; c: Pro-Lys; d: Pro-Arg. Peak numbers correspond to compounds listed in tables 4.1.1 and 4.1.2. Pyroglutamic acid diTMS (RRT - 0.425); *m/z* 73, **156**, 230, 258, (*273*). Fabbri et al. (2012) [182].

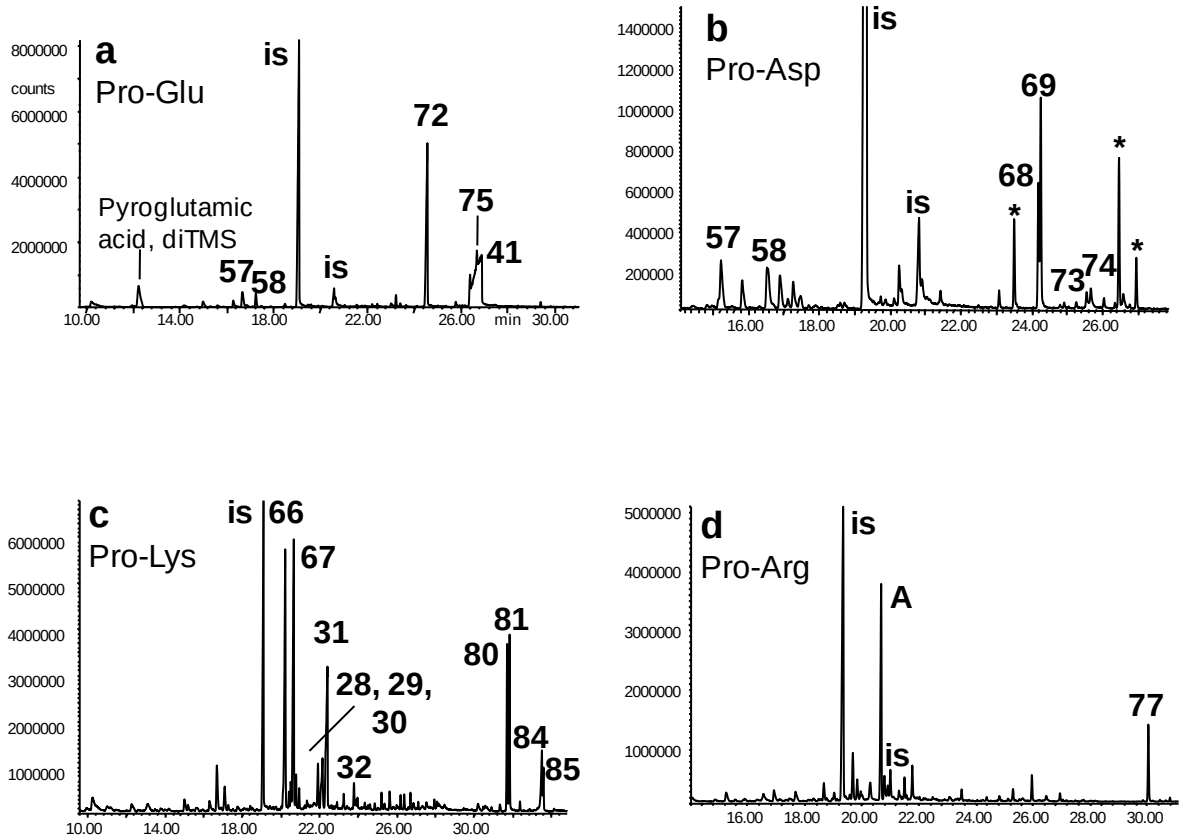

Figure 4.1.5 Mass spectra of selected TMS derivatives of 2,5-diketopiperazines (DKPs) with the tentative assigned molecular structure. Numbers # correspond to compound numbering in table 4.1.2. Fabbri et al. (2012) [182].

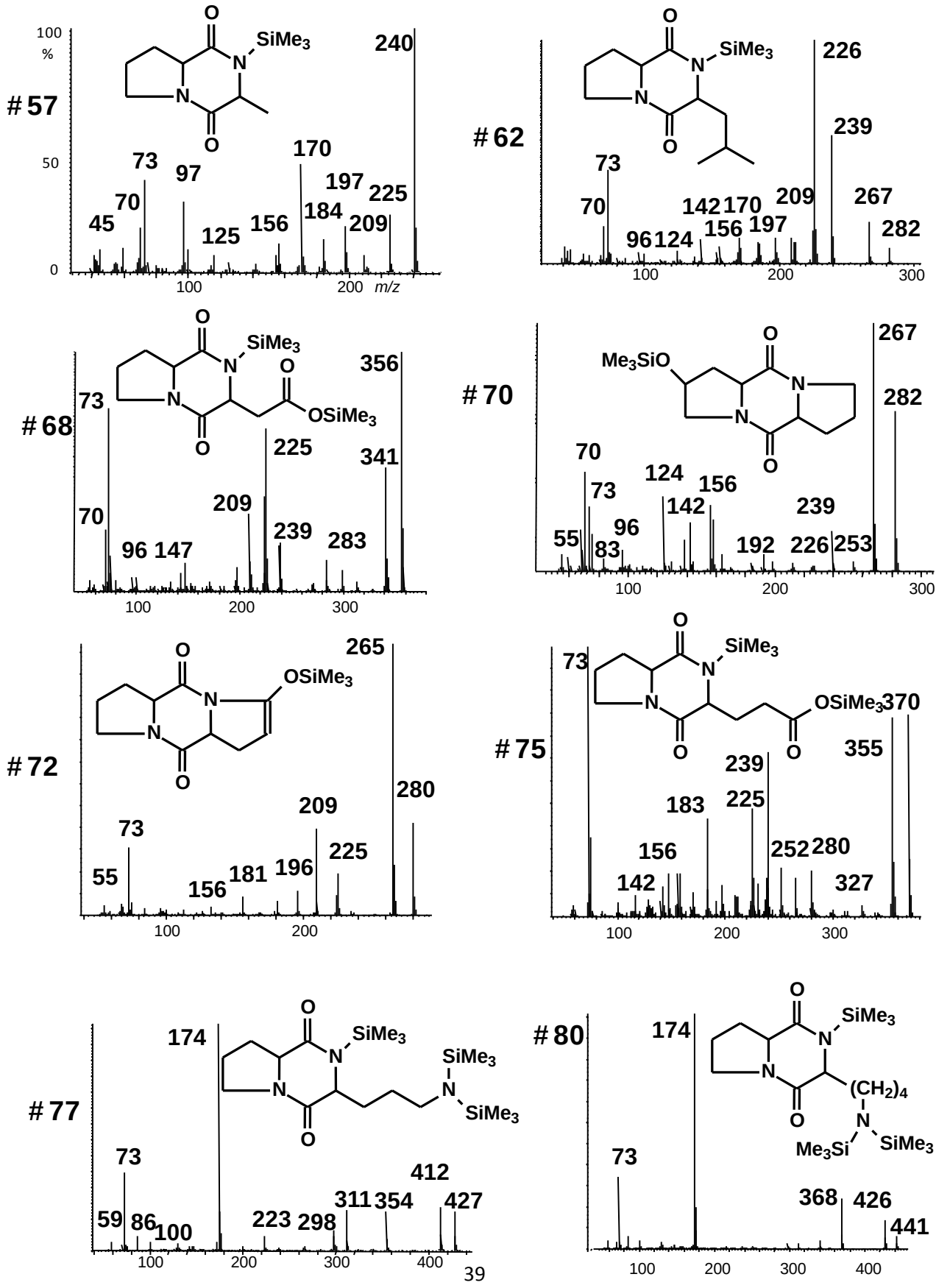

Figure 4.1.6 Minimized conformation by MM calculations of DKP # 41. The distance H-5/H-11 is 2.8 Å,in line with the observation of NOE effect between the two protons.

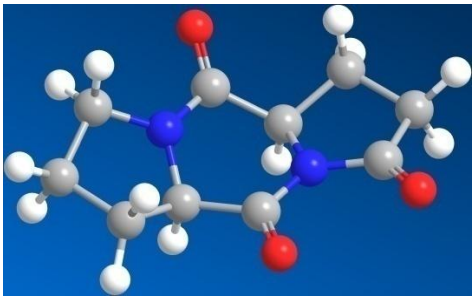

Figure 4.1.7 GC-MS trace (total ion) of the solutions obtained after off-line pyrolysis at 500 °C of the linear tripeptide Pro-Glu-Leu. Peak numbers correspond to compounds listed in table 4.1.1. Fabbri et al. (2012) [182]

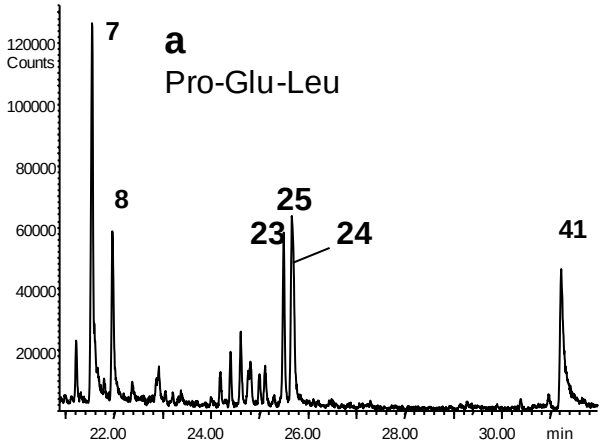

Figure 4.1.8 GC-MS trace (total ion) of the trimethylsilylated solution obtained after off-line pyrolysis at 500 °C of the linear tripeptide Lys-Pro-Leu. Peak numbers correspond to compounds listed in tables 4.1.1 and 4.1.2. Fabbri et al. (2012) [182].

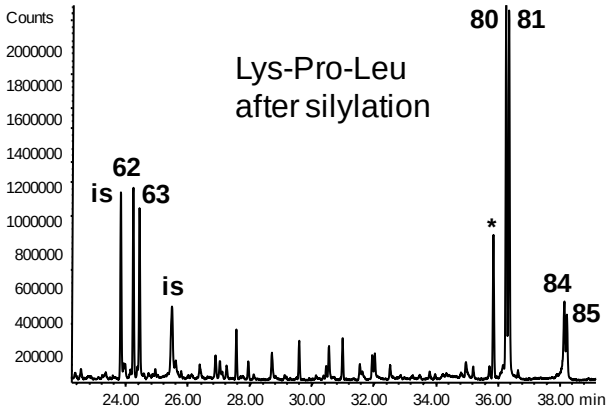

4.2 Pyrolysis of dipeptides containing polar amino acids

4.2.1 *Asp-Asp*

The GC trace of the products evolved from the pyrolysis of Asp-Asp was characterised by three main peaks (chromatogram not shown), whose molecular attribution and mass spectra were reported in table 4.2.1, corresponding to maleimide (compound #5), succinimide (#7) and a compound (#28) identified as maleimide dimer. The latter compound was reported to be formed upon asparagines pyrolysis by Sharma et al. [62]. Other less abundant peaks were attributed to alkyl derivatives of maleimide (#3) and succinimide (#10). The two compounds were previously reported to be formed during aspartic acid pyrolysis [57]. The mass spectrum of the isomeric form of maleimide, reported in figure 4.2.1, exhibited a base peak at *m/z* 125. The molecular ion of this compound was attributed to the peak at m/z 196. Upon silylation, the GC-MS pattern of the pyrolysate changed significantly. Relative retention times and mass spectra of the silylated derivatives of the products formed during polar dipeptides pyrolysis, are listed in table 4.2.2. A series of peaks with mass spectra in accordance to the silylated maleimide dimer (compounds # 52 and 53) and cyclo(Asp-Ala) (compound # 61) were revealed.

4.2.2 *Asp-Glu*

Pyrolysis of this peptide resulted in the formation of ion traces characterized by a cluster of peaks including 2,5-furandione (compound #2 in table 4.2.1), which is the main peak of the underivatized GC-MS trace and was reported to be formed from the pyrolysis of protein inside humic matter in soil [93]. Another abundant peak was attributed to maleimide (# 5), which is a typical pyrolysis products of aspartic acid. The region at high retention times was featured by high peaks (compounds # 29 and 30) which gave a mass spectra with an intense signal at m/z 210. Other minor peaks were attributed to hydroxyproline derivatives (compounds #12, #14 and 16) and pyrimidine carboxylic acid (# 11), reported to be formed during the pyrolysis of polar amino acids [145]. The chromatogram obtained for the silylated pyrolysate (not shown) is dominated by the presence of pyroglutamic acid, not reported in table 4.2.2. Other peaks were attributed to several amino-carboxylic acids, such as pyrimidine-dicarboxylic acid and quinolic acid.

4.2.3 *Gly-Asp*

The GC-MS of the pyrolysate obtained from the dipeptide *Gly-Asp* was characterized by three main peaks corresponding, from the most to the less abundant, to an alkyl pyrrolidine (# 13), maleimide (# 5) and to a peak that was not identified. The silylated GC-MS trace is featured by several peaks,

including a cyclic dipeptide, cyclo(Gly-Asp) (#45), deriving from the direct cyclisation of the two amino acids, and the TMS derivatives of cyclo(Gly-Gly) (# 41) formed from the decarboxylization of the aspartic moiety. The parabanic acid TMS derivative (#42) was also identified in Asp-Gly pyrolysate; similar compounds were reported in the literature to be formed during poly-glycine and poly-alanine pyrolysis [205]. The molecular structure and the mass spectra of this compound were reported in figure 4.2.1.

4.2.4 *Glu-Asp*

The GC-MS of the pyrolysate obtained from the dipeptide Glu-Asp was characterized by three predominant peaks attributed to maleic anhydride (#1), maleimide (#5), and a peak whose attribution was uncertain (intense signal at m/z 146, compound not reported). This product was not detected neither in Asp-Asp or Asp-Glu pyrolysate, even if typical products evolved from this peptides were also detected (e.g. maleimide). The pyrolysate of Glu-Asp resulted to be the most complex among all the tested peptides, being featured by plenty of peaks with high signals. A doublet of peaks eluting at high retention times showed a mass spectra with an intense ion at m/z 210. The compounds (#29 and 30), which were also detected in Asp-Glu pyrolysate, were not identified; although the presence of two peaks eluting at similar retention times and exhibiting the same mass spectra suggests that they could be DKPs. The silylated pyrolysate was dominated in the first elution region by the presence of pyroglutamic acid, which was already detected in Asp-Glu pyrolysis and it is known to be formed upon glutamic acid pyrolysis. At higher times four peaks with an intense ion at m/z 476 were detected (compound from # 56 to # 59) . The molecular attribution of these peaks was uncertain; however, the presence of peak doublets suggested that these could be associated to tri-TMS derivative of Glu-Asp DKP.

4.2.5 *Glu-Glu*

The GC-MS trace of this peptide is featured by rather small peaks and few products. The principal compounds detected in the pyrolysate are reported in table 4.2.1, and are maleimide (# 5) , succinimide (# 7) and pyroglutamic acid (# 24) which is the most abundant product . At higher retention times a peak giving a mass spectra with a principal ion at m/z 84 was tentatively identified as the methyl ester of Pyrrolizin-1,7-dione-6-carboxylic acid (# 31). No DKPs were identified in the underivatized pyrolysate. On the other end, a pair of peaks in the silylated GC-MS trace were attributed to tri TMS-derivative of cyclo(PyroGlu-Gly) (compound # 51 and 55, in table 4.2.2), whose formation was supposed to involve the direct cleavage of a glutamic acid lateral chain after cyclisation. Pyroglutamic acid was found to be again the most abundant product, as for all the dipeptide containing glutamic acid.

4.2.6 *Gly-Glu*

The underivatized GC-MS trace of this peptide was characterized by two main peaks identified from the corresponding mass spectra as succinimide and alkyl-pyrrolidin-2-one (compound # 7 and 26 in table 4.2.2), being previously reported from the hydrothermal liquefaction of swine manure [94]. Only cyclo(Pyro-Glu-Gly) (# 35) was identified, with a corresponding mass spectra identical to that found in the pyrolysate of the dipeptide Glu-Glu. The principal peak in the silylated pyrolysate was found again to be the TMS derivatives of pyroglutamic acid (mono and di-TMS). Several peaks were tentatively identified as TMS-derivatives of cyclic dipeptides; more in detail they were tri-TMS derivative of cyclo(PyroGlu-Gly) (# 55 in table 4.2.2), already detected in Glu-Glu pyrolysate, and the di-TMS derivative of cyclo(Glu-Gly) (#50) , whose structure and mass spectra are reported in figure 4.2.2. The chromatogram was featured in addition by several peaks whose mass spectra were not identified.

4.2.7 *Gly-Ser*

The GC-MS trace is featured mainly by three DKP tentatively identified as cyclo(Gly-Ser), cyclo(Gly-Ala) and dehydrated cyclo(Gly-Ser) (compounds # 19, 23 and 25) whose formation involves the elimination of the hydroxyl group of serine. The proposed structure and the mass spectra of the latter DKP are reported in figure 4.2.1. The most abundant product in the silylated GC-MS trace was identified as imidazolidin-2,4-dione TMS derivative (not shown), whose formation in pyrolysis was previously reported in a study on pyrolysis of several dipeptide containing glycine [83]. Another abundant peak was identified as cyclo(Gly-Gly) (compound #41), formed by cyclisation of serine and glycine followed by direct cleavage of serine lateral chain. Cyclo(Gly-Ala) (# 40) TMS derivative was also detected, together with the per-silylated TMS derivative of cyclo(Gly-Ser) (# 43).

4.2.8 *Tyr-Tyr*

The underivatized GC trace of the products evolved from the pyrolysis of Tyr-Tyr was characterized by three sharp peaks in the first elution region (chromatogram not shown), corresponding to methyl-phenol (compound # 6) - the main peak – ethyl-phenol (# 9), and benzene acetonitrile 4-hydroxy (# 22). The products were previously reported as being formed during the pyrolysis of tyrosine [57]. At higher times the chromatogram was occupied by a broad peak which was identified as a phenol derivative, with an intense ion at m/z 214 (# 36). The silylated GC traces showed on the contrary numerous peaks which are not reported in the literature regarding tyrosine pyrolysis. In the first elution region the chromatogram is mainly featured by the elution of indole TMS-derivatives, and

hydrocinnamic acid TMS-esters (compounds not reported in tables). At higher retention times several peaks were attributed to Tyrosine-Tyrosine DKPs mono and disilylated (compound # 62, 63 and 64 in table 4.2.2) and to cyclo(Gly-Tyr) (#60) formed by cyclisation of the dipeptide followed by the direct cleavage of one lateral chain of the two tyrosine moieties. Proposed structures of this molecules are reported in figure 4.2.2 together with their mass spectra. Despite the presence of other peaks, the most interesting pattern was shown from the ion trace reported in figure 4.2.3 characterised by a cluster of peaks displaying intense signals at m/z 179 and associated to TMS derivative of phenol compounds. This pattern was nor reported in the literature for other peptides containing Tyrosine, neither for the single amino acid.

Table 4.2.1 GC-MS characteristics of principal pyrolysis products evolved from the pyrolysis of polar amino acid containing dipeptides. RRT: retention time relative to sarcosine anhydride. Fabbri et al. (2012) [182].

#	Molecular attribution	RRT	Mass spectra	Sample
1	maleic anhydride	-3.39	**54**, 98	Glu-Asp
2	2,5-furandione	-3.36	54, ***98***	Asp-Glu
3	maleimide, N-ethyl	-2.27	**69**, 82, 97, 110, *125*	Asp-Asp
4	oxazole, 2-phenyl	-2.22	51, 90, 117, ***145***	Gly-Glu, Glu-Glu
5	maleimide	-1.93	54, 69, ***97***	Gly-Asp, Glu-Glu, Asp-Asp, Glu-Asp, Asp-Glu
6	methyl-phenol	-1.41	51, 77, **107**, *108*	Tyr-Tyr
7	succinimide	-0.87	56, 69, ***99***	Asp-Asp, Gly-Glu, Glu-Glu
8	pyrimidine, 2,4,5-triamino-	-0.67	56, 69, 98, ***125***	Glu-Asp
9	ethyl-phenol	-0.74	51, 69, **107**, *122*	Tyr-Tyr
10	methyl-succinimide	-0.61	56, 70, **99**, *114*	Asp-Asp
11	1.2,6,dioxohexahydropyrimidine carboxylic acid	-0.59	70, 95, ***113***	Asp-Glu
12	hydroxyproline derivative 1	-0.5	58, 69, **86**, 113	Asp-Glu, Glu-Asp
13	alkyl pyrrolidine	-0.46	51, 69, 110	Gly-Asp
14	hydroxyproline derivative 2	-0.42	58, 69, **86**, 113, 139	Asp-Glu, Glu-Asp
15	unknown (2)	-0.27	69, 146, 73, 57	Glu-Asp
16	hydroxyproline deriv 3	-0.26	58, 69, **86**, 113, 139	Asp-Glu, Glu-Asp
17	2-pyrrolidinecarbonitrile	-0.14	56, 67, ***110***	Glu-Glu
18	pyrrolidine-1-acetonitrile	-0.06	**54**, 69, *138*	Gly-Asp
19	cyclo(Gly-Ser)	0.01	57, 85, 113, ***144***	Gly-Ser
20	succinimide, N-alkyl	0.05	69, ***139***, 167	Asp-Asp
21	unknown (3)	0.14	149, **177**	Glu-Glu
22	benzeneacetonitrile, 4-hydroxy	0.16	51, 78, 106, ***133***	Tyr-Tyr
23	cyclo(Gly-Ala)	0.2	57, **85**, 114, *127*	Gly-Ser
24	pyroglutamic acid	0.28	28, 41, 56, **84**, *129*	Glu-Glu
25	de-hydrated cyclo(Gly-Asp)	0.28	55, 84, **113** ***(154)***	Gly-Asp
26	alkyl,pyrrolidin-2-one	0.35	56, 69, 77, **84**	Gly-Glu
27	dehydrated cyclo(Gly-Ser)	0.37	55, 69, 83, 111, ***126***	Gly-Ser
28	maleimide dimer 1	0.39	55, 97, **125**, 153, *196*	Asp-Asp
29	unknown (4)	0.4	55, 84, 125, **210**	Asp-Glu, Glu-Asp
30	unknown (5)	0.41	55, 84, 125, **210**	Asp-Glu, Glu-Asp
31	pyrrolizin-1,7-dione-6-carboxylic acid methyl ester	0.44	55, 69, **84,** 156, (*197*)	Glu-Glu
32	pyroglutamic derivative 2	0.46	55, 69, **84**	Glu-Glu
33	de-hydrogenated cyclo(Glu-Asp)1	0.47	56, 69, **84**, 130	Glu-Asp
34	de-hydrogenated cyclo(Glu-Asp) 2	0.47	56, 69, **84**, 130	Glu-Asp
35	cyclo(PyroGlu-Gly)	0.47	56, **84**, 97, 126, *168*	Gly-Glu
36	unknown	0.495	51, 91, 107, **121**, 214	Tyr-Tyr

Table 4.2.2 GC-MS characteristics of trimethylsilyl (TMS) derivatives of compounds detected in polar amino acids containing dipeptides pyrolysates. RRT: retention time relative to the silylated 1-benzyl-3-oxo-piperazine (internal standard). The compounds marked by an asterisk (*) have an uncertain attribution.

#	Molecular attribution	RRT	Mass spectra	Sample
40	cyclo(Gly-Ala) di-TMS	-0.98	73, 129, 142, **257**, *272*	Gly-Ser
41	cyclo(Gly-Gly) di-TMS	-0.91	73, 114, 243, **258**	Gly-Asp, Gly-Ser
42	parabanic acid di-TMS	-0.87	73, **100**, 243, *258*	Gly-Asp
43	cyclo(Gly-Ser) di-TMS	-0.24	73, 147, **257**, 345, *360*	Gly-Ser
44	cyclo(Pro-Gly) mono-TMS	-0.14	**83**, 111, 211, *226*	Glu-Glu
45	cyclo(Gly-Asp) tri-TMS	-0.02	73, 156, **271**, 373, *388*	Gly-Asp
46	cyclo(PyroGlu Gly) di-TMS	0.03	73, 168, 241, 297, ***312***	Gly-Glu
47	cyclo(PyroGlu Gly) mono-TMS	0.07	73, 157, 168, **240**	Gly-Glu
48	unknown 6	0.13	73, **156**, *386*	Asp-Glu, Glu-Asp
49	unknown 7	0.14	73, **156**, *386*	Asp-Glu, Glu-Asp
50	cyclo(Gly-Glu) di-TMS	0.16	73, **156**, 171, 315, *330*	Gly-Glu
51	cyclo(Pyro Glu –Gly) tri-TMS 1	0.19	73, 127, **156**, 369, *384*	Gly-Glu, Glu-Glu
52	maleimide dimer di-TMS 1	0.21	73, 100, 155, **325**, *340*	Asp-Asp
53	maleimide dimer di-TMS 2	0.22	73, 100, 155, **325**, *340*	Asp-Asp
54	cyclo(Gly-Tyr) TMS	0.27	73, **179**, 296, 421, *436*	Tyr-Tyr
55	cyclo(PyroGlu –Gly) tri-TMS 2	0.29	73, 127, **156**, 369, *384*	Gly-Glu, Glu-Glu
56	cyclo(Glu-Asp) 1 TMS *	0.36	73, 129, 169, *217*, **476**	Glu-Asp
57	cyclo(Glu-Asp) 2 TMS *	0.36	73, 129, 169, *217*, **476**	Glu-Asp
58	cyclo(Glu-Asp) 3 TMS *	0.37	73, 129, 169, *217*, **476**	Glu-Asp
59	cyclo(Glu-Asp) 4 TMS *	0.37	73, 129, 169, *217*, **476**	Glu-Asp
60	cyclo(Tyr-Tyr) mono TMS 1	0.40	73, 173 341, **356,** *372*	Tyr-Tyr
61	cyclo(Asp-Ala) diTMS	0.41	73, 103, 147, ***371****(M-H)*	Asp-Asp
62	cyclo(Tyr-Tyr) mono TMS	0.52	73, 173 341, **356,** *372*	Tyr-Tyr
63	cyclo(Tyr-Tyr) di-TMS 1	0.55	73, **179**, 364, 455, *470*	Tyr-Tyr
64	cyclo Tyr-Tyr) di-TMS 2	0.56	73, **179**, 364, 455, *470*	Tyr-Tyr

Figure 4.2.1 Mass spectra of selected compounds with the tentative assigned molecular structure. Numbers # correspond to compound numbering in tables 4.2.1 and 4.2.2.

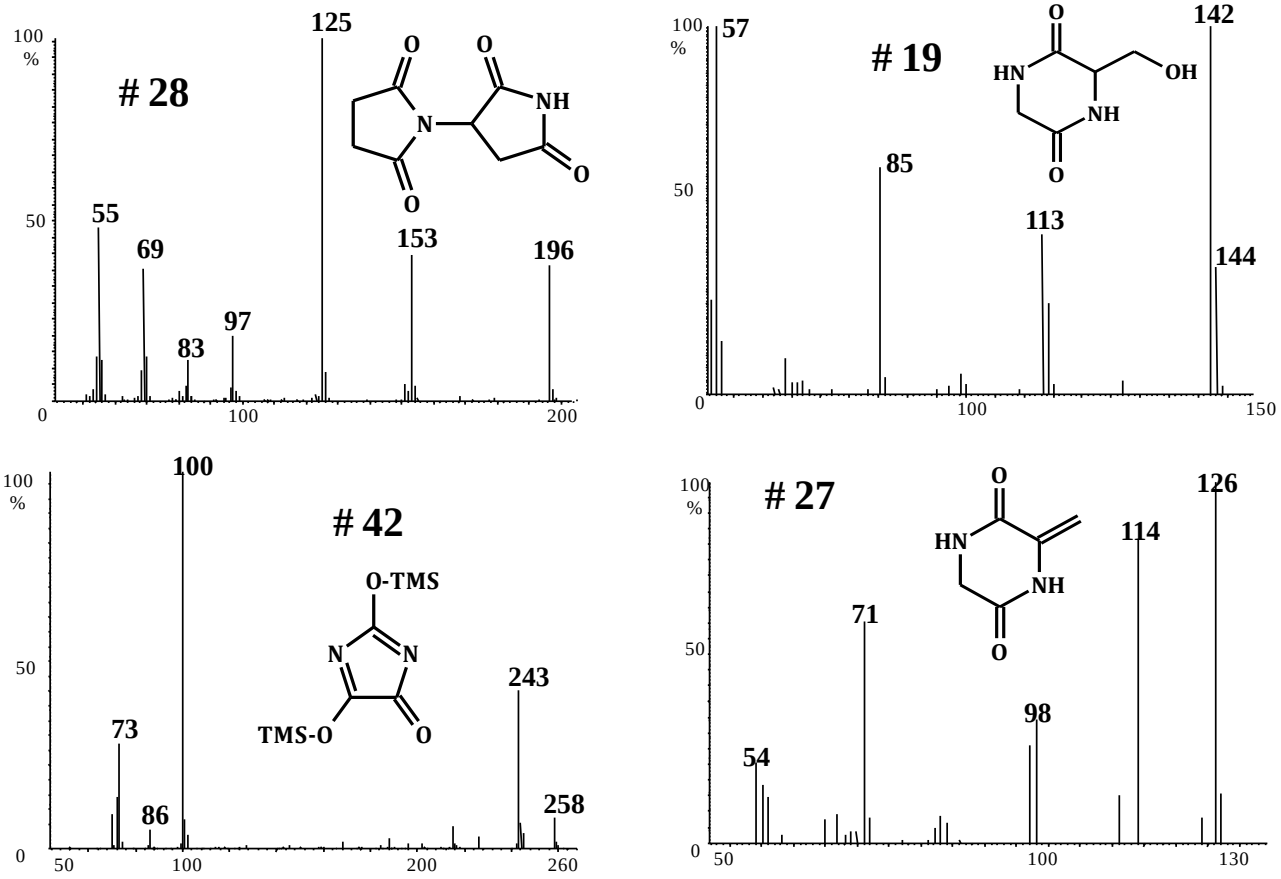

Figure 4.2.2 Mass spectra of selected TMS derivatives of 2,5-diketopiperazines (DKPs) with the tentative assigned molecular structure. Numbers # correspond to compound numbering in table 4.2.2

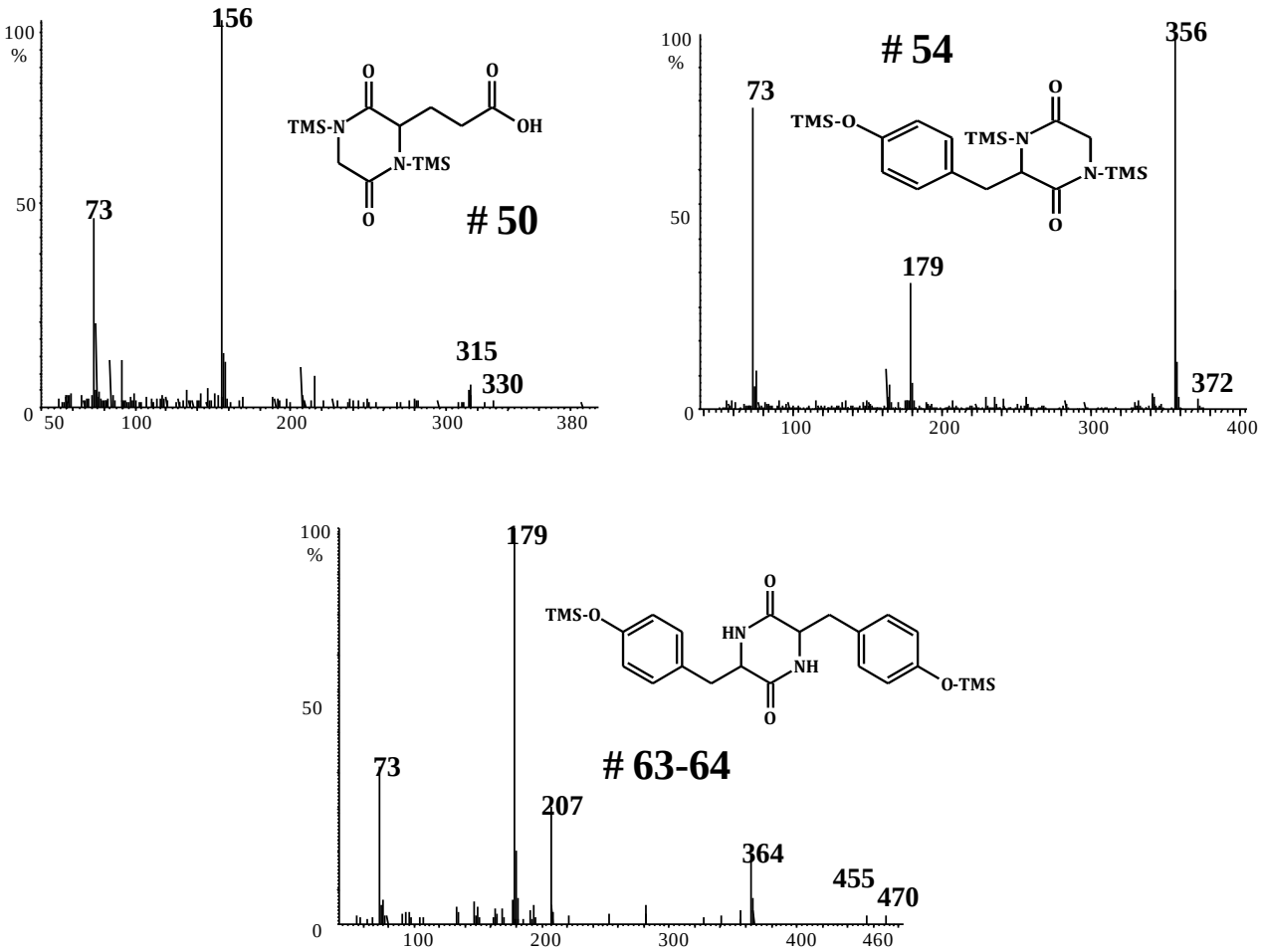

Figure 4.2.3 Extracted mass chromatogram at m/z 179, corresponding to silylated methyl phenol, obtained from the GC-MS analysis of Tyr-Tyr derivatized pyrolysate. Doublet of peaks marked by an asterisk (*****) are likely to correspond to DKPs.

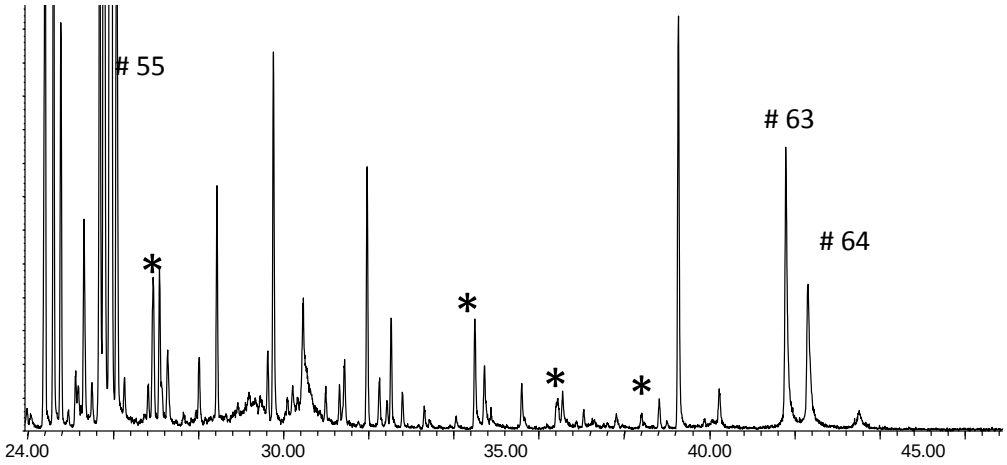

4.3. Pyrolysis of proteins

4.3.1 Off-line pyrolysis of collagen

Being a protein rich in Pro residues, collagen was selected to test the formation of DKPs containing Pro. A typical pyrogram reported in figure 4.3.1a shows that the most intense peaks in the elution region of DKPs were due to cyclo(Pro-Gly) (# 9), cyclo(Pro-Pro) (# 24) and cyclo(Pro-Hyp) (# 36) (along with its dehydrated derivative # 6) in accordance to the fact that Gly, Pro and Hyp (hydroxyproline) are the most abundant amino acids in collagen. In accordance to the occurrence of several Pro/Glu and Pro/Gln sequences in collagen (alpha-1 from bovine http://www.uniprot.org/uniprot/P02453), the cyclo(Pro-pyroGlu) # 41 was revealed in the chromatogram. The pyrogram resulting after silylation improved the detection of DKPs containing Gly which gave broad peaks in the underivatised form (see figure 4.3.1a, # 1 and 9) and sharp peaks in the silylated form (figure 4.3.1b, # 50 and 59, respectively). The silylated isomers of cyclo(Pro-Hyp) were clearly detected as two well separated peaks (# 70 and 71). However, neither the silylated cyclo(Pro-Arg) derivatives (# 77) nor the silylated cyclo(Pro-Lys) could be revealed in the mass chromatogram at m/z 174 (CH2=N(SiMe3)2) typical of these DKPs, even though collagene chains contain Pro/Arg and Pro/Lys sequences. Similarly, there were no peaks associated to the silylated cyclo(Pro-Asp) and cyclo(Pro-Glu).

4.3.2 Py-GC-MS of serum bovine albumin (BSA)

The information collected from off-line pyrolysis of peptide model compounds could be utilised in the identification of DKPs from conventional on-line Py-GC-MS analysis. This aspect was tested by analysing a common globular protein, BSA. The MS pyrogram of BSA in the full scan mode is reported in figure 4.3.2 with the indication of three main elution regions of pyrolysis products. The first elution region is that of the thermal fragmentation products of the lateral chain of aromatic amino acids (peaks labelled A-F, from toluene to indole) [55]. The elution region (G in figure 4.3.2) has many unidentified compounds, but corresponded to the elution of alkylated pyrrole/pyrrolidinediones [73]. The elution region of DKPs falls at higher retention times, where the most intense peaks are associated to the DKPs of neutral amino acids: cyclo(Pro-Leu) # 23/25 (the most abundant), Val-Leu #13/15, Leu-Leu # 21/22, Phe-Ala # 33/34, Phe-Val #37/39, Phe-Leu # 42/44. The GC peak profile of Pro containing DKPs was enhanced in the extracted chromatogram at m/z 70 (pyrrolidinium ion). The marker of Pro/Glu or Pro/Gln sequences, that is the cyclo(Pro-pyroGlu) #41 could be nicely detected. However, the peak height was much lower than that of the two cyclo(Pro-Leu) isomeric peaks even though the number of Pro/Glu, Pro/Gln sequences in BSA

is similar to that of Pro/Leu (http://www.uniprot.org/uniprot/P02769). Similarly, the number of Pro/Lys sequences in BSA is comparable to those of Pro/Leu, but the GC peaks associated to the pyrolytic markers of Pro/Lys (# 28, # 32) were of lower intensity than those of cyclo(Pro-Leu). Thus, the relative abundance of DKPs did not reflect the frequency of the corresponding amino acid sequences in the protein chain. The explanation is given by a different tendency of amino acids and peptides to form cyclic dipeptides [83, 85, 59]. Remarkably, even though the yields of DKPs from pyrolysis of BSA are rather low (estimated in μg g^{-1}, i.e. part per mil, [95]), the peaks # 38 and # 39 associated to a single Pro-Met sequence could be clearly revealed in the m/z 70 mass chromatogram (figure.4.3.2). Attempts to produce silylated DKPs by in situ derivatisation Py-GC-MS failed, thus the occurrence of DKPs with a polar amino acids observed in the pyrolyates of di and tripeptides could not be confirmed for representative globular (BSA) and fibrous (collagen) proteins under the analytical conditions here applied.

Figure 4.3.1 GC-MS trace (total ion) of the solutions obtained after off-line pyrolysis at 500 °C of collagen (a) underivatised, and (b) after trimethylsilylation. Peak numbers correspond to compounds listed in tables 4.1.1 and 4.1.2

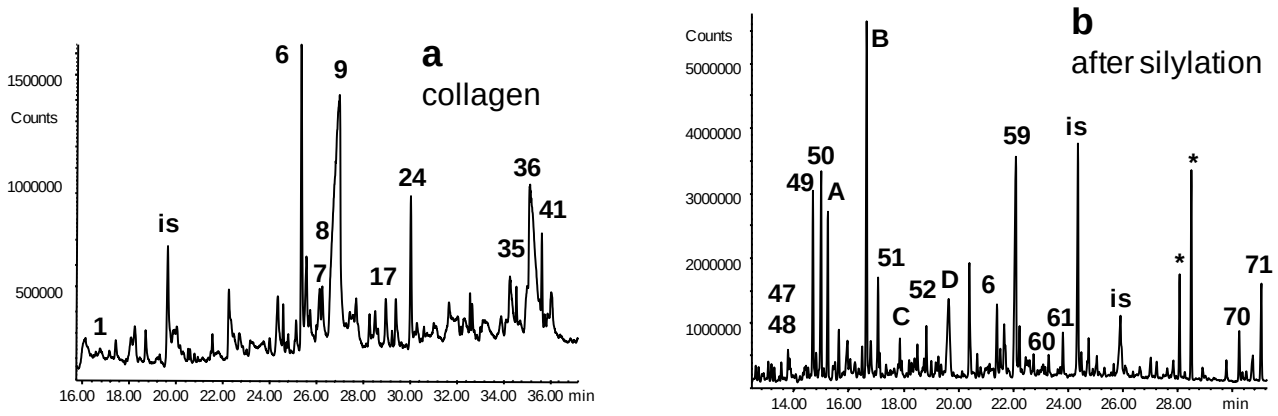

Figure 4.3.2 Total ion chromatogram (top) and extracted mass chromatogram at m/z 70 (bottom) obtained from Py-GC-MS of bovine serum albumin. A: toluene; B:phenol; C: 4-methylphenol; D: benzyl nitrile; E: benzenepropanenitrile; F: indole; G: pyrrole/pyrrolidine 2,4 diones from Leu-Leu [34]. Peak numbers correspond to compounds listed in tables 4.1.1 and 4.1.2.

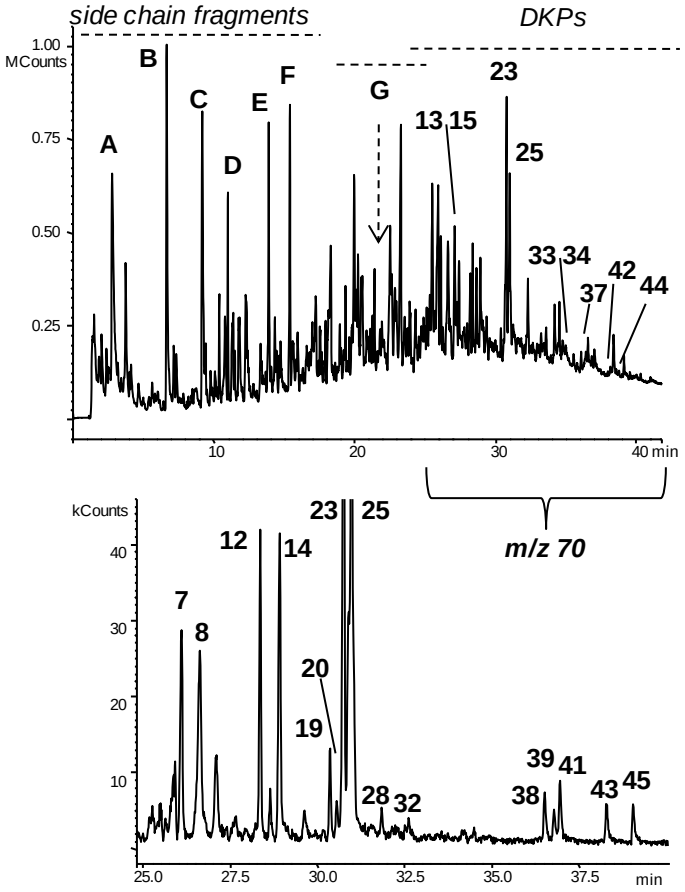

4.3.3 Lysozyme

Lysozyme was pyrolysed in order to test and eventually enhance the library of protein pyrolysis products in addition to the DKPs reported in the previous paragraph.The GC-MS trace of the underivatized lysozyme pyrolysate is reported in figure 4.3.3. Molecular characterizations of numbered peaks, together with the yields obtained from the sample protein pyrolysis calculated as $Wg_{analytes} / Wg_{sample,}$ are reported in table 4.3.1. The amounts of analytes produced from lysozyme pyrolysis were calculated as described in chapter 3, using sarcosine anhyidride as internal standard. The first elution region of the chromatogram is mainly featured by the presence of thermal degradation products of amino acids lateral chains, while at higher retention times there is the elution region of 2,5-diketopiperazine. Indole (peak #7) was found to be the principal pyrolysis products of lysozyme (4.6% , see table 4.3.1). This compound is mainly formed by the cleavage of tryptophan lateral chain [57]. Tryptophan is rather abundant in lysozyme sequence (Protein Data Bank ID

1LSY), where it accounts for the 4.8% of the amino acidic composition with 6 units per protein molecule. All the alkyl derivatives of indole (from peak # 8 to peak #10), which represent the main pyrolysis products in the underivatized GC pyrograms, were formed from tryptophan degradation. Succinimide (peak #2) is another abundant product of lysozyme pyrolysis that is reported in the literature to be formed by thermal degradation of asparagines and aspartic acid [62], which are among the protein most abundant amino acid, with 17 and 7 residues, (accounting for 9.5% and 4.8% of the amino acid composition respectively). Differently from the results reported from BSA pyrolysis, only small amounts of phenol and imidazole, including their derivatives, were recorded, since in the protein sequence this amino acids have rather low abundances (3 resiudes for Tyr and only 1 residue for His). On the other hand, lysozyme was the only protein for which succinimide was recorded to be produced upon pyrolysis. DKPs only account for a small fraction of the protein pyrolysate; this is probably due to the high percentage of polar amino acids and the low percentage of proline residues (3 residues). In fact, dipeptides are not easily formed during pyrolysis of polar amino acids while, as already said, proline was shown to promptly yields DKPs upon heating [59] and in addition, DKPs from Pro are considered rather stable [70]. The DKPs detected in lysozyme pyrolysate are formed from the cyclisation reactions of proline, leucine and glycine; the latter are rather abundant in the protein sequence. Leucine is in fact the most abundant amino acid with 15 residue accounting for more than the 10% of the protein sequence. Cyclo(Pro-Leu) is present in the lysozyme (peaks #22 and #23) as in the BSA pyrolysates, but not in collagen and ovalbumin. Cyclo(Pro-Gly) (peak #15) was detected in BSA and collagen pyrolysates at rather higher quantities respect to lysozyme (see paragraph 4.2), while it was not detected in ovalbumin pyrolysate. Cyclo(Leu-Leu) instead was detected in high amount (0.62% yield) only in lysozyme, while it was detected only in low amounts in BSA and was not detected in collagen and ovalbumin pyrolysates. Typical pyrolysis products of alanine, which is one of the most abundant amino acids in lysozyme (15 residues), were not detected in the underivatized pyrolysates. On the contrary, many DKPs were detected in the GC-MS trace of the silylated pyrolysates, shown in figure 4.3.3b. Molecular characterizations of numbered peaks, together with the yields obtained from the sample protein pyrolysis, are reported in table 4.3.2. The DKPs detected in the silylated pyrolysate are mainly derived from alanine cyclisation reactions with other amino acids such as alanine itself, valine and leucine.

Table 4.3.1 Principal pyrolysis products detected in lysozyme underivatized pyrolysate. Yields were calculated as $Wg_{analyte}/Wg_{sample}*100$ and are reported as the mean from n=2 pyrolysis.

#	R.T.	ANALYTES	Mean yields (‰)(n=2)	RSD(%)
1	9.7	Phenol-4-methyl	1.77	47
2	11.3	Succinimide	2.07	26
3	11.4	Benzyl-nitrile	0.53	20
6	14.4	Benzen-propan-nitrile	0.23	26
7	15.9	Indole	46.55	20
8	18.3	Indole, 3-methyl	5.30	15
9	20.8	Indole, 1-ethyl	0.44	23
10	21.0	Indole, 2,3-dimethyl	0.33	22
14	28.5	cyclo(Pro-Gly)	0.36	9
18	33.8	cyclo(Leu-Leu) 1	0.37	11
19	34.0	cyclo(Leu-Leu) 2	0.25	6
20	33.2	cyclo(Pro-Leu) 1	2.36	1
21	34.2	cyclo(Pro-Leu) 2	1.83	4

Table 4.3.2 Principal pyrolysis products detected in lysozyme silylated pyrolysate. Yields were calculated as $Wg_{analyte}/Wg_{sample}*100$ and are reported as the mean from n=2 pyrolysis.

#	R.T.	ANALYTES	Mean yields (‰)(n=2)	RSD(%)
1	11.9	Phenol-4-methyl-TMS	2.11	26
6	17.7	cyclo(Ala-Ala),bis-TMS 1	0.16	22
7	18.0	cyclo(Ala-Ala),bis-TMS 2	0.19	25
10	19.6	Indole N-TMS	16.78	20
11	20.3	cyclo(Ala-Val),bis-TMS 1	0.03	8
12	20.8	cyclo(Ala-Val),bis-TMS 2	0.03	30
14	21.8	cyclo(Ala-Leu),bis-TMS 1	0.09	61
15	22.0	cyclo(Ala-Leu),bis-TMS 2	0.08	33
16	22.1	Indole-3-methyl-N-TMS	2.29	12
17	23.3	cyclo(Gly-Leu)bis-TMS	0.11	39
21	28.0	cyclo(Pro-Gly) TMS	0.42	15

Figure 4.3.3 GC-MS trace (total ion) of the solutions obtained after off-line pyrolysis at 500 °C of lysozyme (a) underivatised, and (b) after trimethylsilylation. Peak numbers correspond to compounds listed in tables 4.3.1 and 4.3.2.

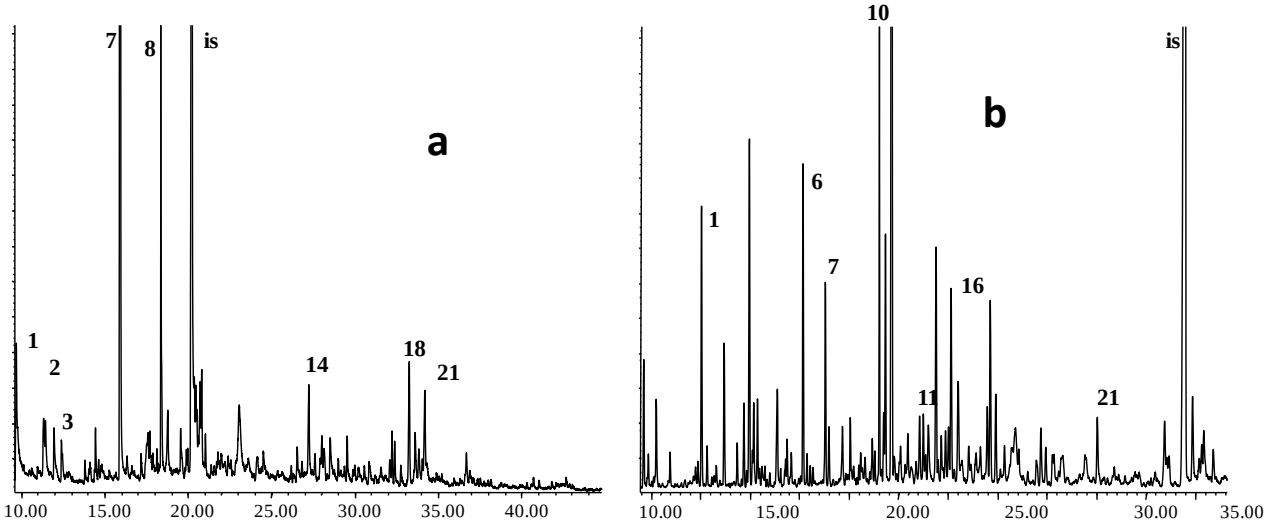

4.3.4 Ovalbumin

The GC-MS trace of the underivatized ovalbumin pyrolysate is reported in figure 4.3.5a. Molecular characterization of numbered peaks, together with the yield values obtained from the sample protein pyrolysis calculated as $Wg_{analytes}$ / $Wg_{sample,}$ are reported in table 4.3.3. The first elution region of the chromatogram is mainly featured by the presence of thermal degradation products of amino acid lateral chains, while at higher retention times there is the elution region of 2,5-diketopiperazine. DKPs peaks showed low signals in the GC-MS trace of the underivatized pyrolysate. The most abundant pyrolysis products deriving from the thermal degradation of the amino acids lateral chains are that evolved from the cleavage of phenolic units from tyrosine, indole derivatives from tryptophan, and benzyl nitrile from phenylalanine. The most abundant pyrolysis product detected in the underivatized pyrolysates is in fact indole, with the 1.16 % yield, followed by benzyl nitrile, benzyl propan nitrile and 4-methyl phenol. Also in this case, proline units were shown to promptly yields DKPs upon heating [59], being these the only DKPs detected in the underivatized pyrolysate, formed from the cyclisation of this amino acid with valine and leucine. The GC-MS trace of the silylated pyrolysate is reported in figure 4.3.5b. Molecular characterizations of numbered peaks, together with the yield values obtained from the sample protein pyrolysis are reported in table 4.3.4. The silylated pyrogram is rather rich of compounds, both deriving from cyclisation reaction and from amino acids lateral chains cleavage. Among them, it is interesting to notice the presence of

pyroglutamic acid, a product deriving from the self-cyclisation followed by cleavage of the glutamic acid lateral chain. The pyroglutamic formation reaction is shown in figure 4.3.4.

Figure 4.3.4. Pyroglutamic acid formation

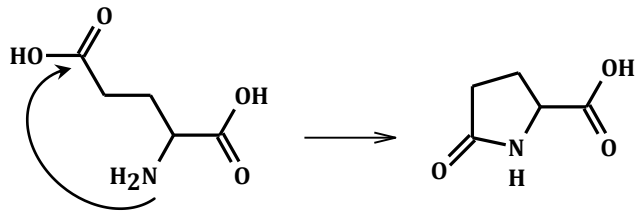

Glutamic acid is in fact one of the protein most abundant amino acid, with 33 resiudes for protein unit. The presence of the carboxylic group on the alpha carbon affect the chromatographic behavior of this compound, making its detection pretty difficult in the underivatized pyrolysate. On the other hand, the silylated pyrolysate is rich of cyclic dipeptides formed by cyclisation reaction of alanine, which is one of the most abundant amino acid in the protein sequence with 35 residue (Protein Data Bank ID 1OVA), with alanine itself, glycine, valine and leucine.

Table 4.3.3 Principal pyrolysis products detected in Ovalbumin underivatized pyrolysate. Yields were calculated as $Wg_{analyte}/Wg_{sample}*100$ and are reported as the mean from n=2 pyrolysis

#	R.T.	ANALYTES	Mean yields (‰)(n=2)	RSD(%)
1	9.7	4-methyl phenol	3.69	20
3	11.4	Benzyl nitrile	3.26	14
6	14.4	Benzyl propan nitrile	2.18	15
7	15.9	Indole	11.58	21
8	18.3	Indole, 3-Methyl	1.77	23
9	20.8	Indole, 1-ethyl	0.09	141
15	30.4	cyclo (Pro-Val) 1	0.37	5
16	31.1	cyclo (Pro-Val) 2	0.33	14
20	33.9	cyclo (Pro-Leu) 1	2.31	4
21	34.2	cyclo (Pro-Leu) 2	2.33	13

Table 4.3.4 Principal pyrolysis products detected in Ovalbumin silylated pyrolysate. Yields were calculated as $Wg_{analyte}/Wg_{sample}*100$ and are reported as the mean from n=2 pyrolysis

#	R.T.	ANALYTES	Mean yields (‰)(n=2)	RSD(%)
1	11.9	4-methyl phenol, TMS	3,86	22
2	13.9	Pyroglutamic acid-bis-TMS	1,36	15
3	14.9	Indole,3-acethyl-nitrile, N-TMS	0,86	14
4	17.5	Proline derivative 1	1,37	35
5	17.6	Proline derivative 2	1,22	33
6	17.7	cyclo(Ala-Ala)-bis-TMS 1	0,19	22
7	18.0	cyclo(Ala-Ala)-bis-TMS 2	0,22	17
8	18.9	cyclo(Gly-Ala)-bis-TMS	0,28	25
9	19.2	cyclo(Gly-Gly)-bis-TMS	0,62	23
10	19.7	Indole-N-TMS	6,01	12
11	20.3	cyclo(Ala-Val)-bis-TMS 1	0,07	29
12	20.8	cyclo(Ala-Val)-bis-TMS 2	0,06	33
13	21.6	cyclo(Gly-Val)-bis-TMS	0,23	18
14	21.9	cyclo(Ala-Leu)-bis-TMS 1	0,07	28
15	22.0	cyclo(Ala-Leu)-bis-TMS 2	0,05	25
16	22.1	Indole,3-methyl-N-TMS	1,27	16
17	23.3	cyclo(Gly-Leu)-bis-TMS	0,09	44

Figure 4.3.5 GC-MS trace (total ion) of the solutions obtained after off-line pyrolysis at 500 °C of ovalbumin (a) underivatised, and (b) after trimethylsilylation. Peak numbers correspond to compounds listed in tables 4.3.3 and 4.3.4.

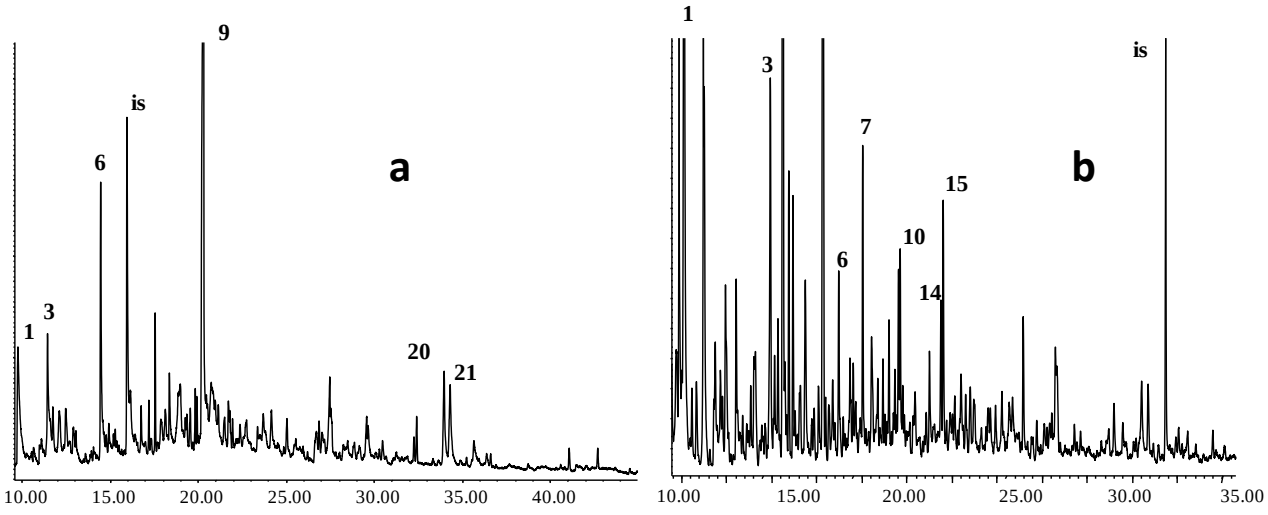

Chapter 5

Application of the analytical pyrolysis procedure to real samples

5.1 Analysis of bio-oil obtained from the pyrolysis of microalgae

5.1.1 Introduction

Biofuels from algae may represent a valid alternative to fossil fuels and conventional biofuels from terrestrial crops. From the point of view of energetic balance it was estimated that an algae cultivar with a growth rate 0.025 kilograms on squared meters for a day, producing 1 kilogram on cubic meter of raw algae biomass with a lipidic content of 20% on dry base, could produce a net amount of 928 GJ per hectare, while for a sugar cane cultivar, whose productivity assumes a typical value of 75 tons for year, the amount of energy obtained yearly is about 143 GJ per hectare [98]. An hypothetic cultivation system for biodiesel production from microalgae consists of :

- *Cultivation of microalgae in photobioreactor or open ponds, with water, nutrients, light and carbon dioxide supplying.*
- *Biomass harvesting by means of sedimentation and centrifugation*
- *Oil extraction and transesterification*
- *Utilization of the residual biomass for animal feeding, soil fertilizer and nutraceutical or cosmetics production*
- *Possible nutrient recycle*

Following a thorough economical analysis of the whole biodiesel production from microalgae process, conduced in 1996 from NREL (US National Renewable Energy Laboratory), the general opinion was that such a kind of biofuel production would have ended with a negative economic balance, since even in optimal algae growth conditions and an optimal photosynthetic productivity, prices of biofuels from algae would have been twice higher than that of fossil fuels. From then until now fuel price is more than doubled, driving scientific research to re-evaluate the possibility of using algal biomass as a source of renewable energy, also considering the growing concerns about global warming and so the necessity to use fuels with lower carbon dioxide emissions balance. As already mentioned, several aspects of the microalgae cultivation must be improved in order to make the bio-fuels production economically more competitive. To reach this scope, one of the most important aspects seems to be the selection of the microalgae species. This choice has to be established on a optimal combination of certain paramaters, such as high growth rate, high lipidic content and harvesting facility.

- Pyrolysis is a thermal process that occurs between 350-700°C in the absence of oxygen, capable to convert solid material into liquid, or bio-oil, gas, and a carbon residue called bio-char. Whenever it is possible to harvest and dry the biomass (depending on the selected biomass), pyrolysis gives the chance to convert the residual biomass in a bio-oil ash-free with intermediates features between lignocellulosic biomass and fossil fuels. This liquid product can be further fractionated into a hexane soluble fraction, which is spontaneously separated from the polar fraction which on the contrary results to be similar to bio-oils obtained from terrestrial lignocellulosic biomasses. The main advantage of direct pyrolysis of bio-diesel production residues, with respect to hydrothermal liquefaction or hydrothermal liquefaction followed by pyrolysis, is that no wastewater contaminated by polar compounds produced during pyrolysis is produced; if the biomass harvesting is relatively easy, this factor can justify exsiccation and pyrolysis of the biomass. In addition, a by-product of this process is the bio-char, a carbonaceous material with high nitrogen, phosphorous and minerals contents, that can be used as a low releasing fertilizer, closing the cycle of organic nutrients [99]. The results showed in this chapter were collected during a research project whose main scope was the screening of different algal species for biofuels production and evaluate the combustion characteristics of the products obtained upon pyrolysis.

The present section regards on the chemical characteristic of the obtained bio-oils were investigated, with particular attention to nitrogen containing organic compounds produced from microalgae proteins pyrolysis. In fact, algal biomass differs from terrestrial lignocellulosic biomass substantially for the higher content of proteins of the former, and hence on higher nitrogen content. The occurrence of nitrogen has a great impact on fuel properties and on its quality, for instance a possible enhanced production of NOx from nitrogen-containing organic compounds. Therefore, the knowledge of the chemical nature of nitrogen-containing compounds in pyrolytic liquids from microalgae is of great importance in fuel development (see section 1.2).

5.1.2 Tested algae

Botryococcus braunii

Botryococcus braunii is a unicellular green microalgae of the Chlorophycae class. This microorganism is able to convert the 3% of solar energy into hydrocarbons [100]. Since hydrocarbons are produced in a range of 30-75% of microalgae dry weight [101] it is considered as a possible renewable source of biofules. The chemical nature of the hydrocarbons produced from *B. braunii* allows to distinguish between different three different groups of algal strains:

- Group A - who synthesize n-alcadiens (C_{25}-C_{31})

- Group B - who synthesize triterpenoids, like botryococcenti (C_nH_{2n-10}, n=30-37)
- Group L - who synthesize a tetraterpenoids known as lycopadiene

The cultivated microalgae for *B. braunii* come from Göttingen University (Germany) and belongs to the strain SAG 807-1 of the group A.

Desmodesmus communis

Desmodesmus communis is afreshwater unicellular microalgae of the Chlorophycae class, often present in colonial from of 2 to 8 cells. Colonies are made of merged cells in a gelatinous substrate with every cell surrounded by a thick cellulosic membrane. These are desirable characteristics for microalgae cultivations in open ponds, since cells are able to resist to variable thermal conditions and to contamination from other microorganisms. Moreover, *Desmodesmus* is characterized by high growth rates and uptake of nutrients from the growth medium, making its cultivation promising in the field of phytodepuration [102]. The studied species is a native strain of the Forlì-Cesena province (Italia), isolated from a water sample of an artificial lake by G. Samorì in 2009, and initially identified as *Scenedesmus sp* before genetical analysis performed in 2012 allowed to identify it as *Desmodesmus communis*.

Nannochloropsis gaditana

Nannochloropsis gaditana is a marine unicellular microalgae belonging to the Eustigmatophyceae class. The cells have a spherical shape with 2 μm diameter and are rich of pigments like astaxanthin, zeaxanthin and cantaxanthin, and polyunsaturated fatty acids like omega-3 and omega-6 [103]. The high lipidic content together with a specific fatty acid composition and the common use of this species in open ponds cultivar make this a promising microalgae for the production of biofuels. More in detail, the *Nannochloropsis gaditana* species cultivated come from a strain isolated by C. Andreoli in 1999 from a water sample of Comacchio valley, in the Ferrara province (Italy).

5.1.3 Results and Discussion

Chemical analysis of algal biomasses

The chemical composition of microalgae biomasses was determined in terms of polysaccharides, proteins and total fatty acid content. Data were calculated as weight % on dry base and are summarized in table 5.1.1, together with the amounts of harvested biomass expressed as dry weight.

Tabel 5.1.1 Biomass composition values of the tested microalgae at the harvesting time are expressed as $\%_{wgt}$ on dry biomass.

	Botryococcus braunii	***Desmodesmus communis***	***Nannochloropsis gaditana***
Dry weight (mg/L)	1950	300	140
Polysaccharides (%)	22.5	32	17
Proteins (%)	7.5	21	25
Lipids (%)	48	9	25

Freshwater microalgae - *Botryococcus braunii* and *Desmodesmus communis* - were grown on modified Chu13 culture media [201], while f/2 [202] culture media with a 35% of salinity was used for *Nannochloropsis gaditana*. Culture media were kept under controlled conditions of light and temperature of 120µE m^{-2} s^{-1} and 20°C utilising a thermostat-controlled chamber equipped with fluorescent lamps at controlled luminous intensity. The lighting system was controlled by means of a timer, set on a 16 hours photoperiod of light and a 8 hours photoperiod of darkness. All the operations were carried out in a sterile hood and sterile materials to avoid contamination from bacteria, protozoa and other algal species. The cultivation technique used in this study is called "batch" and it consists of introducing small-medium quantities of algae inocula in sterilized Erlenmeyer flasks containing 1.5-2 liters of culture medium. Flasks were then placed in thermostated chambers. The microalgae cells were stirred by means of oscillators to increase nutrients uptake, gas exchange at the cell-water interface and light exposure. In batch cultivations the algal growth was monitored from the introduction of the inocula until the nutrients depletion in the culture media and the consequently arrest of algae reproduction. Generally, different growth stages could be observed. In the first stage algal cells get adapted to the new growth conditions, followed by a stage of exponential growth, and a stationary phase where algal growth is stopped due to exhaustion of nutrients or cell density effect which limits their further growth. This stage lasts until the occurrence of microorganisms death. The algal biomass of each studied species was collected in the advanced stationary stage of growth. Algal biomasses were recovered as slurry solutions in flasks to be subsequently freeze-dried prior to pyrolysis.

Bench scale pyrolysis

1 g of algal biomass was subjected to pyrolysis by means of a nitrogen fixed bed reactor. Nitrogen was fluxed at 1.5 L/min and the pyrolysis reactor temperature was set at 500°C. Biomasses were pyrolysed for 5 minutes and bio-oils were collected by means of two cold traps. The reactor and the pyrolysis conditions were described by Fabbri et al [104]. *Desmodesmus communis* and *N. gaditana* bio-oils were completely dissolved into acetone, while *B. braunii* bio-oil was dissolved first into

acetone and then in pentane because of its high hydrocarbons content. Pyrolysis conditions and amounts of bio-oil and char obtained from the pyrolysis of the tested biomasses are reported in table 5.1.2.

Table 5.1.2: Pyrolysis conditions and quantity of produced bio-oil and char for the tested microalgae.

	Pyrolyzed amounts (g)	**Temp. (°C)**	**Time (min)**	**Solvents -**	**Char (g)**	**Bio-oil (g)**	**Bio-oil Water content (g)**
Nannochloropsis gaditana	0.94	500	5	Acetone	0.45	0.52	**0.05**
Desmodesmus communis	1.04	500	5	Acetone	0.47	0.58	**0.04**
Botryococcus braunii	1.4	500	5	Acetone Pentane	0.45	0.45	**<0.004**

Bio-oil chemical analysis

Elemental analysis were performed on raw biomass, bio-oil and bio-char, by means of a CHNS analyzer. Ashes content was determined by combustion at 550°C for 5 hours. The oxygen content was estimated by difference. Results are shown in table 5.1.3. It was possible to calculate the higher heating values from this data using the equation reported in the literature by Channiwala and Parikhh [207]:

HHV=0.3491C+1.1783H+0.1005S-0.1034O-0.0151N-0.0211A(MJ kg-1)

Where C, H, N, O, S and A are respectively the single element content and the ash content expressed as weight percent on dry base. Higher heating values of each analysed fraction are reported, together with elemental analysis results, in table 5.1.3.

Table 5.1.3: Elemental composition of algal biomasses and higher heating value (HHV) of the respective pyrolytic fraction. Values are expressed as relative % of element content for each fraction and as MJ Kg^{-1} for HHV.

		N	**C**	**H**	**S**	**O**	**Ashes**	**HHV (MJ Kg-1)**
Nannochloropsis Gatidana	*Biomass*	4.0	25.0	4.8	0.6	33.7	31.9	10.2
	Bio-Char	3.6	21.1	1.6	0.9	6.1	66.7	7.2
	Bio-oil	6.1	62.6	8.6	0.1	22.7	0.0	29.5
Desmodesmus communis	*Biomass*	5.8	34.7	5.6	0.1	34.2	19.7	14.7
	Bio-char	5.5	37.4	3.0	0.0	10.4	43.7	14.5
	Bio-oil	8.7	62.4	8.3	0.1	20.5	0.0	29.3
Botryococcus Braunii	*Biomass*	1.5	44.3	6.8	0.1	27.6	19.8	20.2
	Bio-char	1.9	26.6	1.5	0.0	8.5	61.5	8.9
	Bio-oil	0.9	73.2	15.0	0.0	11.0	0.0	42.0

The relatively low energy contents of microalgae raw biomasses reported in table 5.1.3 show that the biomass direct combustion would be energetically uneconomical. This is mainly due to the high

ashes amounts in raw microalagae biomasses which reduces significantly their energy content. On the contrary, all the obtained bio-oils showed rather higher HHVs respect to the starting biomasses; in addition, their energy content is much higher of that tipically obtained from ligneocellulosic biomasses (lower than 20 MJ Kg^{-1}) and is comparable to that of biodiesel and bioethanol (39 and 29 MJ Kg^{-1} respectively). It is interesting to notice that for *Desmodesmus* and *Nannochlorpsis*, a greater part of nitrogen in the starting materials went into bio-oils respect to bio-chars. Counterwise, *Botryococcus* bio-char was the only bio-char for which a greater nitrogen content respect to the bio-oil was recorded.

Principal organic compounds in bio-oils were determined by GC-MS analyses. An aliquot of 1 mg of bio-oil was dissolved in acetonitrile (in *n*-hexane only for *Botryococcus braunii*) to obtain a 1% $_{wg}$ solution. 0.1 mL of a internal standard solution (sarcosine anhydride, see materials and methods, chapter 3) at 250 mg/L were added to 0.1 mL of bio-oil solution and then directly injected in the injection port of the GC-MS system. A fraction of the obtained solution was then placed in a vial with 0.1 mL of 1-oxo-4-benzyl-piperazinedion (silylation internal standard), 0.06 mL of BSTFA (Bis-trmethylsilyl-trifluoroacetamide) with a 1% of TMCS (trimethyl-chloro-silane). The solution was then heated at 60°C for 2 hours and added with ethylacetate and brought to the volume to 2 mL before the GC-MS analysis. Sample solutions were inserted under splitless conditions in the injection port of an Agilent 6850 chromatograph connected to an Agilent 5975 quadrupole mass spectrometer. Analytes were separated by a fused-silica capillary column (stationary phase poly (5% diphenyl/ 95% dimethyl) siloxane, 30 m, 0.25 mm i.d., 0.25 μm film thickness) using helium as carrier gas (at constant pressure, 33 cm s^{-1} linear velocity at 200 °C). The temperature programs and the quadrupole settings are reported in chapter 3 for both underivatized and silylated solutions. GC-MS traces of the underivatized solutions are reported in figure 5.1.1, figure 5.1.2 and figure 5.1.3. Numbered peaks are referred to table 5.1.7, in which molecular attributions for the principal peaks are reported. In table 5.1.4, table 5.1.5 and table 5.1.6 estimated % weight for each class of compounds are reported.

Figure 5.1.1 *Desmodesmus communis* bio-oil GC-MS trace. Peak numbers refer to compounds listed in table 5.1.7.

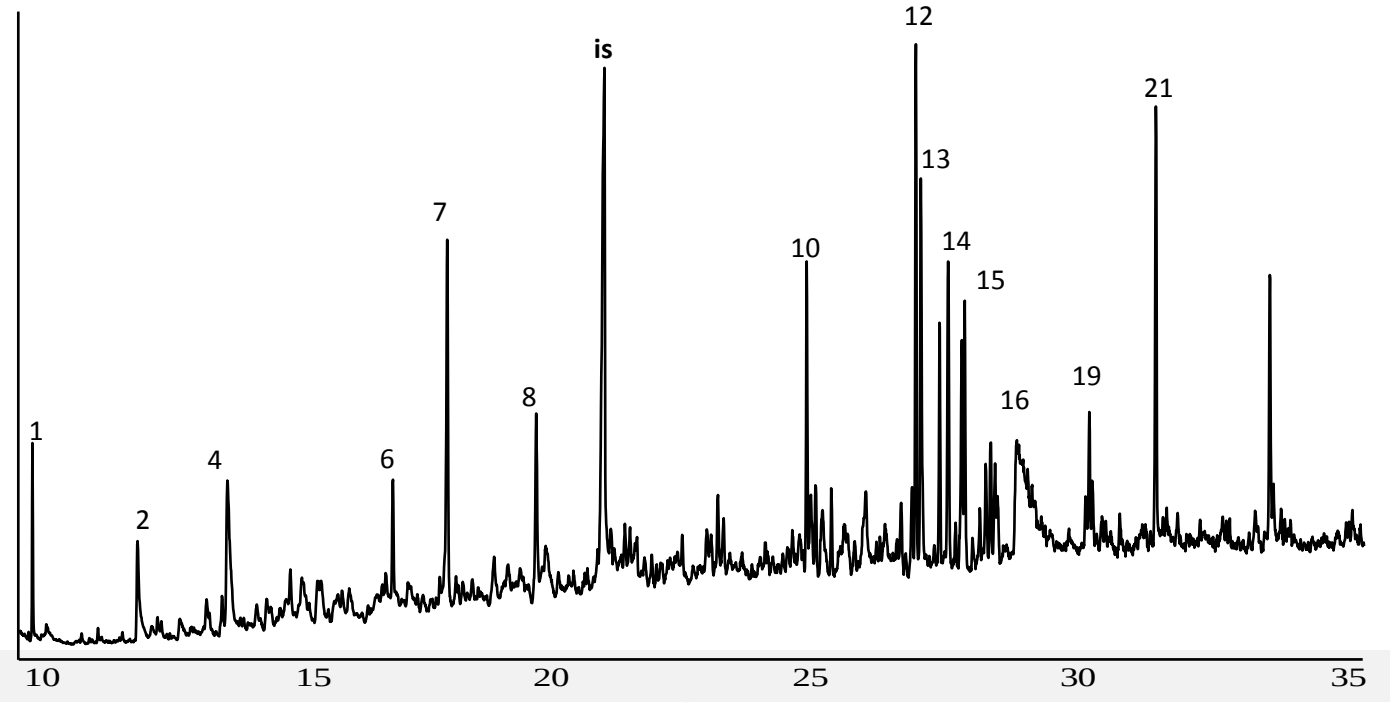

analysis.

***Desmodesmus communis* bio-oil**	
Analytes class	% g/g
DKP	*3.07*
Phenols	*0.65*
Furans	*0.15*
Nitrogenated aromatics	*1.55*
Nitriles and Amines	*0.42*
Pyrrolidions	*0.14*
Unknown	*0.08*
Fatty acids	*3.63*
Anhydrosugars	*1.19*
Sterols	*0.03*

Figure 5.1.2 *Nannochloropsis* bio-oil GC-MS trace. Peak numbers refer to compounds listed in table 5.1.7.

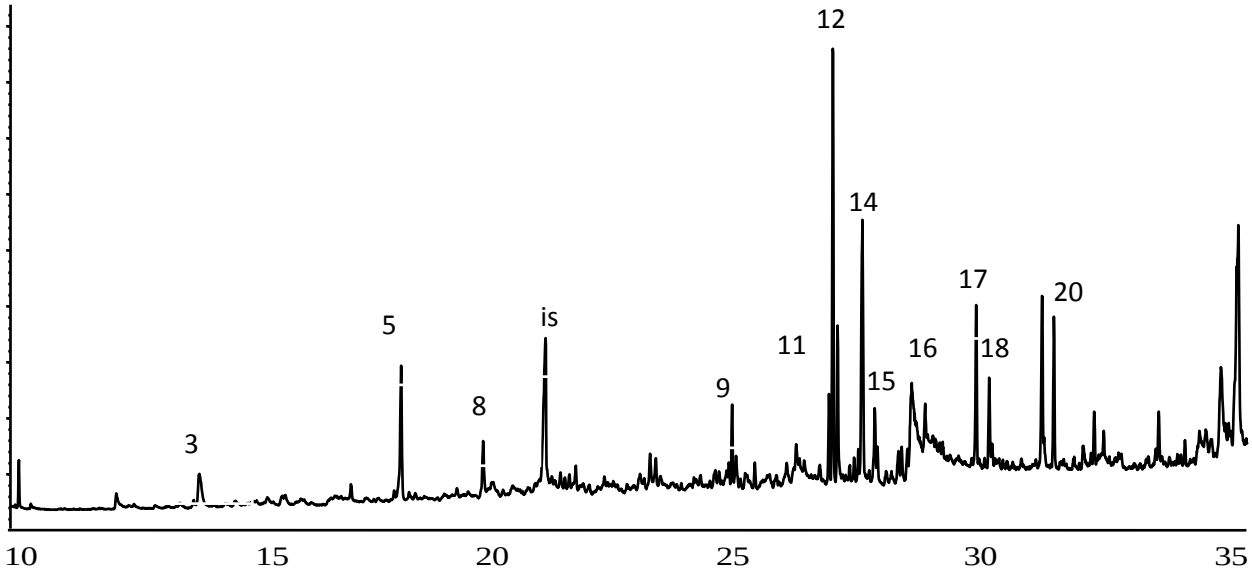

Table 5.1.5. Chemical composition of bio-oil from *Nannochloropsis gaditana* resulting from GC-MS analysis.

***Nannochloropsis gaditana* bio-oil**	
Analytes class	% g/g
DKP	2.37
Phenols	0.40
Furans	0.09
Nitrogenated aromatics	0.92
Nitriles and Amines	0.31
Pyrrolidions	0.08
Unknown	0.11
Fatty acids	6.73
Anhydrosugars	0.61
Sterols	0.43

Figure 5.1.3 *Botryococcus* bio-oil GC-MS trace

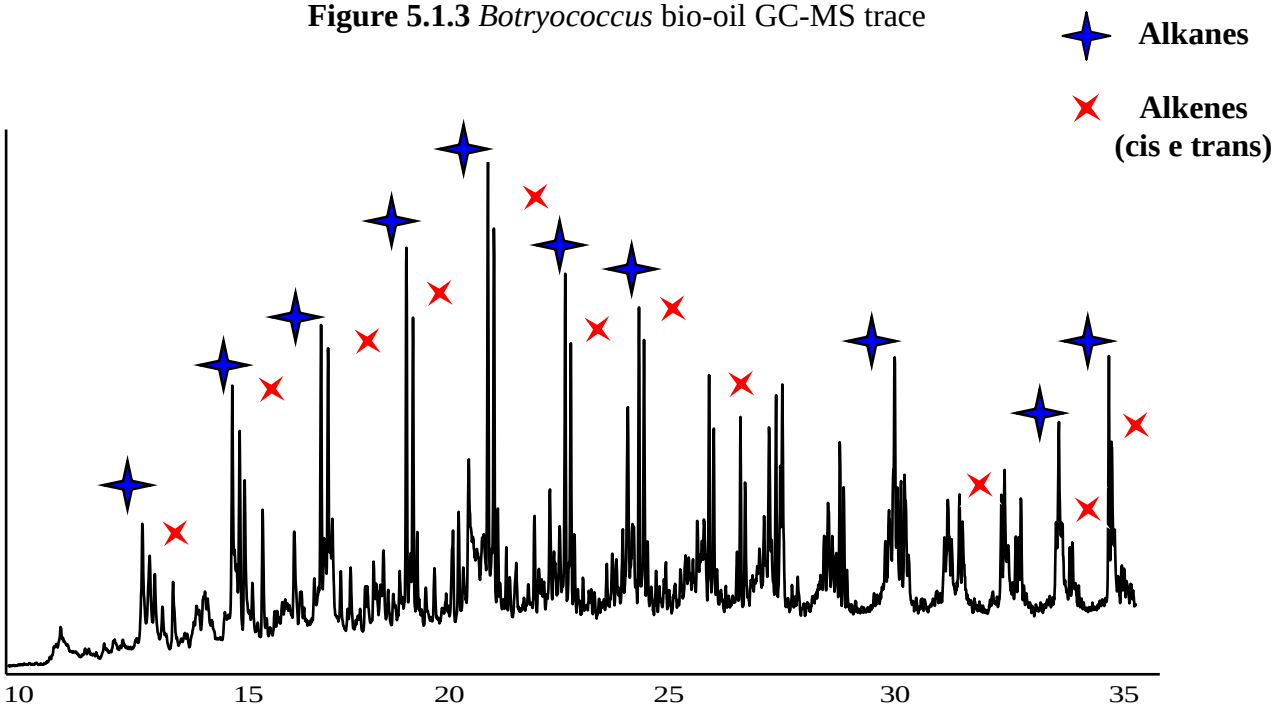

Table 5.1.6. Chemical composition of bio-oil from *Botryococcus braunii* resulting from GC-MS analysis. (n.d = not detected)

***Botryococcus braunii* bio-oil**	
Analytes class	% g/g
DKP	n.d
Phenols	n.d
Furans	n.d
Nitrogenated aromatics	n.d
Nitriles and Amines	n.d
Pyrrolidions	n.d
Unknown	15.00
Fatty acids	n.d
Anhydrosugars	n.d
Sterols	n.d
Hydrocarbons	85.00

Table 5.1.7 Molecular attribution of numbered peaks reported in the GC-MS traces of the bio-oil obtained from the microalgal biomasses (figures 5.1.1-5.1.3).

1 4-hydroxy -4-methyl pentan-2-one	**12** phytadiene 1
2 phenol	**13** cyclo(Pro-Leu)
3 corilon	**14** phytadiene
4 phenol-3-methyl	**15** hexaadecan-nitrile
5 benzylnitrile	**16** headecenoic acid
6 indole	**17** phytadiene
7 benzen-propan-nitrile	**18** phytadiene
8 methyl-indole	**19** octadecenenitrile
9 nitrogenated compund	**20** octadecenenitrile
10 heptadecane	**21** hexadecanamide
11 cyclo (Pro-Val)	

Over 80 compounds were identified and quantified in the microalgae bio-oils. Results are reported in terms of principal compounds classes in figure 5.1.4. Bio-oils obtained from *Desmodesmus communis* and *Nannochloropsis* were found to have a similar chemical composition, featured mainly by carbohydrates (anhydrosugars and furans) and lipids (fatty acids). An important fraction of both bio-oils is formed by compounds containing nitrogen, mainly deriving from thermal degradation of proteins (E.g., 2,5-diketopiperazines, DKP) and from secondary reaction of proteins with lipids (long chain aliphatic nitriles). Differently from them, *Botryococcus braunii* bio-oil is mainly featured by hydrocarbons presence.

Figure 5.1.4 GC-MS detectable fractions of the analysed bio-oils obtained from the pyrolysis of the microalgae. Numbers indicate the weight % calculated as wg(g) $_{analytes}$ // wg(g) $_{bio\text{-}oil}$.

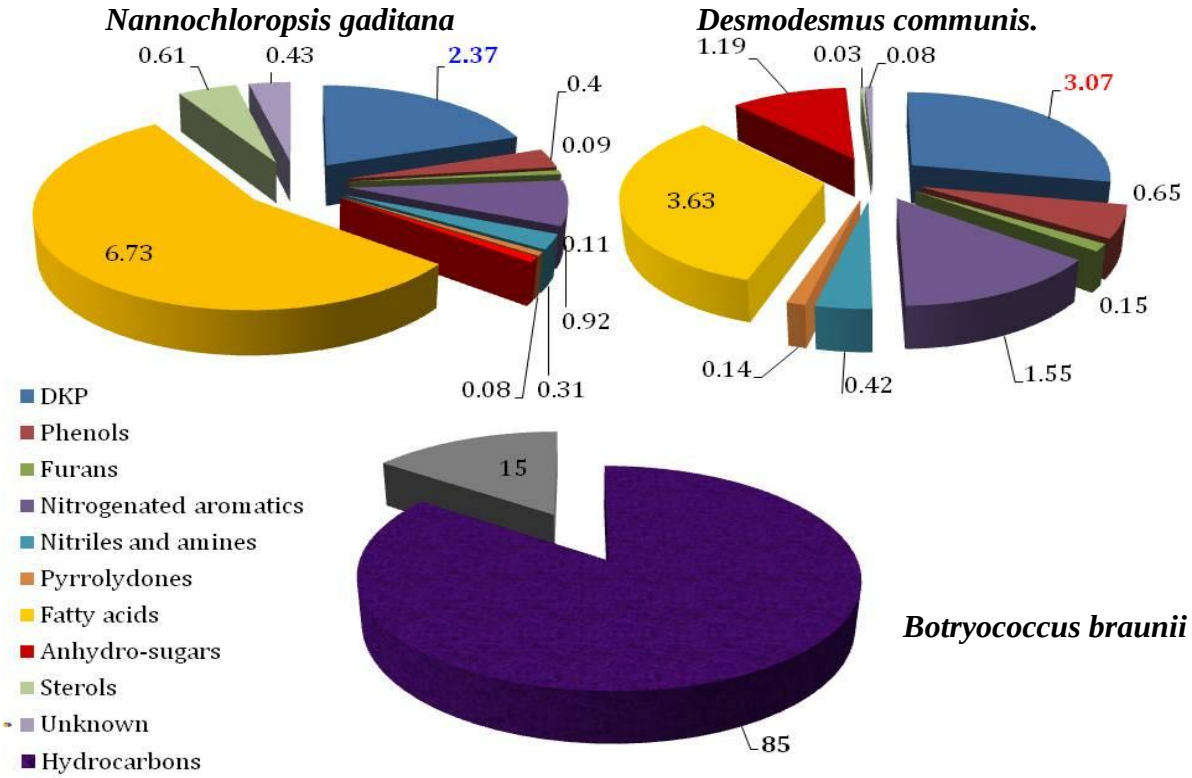

As showed in figure 5.1.4, *Desmodesmus communis* bio-oil has an higher content of DKPs respect to *Nannochloropsis*. The yields and the relative retention times of the DKPs detected in *Nannocloropsis* and *Desmodesmus communis* underivatized bio-oils are reported respectively in table 5.1.8 and 5.1.10. Yields are expressed as $Wg_{DKP}/Wg_{bio\text{-}oil}$ * 100. DKPs quantities were calculated using sarcosine anhydride as internal standard, as described in chapter 3. The most abundant cyclic dipeptide detected in the underivatized bio-oils was cyclo(Pro-Leu), for which similar yields were calculated for both the bio-oils. On the other hand, *Desmodesmus communis* bio-oil was featured by

an high content of pyrocoll (0.35% in table 5.1.10) that was detected only as a minor product in *Nannochloropsis* bio-oil (0.06% in table 5.1.8). Interestingly, the GC-MS traces of both the bio-oils were featured by a pattern of small peaks eluting at high retention times, which were attributed to cyclic derivatives of Pro-Glu and Pro-Lys, as the ones described in paragraph 4.1 evolved from pyrolysis of linear dipeptides. However, the TMS derivatives of these compounds were not detected in the silylated pyrolysates; this fact is probably due to the low amounts of these compounds in the analysed bio-oils for which the detected concentrations ranged from 0.01% to 0.04% (table 5.1.8 and 5.1.10) . The derivatisation procedure allowed the detection of the DKPs listed in table 5.1.9 for *Nannochloropsis* bio-oil and in table 5.1.11 for *Desmodesmus communis* bio-oil. In both the bio-oils, silylated derivatives of cyclic dipeptides containing Glycine and Alanine moieties were detected as the principal DKPs

Table 5.1.8 DKPs detected in *Nannochloropsis gaditana* bio-oil. Retention times were reported as relative retention times respect to anhydride sarcosine (is). RRT= 1- (RT_{is}/RT_{DKP}).

DKP from Nannochloropsis	Yields	RRT
Pyrocoll	0.06	0.21
cyclo(Pro-Ala) 1	0.09	0.22
cyclo(Pro-Ala) 2	0.07	0.23
dehydrogenated cyclo(Pro-Ala) 1	0.02	0.26
cyclo(Pro-Gly)	0.08	0.25
cyclo(Gly-Leu)	0.02	0.27
cyclo(Pro-Val) 1	0.10	0.28
cyclo(Pro-Val) 2	0.14	0.28
cyclo(Leu-Leu) 1	0.02	0.29
cyclo(Leu-Leu) 2	0.01	0.29
cyclo(Pro-pyrrole)	0.01	0.32
cyclo(Pro-Pro)	0.16	0.34
cyclo(Pro-Ile) 1	0.11	0.33
cyclo(Pro-Ile) 2	0.04	0.33
cyclo(Pro-Leu) 1	0.30	0.33
cyclo(Pro-Leu) 2	0.28	0.34
cyclo(Pro-Lys -NH3) 1	0.01	0.36
cyclo(Pro-Lys -NH3) 2	0.01	0.45
cyclo(Pro-Glu - H2O) 1	0.00	0.35
cyclo(Pro-Glu - H2O) 2	0.01	0.36
cyclo(Phe-Ala) 1	0.01	0.41
cyclo(Phe-Ala) 2	0.01	0.42
cyclo(PyroGlu-Gly)	0.01	0.47
cyclo(Pro-Met) 1	0.02	0.44

cyclo(Pro-Met) 2	0.02	0.44
cyclo(Val-Phe) 1	0.01	0.44
cyclo(Val-Phe) 2	0.01	0.45
cyclo(Phe-Leu) 1	0.01	0.46
cyclo(Phe-Leu) 2	0.01	0.47
cyclo(Pro-Phe) 1	0.03	0.46
cyclo(Pro-Phe) 2	0.03	0.47
cyclo(Pro-Lys-NH_3/ H_2) 1	0.01	0.39
cyclo(Pro-Lys-NH_3/ H_2) 2	0.01	0.39
cyclo(Pro-PyroGlu)	0.01	0.45

Table 5.1.9 DKPs detected in *Nannochloropsis gaditana* silylated bio-oil. Retention times were reported as relative retention times respect toTMS derivative of 1,3 benzyl-oxo-piperazine (is). RRT= 1- (RT_{is}/$RT_{DKP-TMS}$).

DKP TMS derivative	Yields	RRT
cyclo(Ala-Ala) 01 TMS	0.08	-1.01
cyclo(Ala-Ala) 02 TMS	0.08	-0.95
cyclo(Gly-Ala) TMS	0.13	-0.81
cyclo(Gly-Gly) TMS	0.10	-0.75
cyclo(Ala-Val) 01 TMS	0.02	-0.62
cyclo(Ala-Val) 02 TMS	0.05	-0.57
cyclo(Gly-Val) TMS	0.05	-0.50
cyclo(Ala-Leu) 01 TMS	0.04	-0.48
cyclo(Ala-Leu) 02 TMS	0.06	-0.47
cyclo(Ala-Ile) 01 TMS	0.03	-0.47
cyclo(Val-Leu) 01 TMS	0.01	-0.29
cyclo(Val-Val) 02 TMS	0.002	-0.29

Table 5.1.10 DKPs detected in *Desmodesmus communis* bio-oil. Retention times were reported as relative retention times respect to anhydride sarcosine (is). RRT= 1- (RT_{is}/RT_{DKP}).

DKP from *Desmodesmus communis*	Yields	RRT
Pyrocoll	0.29	0.21
cyclo(Pro-Ala) 01	0.16	0.22
cyclo(Pro-Ala) 02	0.10	0.24
dehydrogenated cyclo(Pro-Ala) 01	0.02	0.26
dehydrogenated cyclo(Pro-Ala) 02	0.02	0.26
cyclo(Pro-Gly)	0.17	0.25

cyclo(Gly-Leu)	0.08	0.27
cyclo(Pro-Val)	0.25	0.28
cyclo(Leu-Leu) 01	0.01	0.29
cyclo(Leu-Leu) 02	0.01	0.29
cyclo(Pro-pyrrole)	0.01	0.32
cyclo(Pro-Pro)	0.22	0.34
cyclo(Pro-Ile) 01	0.11	0.33
cyclo(Pro-Ile) 02	0.05	0.33
cyclo(Pro-Leu) 01	0.37	0.33
cyclo(Pro-Leu) 02	0.36	0.34
cyclo(Pro-Lys -NH3) 01	0.01	0.36
cyclo(Pro-Lys -NH3) 02	0.01	0.45
cyclo(Pro-Glu - H2O) 01	0.01	0.35
cyclo(Pro-Glu - H2O) 02	0.01	0.35
cyclo(Phe-Ala) 01	0.01	0.41
cyclo(Phe-Ala) 02	0.01	0.42
cyclo(PyroGlu-Gly)	0.01	0.47
cyclo(Pro-Met) 01	0.01	0.44
cyclo(Pro-Met) 02	0.02	0.44
cyclo(Val-Phe) 01	0.01	0.44
cyclo(Val-Phe) 02	0.01	0.45
cyclo(Phe-Leu) 01	0.01	0.46
cyclo(Phe-Leu) 02	0.01	0.47
cyclo(Pro-Phe) 01	0.04	0.46
cyclo(Pro-Phe) 02	0.04	0.47
cyclo(Pro-Lys-NH_3/ H_2) 01	0.02	0.39
cyclo(Pro-Lys-NH_3/ H_2) 02	0.01	0.39
cyclo(Pro-Lys-NH_3/ H_2) 03	0.01	0.37
cyclo(Pro-PyroGlu)	0.04	0.45

Table 5.1.11 DKPs detected in *Desmodesmus* silylated bio-oil. Retention times were reported as relative retention times respect toTMS derivative of 1,3 benzyl-oxo-piperazine (is). RRT= 1-($RT_{is}/RT_{DKP\text{-}TMS}$).

DKP TMS derivative	Yields	RRT
cyclo(Ala-Ala) 01 TMS	0.04	-1.01
cyclo(Ala-Ala) 02 TMS	0.04	-0.95
cyclo(Gly-Ala) TMS	0.06	-0.81
cyclo(Gly-Gly) TMS	0.08	-0.75
cyclo(Ala-Val) 01 TMS	0.01	-0.62
cyclo(Ala-Val) 02 TMS	0.02	-0.57
cyclo(Gly-Val) TMS	0.03	-0.50
cyclo(Ala-Leu) 01 TMS	0.02	-0.48
cyclo(Ala-Leu) 02 TMS	0.03	-0.47
cyclo(Ala-Ile) 01 TMS	0.03	-0.46
cyclo(Val-Leu) 01 TMS	0.01	-0.29
cyclo(Val-Val) 02 TMS	0.01	-0.28

5.1.4 Conclusions

Pyrolysis showed to be an interesting treatment for the upgrading of microalgae biomass into potential feedstock for fuel production. In fact, in the cases of *Nannochoropsis* and *Botryococcus* pyrolysis was able to convert into a liquid fuel more than 60% of the energy content of the starting material, segregating at the same time a significant amount of carbon and all the ashes into bio chars. On the other hand, *Desmodesmus* was the only biomass which was found to produce upon pyrolysis a bio-char with an higher energy content with respect to bio-oil. Significant amounts of nitrogen were retained into *Nannochloropsis* and *Desmodesmus* bio-oils, while *Botryococcus* bio-oil resulted to retain only low amount of this element. However, for all the microalgae great part of the nitrogen in the starting material was retained into bio-char. The analytical method illustred in chapter 4 allowed to characterize the chemical composition of the obtained bio-oils by GC-MS analysis. The GC-MS traces of the bio-oils showed rather abundant amounts of nitrogen containing compounds for all the tested algae, with the exclusion of *Botryococcus braunii* bio-oil whose composition was found to be similar to that of mineral fuels. DKPs were found to be the most abundant nitrogen containing compounds inside microalgae bio-oils. The presence of nitrogen inside biofuels can cause many problems, e.g. the emission upon combustion of nitrogen oxides. Further studies in catalytic pyrolysis could be focused on the segregation of nitrogen in the carbonaceous solid residue produced upon pyrolysis, which could then be used for interesting applications in agriculture as a fertilizer. Quantitative results showed that only a bio-oil minor fraction of *Nannochloropsis* and *Desmodesmus* could be characterized by means of gas chromatography, suggesting the existence of a greater non-volatile fraction of unknown chemical nature.

5.2 Chrysotile/BSA interaction

5.2.1 Introduction

Asbestos is a commercial term encompassing some magnesium silicates which crystallize in fibrous forms, including chrysotile, $Mg_3Si_2O_5(OH)_4$, by far the most widespread material of this type [105]. These fibers belonging to the serpentine minerals are constituted of stacking layers of silica $(Si_2O_5)_n^{-2n}$ sheet linked to octahedral brucite sheet $[Mg_3O_2(OH)_4]_n^{+2n}$. A slight misfit between the sheets induces curling to constitute concentric cylinders with the brucite layers outwards [106, 107]. The chrysotile stoichiometric composition $[Mg_3Si_2O_5(OH)_4]$ results strongly affected by the presence of many impurities and ion substitutions which differ as the function from the ores were the mineral samples arise [108]. The presence of impurities, ion substitutions and structural disorder in mineral chrysotile fibers affects not only its morphology and chemical-physical properties, but also the biological-mineral system interaction [109, 110]. Health hazards associated with asbestos are well documented in the medical and general health literature and its deleterious environmental effects are now well known [111]. The molecular mechanisms underlying the fibrogenic and tumorigenic effects of asbestos are not yet fully understood, but different physico-chemical factors seem to be involved, such as size, surface reactivity, chemical composition and level of contaminants [112, 113]. The physicochemical properties of asbestos fibers are also responsible for their solubility, biodurability, and biopersistence [114]. The fibers properties that are related to their cytotoxicity [115, 116] and mutagenic responses [117] are strongly affected by the surface chemical adsorption of biological molecules and macromolecules, such as proteins, cell-membrane lipids, and nucleic acids [118]. Alterations in these essential cellular components can alter cell functions and hence drive the cell to either neoplastic transformation or apoptosis. The adsorption of serum macromolecules, such as fibronectin and albumin, onto mineral asbestos fibers has been studied to obtain information about the phagocytosis and toxicity of asbestos fibers for mesothelial cells [119]. Albumin, the major plasma protein, is a highly soluble protein that can be prepared at concentrations of up to 30% (w/v) [120]. This property is related to its negative charge at neutral pH. The amino acid sequence of albumin is characterized by unusually high percentages of cysteine [139] and charged amino acids, and low percentages of tryptophan, glycine, and methionine [121, 122]. Additionally, and unusually for extracellular proteins, it possesses a single, free sulfhydryl (Cys 34) and has no sites for enzymatic glycosylation [123, 124]. Geoinspired chrysotile nanocrystals have been synthesized as a unique phase with definite structure, morphology and chemical composition to be as a standard reference sample for the investigation of the molecular interaction between chrysotile fibers and biological systems [36, 125]. The synthetic chrysotile nanocrystals have an hollow tubular

morphology in which two or three tubular subunits are concentrically arranged in a telescopic form around a central hole of 7 nm of diameter [126, 127]. The geoinspired synthetic chrysotile fibers, with stoichiometric composition [$Mg_3Si_2O_5(OH)_4$], in contrast to natural ones, do not exert any significant cytotoxic effect [128]. In fact the incorporation of foreigner ions and the presence of surface active metal ions are considered implied with natural chrysotile fibers cytotoxicity and genotoxicity [129,130]. The first morphological evidence of both bovine serum albumin (BSA) and human serum albumin (HSA) adsorption onto synthetic stoichiometric chrysotile nanocrystals has been obtained, and serum albumin secondary structure modifications induced by the surface interaction have been quantified by FTIR spectroscopy on the HAS/BSA-coated chrysotile nanocrystals [131, 132] and circular dichroism (CD) investigations on the protein solution exchanged from the chrysotile surface [133]. Also, the HSA secondary structure modifications induced by the chrysotile surface have been studied via MD and experimental FTIR methods [132]. The present study give strong support to the atomistic computer simulations as a powerful tool to provide a realistic description of the mechanism of the adsorption process of plasma proteins on the chrysotile surface, which can be quantitatively investigated by FTIR spectroscopy, gaining insight into the mechanism of asbestos toxicity. Fe doped chrysotile fibers have been synthesized as single–tube nanocrystals with a central hole diameter of 7± 1 nm and wall thickness of about the same dimension [131]. They show structure modifications as function of the Fe doping extent which affect their morphological aggregation. In fact the flattening of the curved brucite layers observed in the Fe doped chrysotile crystals resembling the planar morphology characteristic of lizardite occurs so much is higher the Fe doping extent [131]. This morphological modification has been observed when Fe preferentially replace Si resembling lizardite structure [38]. Infrared and Raman spectroscopic analyses have been utilized to investigate Mg and/or Si ions replacement by Fe ions in chrysotile structure as a function of the Fe doping extent. The results highlight that Fe can replace both Mg and Si, differently modifying the chrysotile structure as a function of the Fe doping extent and the Fe doping process appears strongly affected by the presence of metallic Fe in the synthetic environment. In fact, octahedral co-ordinated Fe has been observed in all the substitution range in Fe-doped chrysotile synthesized in absence of metallic Fe. On the contrary, tetrahedral co-ordinated Fe inducing a flattening of the chrysotile structure appears prevalent in respect of octahedral co-ordinated Fe in highly Fe-doped chrysotile synthesized when metallic Fe is available in the synthetic environment [131]. Furthermore, the structural modifications induced by Fe doping alter the mechanical properties of the geoinspired chrysotile nanocrystals, causing an increase of its Young's modulus up to redouble [132]. However genotoxic and cytotoxic evaluations carried out on Fe doped

geoinspired chrysotile nanocrystals has highlight as the generation of reactive oxygen species and other radicals catalyzed by iron ions in the chrysotile fibers is potentiated when Fe ions are organized into specific chrysotile crystallographic sites having coordinanation states able to activate free radical generation [133]. These data can explain the role of Fe on the toxicity of natural chrysotile fibers which has been widely investigated. In fact considerable in vitro and in vivo evidence suggests that free radicals, especially iron catalysed HO and reactive nitrogen species, have a pivotal role in causing asbestos associated diseases [133-135]. The available data also suggest that the iron content of asbestos, as well as redox active iron associated with or mobilised from the surface of the fibers, is important in generating $HO^{\cdot}$. The location of the sites responsible for catalytic and redox activity asbestos Fe mediated is currently unknown even if the fibers surface appear mainly to control the Fe reactivity. In fact at neutral pH Fe^{3+} is stable and has a very low water solubility [136]. By EPR, Mossbauer, DRS spectroscopic analyses and magnetic investigations, Mg and/or Si ion replacement by Fe^{3+} in a synthetic geomimetic chrysotile structure has been investigated. The results highlight that, as a function of the Fe doping extent and of the Fe doping process, iron can replace both Mg and Si sites. The contemporary iron substitution into the octahedral and tetrahedral sheets is associated with the presence of both isolated Fe^{3+} centres in high-spin 3d5 configuration (S = 5 2, 6A1(6S)) in Oh and Td symmetry and intra-lattice clustered species. Increasing the Fe doping extent increases the concentration of aggregated species, while magnetic susceptibility confirms a paramagnetic anisotropy [137]. In addition, Mossbauer and EPR revealed isolated iron ions in octahedral sites that undergo both axial and rhombic distortion and the occurrence of aggregated iron ions and/or extra-framework clustering. A linear relationship between the formation of carbon-centred radicals and the amount of rhombic-distorted isolated iron sites was found. Even the smallest iron contamination imparts radical reactivity, hence toxicity, to any chrysotile outcrop, thereby discouraging the search for non-toxic chrysotile. The use of model solids that only differ in one property at a time appears to be the most successful approach for a molecular understanding of the physico-chemical determinants of toxicity [138]. Also the knowledge of the surface charge state of chrysotile in aqueous electrolyte solutions is fundamental in understanding the injurious interactions between asbestos fibers and biological environment [136,39].

Several works describing the mechanism of diketopiperzines (DKPs) formation during pyrolysis are reported in the literature [75, 83, 89, 186]. Most authors agree that DKPs are one of the most abundant primary pyrolysis products of proteins. The thermo-chemical path responsible of their formation seems to be influenced by temperature and the type of amino acids involved. DKPs evolving from proteins pyrolysis are formed by the cyclisation of couples of amino acids contiguous in the protein sequence; this means that DKPs are capable to give punctual information on the

proteins primary structure. Polar amino acids however are supposed to interact differently with the brucite layer respect to neutral amino acids [146]. Since DKPs formed by this amino acids are not detectable without derivatization, a sylilation procedure was developed for the analysis of DKPs containing polar amino acids. In particular, the procedure was focused on the two most abundant amino acid in BSA sequence, lysine and glutamic acid. Attention was also paid to the lateral chain fragmentation products of amino acid like tyrosine and triptophan, which can be strictly involved in the interaction with chrysotile surface. In order to investigate the effect of Fe substitution in chrysotile structure in modifying the surface composition, structure, charge distribution and reactivity we have studied the structural modification of bovine serum albumin (BSA) adsorption on stoichiometric chrysotile and chrysotile Fe-doped on the base of analytical pyrolysis, FT-IR and TGA.

5.2.2 Materials and methods

Synthetic chrysotile nanofiber.

A hydrothermal synthesis reactor (Parr Stirred "Mini" reactor model 4652) with a 500 cm^3 moveable vessel constructed with "alloy C-276" (a metal alloy that contains 6.5 wt% Fe) was used to carry out the hydrothermal reaction of SiO2—with Aerosil 380 as a powder with a surface area of about 380 m^2g^{-1} (Eigenmann and Veronelli S.p.A.)—and $MgCl_2$ in an aqueous NaOH solution up to pH 13 and at temperature of 300° C on the saturated vapour pressure curve (82 atm) with a run duration of 24 h. The precipitate removed from the solution was repeatedly washed with deionised water before being dried for 3 h at 150° C. In order to synthesize the series of Fe-doped chrysotile samples, a gel mixture of SiO2, FeCl3 and MgCl2 in an aqueous solution was prepared. The pH of the gel mixture, which contained an Si/(Mg+Fe) molar ratio in the range of 0.6–0.7, was adjusted to 13 by means of an aqueous NaOH solution. Concentrations of $MgCl_2$ and $FeCl_3$ ranging from 9.75 up to 10 mm were used. The precipitate removed from the solution was repeatedly washed with deionised water before being dried for 3 h at 150° C.

Sample preparation of BSA-Chrysotile nanofiber adducts

Samples of adsorbed bovine serum albumin were prepared by mixing 40mg of inorganic phase with 10 ml of protein dissolved at 5 mg/ml in phosphate buffer (0.010M Na2HPO4, 0.140M NaCl, 0.003M KCl) pH 7.4 in 10 ml polyethylene tubes. The mixture was rotated end-over-end at 37 ◦C for 16 h. For the FT-IR spectroscopic investigation, the solid was recovered by centrifuging at 12,700×g for 3min and freeze-drying at −60 ◦C under vacuum (3 mbar) for 12 h while the supernatant solution was assayed for protein content by means of UV spectroscopy (λ = 278 nm, εBSA = 42,000M−1

cm−1). The amount of adsorbed protein was calculated as difference between the concentrations of the initial solution and that of the supernatant.

Off-line pyrolysis

Pyrolysis was performed on pure BSA, BSA-stoichiometric chrysotile and BSA-Fe doped chrysotile adducts. The apparatus employed for off-line pyrolysis experiments was described elsewhere [147]. Briefly, it consists in a pyrolysis chamber fitted for a pyroprobe model 1000 (CDS Analytical Inc.) equipped with a resistively heated platinum filament. A sample holder quartz tube containing an exactly weighed amount of sample (about 7-10 mg) was introduced into the platinum coil and the probe was in turn inserted into the pyrolysis chamber. The apparatus was fluxed with a nitrogen stream at 200 ml min^{-1} prior to pyrolysis. The exit of the pyrolysis chamber was connected through a Tygon® tube to a cartridge for air monitoring containing a XAD-2 resin as adsorbent (orbo-43) purchased from Supelco. In order to collect higher amounts of pyrolysis products, several pyrolysis were performed with the same cartridge on the same BSA-chrysotile samples adducts, in order to collect more pyrolysis products. After pyrolysis, the cartridge was eluted with 5 mL of acetonitrile. The solutions were collected, concentrated under a gentle nitrogen stream and spiked with 0.1 mL of 250 mg l^{-1} of sarcosine anhydride solution in ACN before being analyzed in GC-MS. DKP yield values were calculated from the resulting total ion current (TIC) chromatogram using a single point calibration performed on cyclo(Gly-Leu), both for the underivatized that for the silylated solutions. All the other compounds were quantified using a response factor of 1:1. Yield values were calculated by the formula $Wg_{analytes}$ / $Wg_{ads.BSA}$ *100, with $Wg_{ads.BSA}$ being the amount of adsorbed BSA on synthtetic chrysotile surface, determined by means of UV spectroscopy as the difference between BSA concentration in the initial solution and that of the supernatant.

Silylation

An aliquot of the acetonitrile used to elute the adsorbent cartridge was placed in a vial with 0.1 mL of 1-benzo-3-oxo-piperazine at 250 mg l^{-1} as silylation internal standard. The obtained solution was then spiked with 60 μL of bis(trimethylsilyl)trifluoroacetamide (BSTFA) containing 1% trimethylchlorosilane. The vial was placed in a heater at 60°C for 2 hours before being analysed in GC-MS.

GC–MS

Sample solutions were injected under splitless conditions into the injector port of an Agilent 6850 gas chromatograph connected to an Agilent 5975 quadrupole mass spectrometer. Analytes were separated by a DB-5HT (Agilent Technology) fused-silica capillary column (stationary phase poly

(5% diphenyl/ 95% dimethyl) siloxane, 30 m, 0.25 mm i.d., 0.25 μm film thickness) using helium as carrier gas (at constant pressure, 33 cm s^{-1} linear velocity at 200 °C). The underivatised solutions were separated with the following temperature programs: from 50 °C to 300 °C (held 5 min) at 5°C min-1, with GC injector port maintained at 260°C. The silylated solutions were separated with the following temperature programs: from 100 °C (held 5 min) to 310 °C at 5°C min-1, with GC injection port maintained at 280 °C. GC-MS interface and quadrupole were maintained at 280 and 250 °C, respectively for all the analysis. Mass spectra were recorded in the full scan acquisition mode under electron ionisation (70 eV) at 1 scan s^{-1} in the 35–650 m/z range.

DTA-TGA analysis

DTA-TGA were carried out by using a Polymer Thermal Science STA 1500 instrument. The weights of the samples were in the range of 5-10 mg. Heating was performed in a platinum crucible under a nitrogen flow (100 cm^3 min^{-1}) at a rate of 10 °C min^{-1} up to 700 °C

FT/IR analysis

Fourier transform infrared (FT-IR) spectra were recorded on a Thermo Nicolet 380 FT-IR spectrometer. Each powdered sample (~ 1 mg) was mixed with about 100 mg of anhydrous KBr. The mixtures were pressed into 7 mm diameter discs. Pure KBr discs were used as background. The infrared spectra were registered from 4000 to 400 cm^{-1} at 4 cm^{-1} resolution. Fourier self-deconvolution and second derivative resolution enhancement were applied to narrow the widths of infrared bands and increase the separation of the overlapping components. The resolution enhancement resulting from self-deconvolution and the second derivative is such that the number and position of the component bands to be fitted are determined. The curve-fitting was carried out employing BRUKER OPUS peak software (version 4.0) The number of bands was entered into the program along with their respective positions and half-heights. The program iterates the curve-fitting process to achieve the best Gaussian-shaped curves that fit the protein spectrum. A best fit is determined by the root mean square (rms) of differences between the original protein spectrum and the sum of all individual resolved bands. The assignment of component bands in amide I has been done according to the literature data. The percentages of each secondary structure were calculated from the integrated areas of the component bands.

5.2.3 Results

FTIR analysis

The secondary structure of the adducts surface were investigated in the amide I (1700-1600 cm^{-1}) region. Fourier self-deconvolution and secondary derivative were applied to estimate number, position and width of the component bands. Fourier self deconvolution of BSA before adsorption is compared with that of stoichiometric chrysotile and Fe-chrysotile after interaction with BSA. An evident BSA structural modification in amide I region can be easily appreciated after adsorption on inorganic phase surface (figure 5.2.4). From the second derivative of the bands the actual half-width can be estimated, based on which a curve-fitting process was iterated to achieve the best fitted curves. The component bands were assigned on the basis of the literature data [41]. From the integrated areas of the component bands, the percentages of each secondary structure for BSA as such and adsorbed on synthetic nanofibers, were assigned. The protein adhesion on inorganic surface lead to a significant reduction in β-sheet as a function of the increasing Fe amounts in synthetic chrysotile, while random coil and expecially β-turns increase significantly (table 5.2.5). Since β-turns are the most flexible structure composed of hydrophilic amino acids, they could be considered the most efficient means for the surface interaction.

Thermogravimetric analysis of BSA and BSA-(Fe) Chrysotile nanofiber adducts

The thermogravimetric results of BSA are presented in figure 5.2.6. The data show a four-step thermal degradation characterized by a high weight loss (~ 69%) due to the protein degradation process. In figure 5.2.5 are reported the thermogramm of BSA-stoichiometric chrysotile adduct with that of BSA- 0.52 wt% Fe chrysotile and BSA - 1.78 wt% Fe chrysotile adducts. TGA analysis showed that the amount of albumin coated on synthetic nanofibers was higher in the case of stoichiometric synthetic chrysotile. The amounts of adsorbed protein on chrysotile samples surface decreased with increasing iron amounts, while the thermal stability of the protein adsorbed on the chrysotile surface increased with increasing Fe amounts, showing a different reactivity in function of Fe chrysotile contents.

BSA off-line pyrolysis

figure 5.2.1 shows the GC-MS trace of pure protein pyrolysate with numbered peaks referred to table 5.2.1. Structural assignments of DKPs and lateral chain fragmentation products are also reported, together with retention times and mass spectra, while in the last column are indicated the amino acids or the specific sequence from which the listed products are likely to be formed in pyrolysis. The compounds listed in table 5.2.1 and 5.2.2 were detected and quantified in each pyrolysate,

including BSA / synthetic chrysotile adducts. The first elution region in all the chromatograms was featured by the elution of aromatic, mainly phenolic and nitrogenated compounds associated to thermal degradation of amino acids side chains. At higher times the GC traces were occupied by peaks associated to DKPs, deriving from cyclisation reactions. Since the peaks shape of relatively polar DKPs was broad, a silylation procedure was performed. As an example, the GC-trace of silylated BSA pyrolysate is reported in figure 5.2.2. Numbered peaks are listed in table 5.2.2, together with structural assignments, retention times and mass spectra. Since the DKPs are originated in pyrolysis from adjacent amino acids, in table 5.2.3 are indicated the number of the amino acidic sequences present in BSA from which the respective DKPs are likely to be formed. The first elution region of the silylated GC-trace is featured by the elution of DKPs and of thermal degradation products of amino acids, mainly tryptophan and phenilalanine, side chains. At higher times the GC traces were occupied by peaks associated to glutamic acid, tyrosine and pyrimidine silylated derivatives. The DKP yields obtained from two replicate pyrolysis of standard BSA are summarized in table 5.2.4 together with the calculated relative standard deviation (RSD).

BSA/ synthetic chrysotile adducts off-line pyrolysis

figure 5.2.6 shows a typical GC-MS trace of the pyrolysate obtained from pure BSA and synthetic chrysotile adducts (0% iron) while in figure 5.2.7 is reported the silylated GC-MS trace obtained from the pyrolysis of BSA adsorbed on chrysotile Fe-doped at 1.78%. Numbered peaks assignments are reported in table 5.2.1 and 5.2.2 respectively. GC-MS analyses of both underivatized and silylated pyrolysates obtained from BSA/nanofiber adducts were featured mainly by the same compounds detected in BSA pyrolysis. The histogram reported in figure 5.2.8 summarisesw the yield values obtained from the quantitative analysis regarding DKPs detected in underivatized and silylated pyrolysates, obtained from all the tested samples, together with that detected for pure BSA (mean value of n=2). In figure 5.2.8 and figure 5.2.9 the yields of lateral chain thermal degradation products detected in the underivatized and the silylated pyrolysates are reported respectively.

5.2.4 Discussion

DKPs

The most abundant DKP evolved from the pyrolysis of all the samples resulted to be the cyclic dipeptide Pro-Leu (table 5.2.4 and figure 5.2.8), which is also the most abundant pyrolysis product of pure BSA. Although Phe-Leu and Pro-Leu are present in the protein sequence with the same number of linked pairs (see table 5.2.3), the corresponding DKP yields are very different (PL = 2.7% , FL = 0.01% for pure BSA, mean of n= 2, see table 5.2.4). This difference was recorded for all the

analyzed samples and is likely to be due to the different thermal stability of the corresponding lateral chains of the two amino acids and then, to the different thermal stability of the corresponding DKPs [70]. In addition, even if Pro-Lys and Pro-Glu sequences are listed among the most abundant sequences inside BSA, the corresponding DKP yields are considerably lower than that of Pro-Leu. This may be due to two reasons: first, the lateral chain of the two polar amino acid are more instable than that of Leu at the pyrolysis temperature (500°C) and so are the relative DKPs; second, the Pro-Xxx sequences , which are the most abundant (5 on 7 for Pro-Glu, 6 on 10 for Pro-Lys and 2 on 6 for Pro-Leu), are less prone to give DKPs compared to Xxx-Pro sequences [70]. The highest yields of DKPs detected in the underivatized pyrolysates were obtained from the pyrolysis of pure BSA and by BSA/stoichiometric chrysotile adducts, followed by samples at 1.78% and 0.52% of iron content (see figure 5.2.8). The latter sample gave the lowest DKP pyrolysis yields for all the proline containing DKPs, with the exceptions of cyclo(Pro-Ala) and cyclo(Pro-Gly), while showing the highest yields for almost all the cyclic dipeptides containing alanine and glycine, which were detected in the silylated solution. In addition, all the yield values calculated for this sample were found to be anomalous respect to the other BSA/chrysotile samples. For instance, cyclo(Pro-Ile) pyrolysis yields of the two samples at 0% and 1.78% iron content are higher respect to that found for the pure protein, while the sample at 0.52% iron content gave the lowest yield. Instead, in the case of cyclo(Pro-Leu) whose yields values diminished from BSA to BSA/chrysotile adducts, sample 0.52% gave again the lowest yield, emphasizing the decreasing trend. Generally speaking, all the BSA/chrysotile samples gave higher yields of Alanine and Glycine containing DKPs respect to pure BSA, even if cyclo(Gly-Gly) was detected only in the pure protein pyrolysate. However, it worth to notice that, excluding the adduct sample at 0.52% of iron content, DKPs relative abundances do not change between BSA and the other samples indicating that the presence of chrysotile alone does not seem to affect the mechanism involved in the formation of these pyrolysis products.

Lateral chains thermal degradation products

Pyroglutamic acid was found to be the most abundant products evolved from the pyrolysis of all the BSA/chrysotile samples (figure 5.2.10). More in detail, the highest yield of this compound was obtained from the BSA/chrysotile sample at 0.52% iron content, followed in decreasing order by 1.78% , 0% and pure BSA. The pyrolytic yield pattern recorded for pyroglutamic acid was also found for other pyrolysis products (figure 5.2.9, compounds # 19 and 25 in table 5.2.1, and figure 5.2.10, compounds # 4, 5, 15, 17, 19, 21 and 27 in table 5.2.2) which are reported in the previous literature as typical pyrolysis products of specific amino acid such as alanine, phenilalanine,

tryptophane and hydroxyl amino acids [57, 148]. More in general, the BSA/chrysotile adducts pyrolysis gave higher yield values for all the lateral chain degradation products detected both in the silylated and underivatized pyrolysates. An increased production of these products was observed, especially for compounds from number #1 to # 8 reported in table 5.2.1 which are reported in the literature as being produced upon pyrolysis of tyrosine, tryptophan, phenilalanine and alanine [57, 148]. However, in this case a different pattern from that noted for Pyroglutamic acid was detected, as both BSA/chrysotile adducts at 0.52 and 1.78% of iron content gave higher yields respect to BSA, but lower respect to BSA/stoichiometric chrysotile sample.

5.2.5 Conclusions

Pyrolysis coupled to GC-MS was used for the first time to study surface interactions and structural modifications of proteins adsorbed onto a mineral phase. BSA/chrysotile adducts doped with different amounts of iron were pyrolysed to obtain information about surface interactions in the presence of metallic ions. A quantitative method for DKPs and other compounds produced upon pure BSA pyrolysis was developed and applied to the protein/chrysotile adducts. The surface interaction between BSA and chrysotile was found to affect protein pyrolysis. Proline containing DKPs detected in the GC-MS traces of the underivatized sample pyrolysates were found to have rather similar relative abundances. On the other hand, DKPs detected in the silylated GC-MS pyrolysates and compounds evolved from the thermal degradation of amino acids lateral chains, were found to be produced in different yields from the various samples. These compounds came mainly from alanine, phenylalanine, tryptophane and hydroxyl amino acids pyrolysis, which were probably the most involved in the interaction between BSA and chrysotile. Quantitative results obtained from pyrolysis showed that BSA / chrysotile at 0.52% of iron content has a different behaviour respect to adducts at 0% and 1.78% of iron content. Pyrolysis results are supported by FTIR analysis showing an increase in the disordered structure larger for the adducts at 0.52% of Fe. Then FTIR and Py/GC-MS results suggest that there is not a linear correlation between the concentration of iron in the nanofiber and the degree of interaction with BSA, but rather the occurrence of a threshold effect at low iron amount in the chrysotile nanofibers. Since the Fe^{+2} ions arrangement in the tetrahedral and octahedral layers of the chrysotile crystalline structure depends on the doping percentage of this element in nanofibers, as this determines the iron placement upon nanofibers surface [136, 142], the achieved results can be reasonably attributed to different surface interactions between BSA molecules and the nanofiber. TGA results showed a direct correlation between the iron doping percentage of nanofibers and the amount of adsorbed BSA, which decrease with increasing iron content. On the other hand, the strength of BSA/chrysotile surface interaction seems to increase with increasing iron content.

Table 5.2.1 Principl pyrolysis products detected in sample pyrolysates. Numbers are referred to peaks in figure 5.2.1.

n°	Compound	RT	Mass spectra		References
1	phenol	9.45	**66**, *94*	**Tyr**	[57]
2	methyl phenol	11.27	77, 79, **107**, *108*	**Tyr**	[57]
3	benzilnitrile	12.40	90, 99, 116, ***117***	**Phe**	[57]
4	dihydrazide derivative	12.84	41, 55, 98, **125**	**-**	-
5	benzen-propannitrile	14.02	**91**, 92, *131*	**Phe**	[57]
6	2-methyl-6-propilimmine	14.36	95, **107**, 120, *148*	**-**	-
7	piperidine	14.74	62, 82, ***98***	**Ala**	[148]
8	indole	14.83	89, 90, **91**, *117*	**Trp**	[57]
9	acetamide, N-(2,4-dihy...	15.69	55, **125**, 136, *167*	**-**	-
10	phenol, 5-methoxy-2-methyl	15.87	110, **125**, 136, *167*	**Tyr**	[183]
11	methyl indole	16.18	77, 96, **130,** *131*	**Trp**	[148]
12	pyrimido-pyrimidine	16.26	68, **111,** *138*	**Ala**	-
13	isopropilidene	16.43	81, 99, **139**, *152*	**-**	-
14	tetramethyl-pyrimidone	16.91	96, 100, **152,** *166*	**-**	-
15	pirrolizine	17.54	84, 97, **140,** *167*	**His**	[57]
16	dibenzyl	18.30	**91**, *182*		-
17	isoquinoline-1-ethyl	18.99	129, 132, **156**, *157*	**Trp**	[148]
18	unknown (?)	19.38	95, 138, **152**, 179	**-**	-
19	pyrimidinedione derivative	19.39	98, **140,** 153, *170*	**Ala**	[148]
20	imidazole derivative	19.74	123, 138, **151,** *166*	**Trp**	[148]
21	quinoline 8-ethyl	20.93	128, 129, 154, ***156***	**Trp**	[148]
22	unknown	21.07	98, 129, **156**, 199	**-**	-
23	diketodipyrrole	21.59	65, 93, 130, ***186***	**Pro-Pro**	[96]
24	cyclo Pro-Ala 1	21.64	**70**, 97, 125, *168*	**Pro-Ala**	[88]
25	pyrazine derivative	21.38	123, **138**, 151, *165*	**hydroxy-amino acids**	[148]
26	cyclo Pro-Ala 2	22.08	**70**, 97, 125, *168*	**Pro-Ala**	[88]
27	cyclo Pro-Gly	22.46	83, 98, **111**, *154*	**Pro-Gly**	[88]
28	cyclo Gly-Leu	22.60	56, 85, 99, **114**, 127,*(170)*	**Gly-Leu**	[88]
29	cyclo Pro-Val 1	23.49	**70**, 72, 125, **154**, *(196)*	**Pro-Val**	[88]
30	12-aminolauric acid	23.68	91, 113, **156,** *196*	**-**	-
31	cyclo Pro-Val2	23.96	**70**, 72, 125, **154**, *(196)*	**Pro-Val**	[88]
32	cyclo Leu-Leu1	25.42	86, 98, 113, **170**, *226*	**Leu-Leu**	[182]
33	cyclo Leu-Leu2	25.54	86, 98, 113, **170**, *226*	**Leu-Leu**	[182]
34	cyclo Pro-Pro	25.72	**70**, 96, 138, 166, ***194***	**Pro-Pro**	[88]
35	cyclo Pro-Ile1	25.22	70, 86, 125,**154,** (*210*)	**Pro-Ile**	[182]
36	cyclo Pro-Ile2	25.39	70, 86, 125,**154,** (*210*)	**Pro-Ile**	[182]
37	cyclo Pro-Leu1	25.57	**70**, 86, 125, 154,(*210*)	**Pro-Leu**	[88]
38	cyclo Pro-Leu2	25.76	**70**, 86, 125, 54,(*210*)	**Pro-Leu**	[88]
39	cyclo Pro-Lys (1)	26.50	70, 125, **154**, 166, *208*	**Pro-Lys**	[182]
40	unknown	26.93	**91**, 97, 230	**-**	-
41	cyclo Pro-PyroGlu	27.09	70, 96, 124, 152, 180, ***208***	**Pro-Glu**	[182]
42	cyclo Pro-Lys (2)	27.29	70, 125, **154**, 166, *208*	**Pro-Lys**	[182]

43	unknown (?)	28.08	104, 150, **195**	-	-
44	unknowm (?)	28.68	89, **117**, 200	-	-
45	cyclo Pro-Lys (3)	28.76	70, 84, 152, 180, ***208***	**Pro-Lys**	[182]
46	cyclo Phe-Ala 1	28.97	44, **91,** 127,*218*	**Phe-Ala**	[89]
47	pyrazole-4-carboxaldehyde	28.97	228	**His**	[183]
48	cyclo Phe-Ala 2	29.50	44, **91,** 127,*218*	**Phe-Ala**	[89]
49	cyclo Pro-Met 1	30.88	70, 139, **154**, 167, *228*	**Pro-Met**	[88]
50	cyclo Pro-Met 2	31.14	70, 139, **154**, 167, *228*	**Pro-Met**	[88]
51	cyclo Val-Phe 1	30.71	**91,** 113, 127, 155, *246*	**Val-Phe**	[75]
52	cyclo Val-Phe 2	31.33	**91,** 113, 127, 155, *246*	**Val-Phe**	[75]
53	cyclo Phe-Leu 2	32.38	**91,** 113, 141, 204, *260*	**Phe-Leu**	[75]
54	cyclo Phe-Leu 1	32.76	**91,** 113, 141, 204, *260*	**Phe-Leu**	[75]
55	cyclo Pro-Phe 1	32.50	70, 91, **125**, 153, *244*	**Pro-Phe**	[76]
56	cyclo Pro-Phe 2	33.28	70, 91, **125**, 153, *244*	**Pro-Phe**	[76]

Table 5.2.2 Principl pyrolysis products detected in samples silylated pyrolysates. Numbers are referred to peaks in figure 5.2.2.

n°	**Compound**	**R.T**	**Mass spectra**		**References**
1	cyclo(Ala-Ala) 1 di-TMS	11.04	156, 171, 255, **271**, *286*	Ala-Ala	[182]
2	cyclo(Ala-Ala) 2 di-TMS	11.42	156, 171, 255, **271**, *286*	Ala-Ala	[182]
3	cyclo(Gly-Ala) di-TMS	12.31	129, 142, 241, **257**, *272*	Gly-Ala	[182]
4	parabanic acid TMS	12.74	73, 100, 147, **243**, *258*	Glu	-
5	1H-indole, 1-(trimethylsilyl)	13.52	73, 79, 174, ***189***	Trp	-
6	cyclo(Ala-Val) 1 di-TMS	13.80	156, 197, 257, **299**, *314*	Ala-Val	[182]
7	cyclo(Ala-Val) 2 di-TMS	14.26	156, 197, 257, **299**, *314*	Ala-Val	[182]
8	cyclo(Gly-Gly) di-TMS	14.37	73, 100, 147, **243**, *258*	Gly-Gly	[182]
9	cyclo(Gly-Val) TMS	14.9	142, 170, 257, **285**, *300*	Gly-Val	[182]
10	cyclo(Ala-Leu) 1 di-TMS	15.15	156, 170, 297, ***313***	Ala-Leu	[182]
11	cyclo(Ala-Leu) 2 di-TMS	15.27	156, 170, 297, ***313***	Ala-Leu	[182]
12	acetonitrile, 2-phenyl N-TMS	15.44	73, 105, 116, **190**, *205*	Phe	-
13	2-piperidinecarboxylic acid O-TMS	15.78	73, 147, **156**, 258, *273*	Ala	-
14	cyclo(Gly-Leu) di-TMS	16.38	156, **257**, 271, 299, *314*	Gly-Leu	[89]
15	piperidine	16.84	73, 100, 142, **244**, *285*	Ala	-
16	unknown (?)	17.24	73, 171, **225**, 254, 269	-	-
17	pyroglutamic acid	17.72	73, 147, **156**, 258 (*273*)	Glu	-
18	pyrazine derivative	19.12	**73**, 188, 229, 329 (?)	-	-
19	benzen-amine derivative	19.66	73, 195, **210**, 251	Phe	-
20	α-D-glucopyranoside derivative	20.28	73, 147, 204, **217**, 333	-	-
21	pyrimidine derivative	24.50	73, 147, **243**, 319, 334	-	-
22	indole derivative	24.66	73, 247, **321**, *336*	Trp	-
23	tyrosine derivative	24.75	73, 147, 179, 294, **309**	Tyr	-
24	phenyl phosphonic acid TMS	25.48	73, 211, **287**, *302*	Phe or Tyr ?	-
25	unknown (?)	27.07	73, 91, 152, **267**	-	-
26	pyrimidine derivative	27.98	73, 147, 165, 253, 268, 359	Ala	-
27	octadecanoic acid TMS	30.219	73, **117**, 145, 341, *356*	-	-

Table 5.2.3 Number of linked pairs of amino acids in bovine serum albumin responsible of DKPs formation upon protein pyrolysis.

Amino acid sequences	N°
Pro-Leu	*6*
Pro-Val	*3*
Leu-Leu	*8*
Pro-Ala	*1*
Gly-Leu	*5*
Pro-Ile	*1*
Pro-Gly	*1*
Pro-Pro	*1*
Pro-Lys	*10*
Pro-Met	*1*
Pro-Phe	*2*
Val-Phe	*6*
Phe-Ala	*7*
Pro-Glu	*7*
Phe-Leu	*6*

Table 5.2.4 DKPs yields detected in pure Bovine serume albumin (BSA) pyrolysates (n=2). Yields are expressed as Wg_{DKP}/Wg_{BSA} * 100

Analytes ↓ / Sample →	**BSA 1**	**BSA 2**	**MEAN**	**RSD**
diketodipyrrole	0.14	0.15	0.14	5
cyclo(Pro-Ala)	0.23	0.22	0.22	3
cyclo(Pro-Gly)	0.09	0.12	0.10	20
cyclo(Gly-Leu)	0.12	0.13	0.12	6
cyclo(Pro-Val)	0.57	0.69	0.63	13
cyclo(Leu-Leu)	0.17	0.3	0.23	39
cyclo(Pro-Pro)	0.07	0.09	0.08	18
cyclo(Pro-Ile)	0.17	0.18	0.17	4
cyclo(Pro-Leu)	2.5	2.9	2.7	10
cyclo(Phe-Ala)	0.04	0.04	0.04	5
cyclo(Pro-Met)	0.04	0.08	0.06	47
cyclo(Val-Phe)	0.02	0.03	0.02	28
cyclo(Phe-Leu)	0.01	0.02	0.01	47
cyclo(Pro-Phe)	0.04	0.04	0.04	5
cyclo(Pro-Lys)	0.003	0.003	0.003	7
cyclo(Pro-PyroGlu)	0.08	0.09	0.085	8
cyclo(Ala-Ala)*	0.03	0.02	0.025	28
cyclo(Gly-Ala)*	0.04	0.05	0.045	16
cyclo(Gly-Gly)*	0.03	0.04	0.035	20
cyclo(Ala-Val)*	0.05	0.04	0.045	16
cyclo(Gly-Val)*	0.02	0.01	0.015	47
cyclo(Ala-Leu)*	0.01	0.02	0.015	46
cyclo(Gly-Leu)*	0.06	0.07	0.065	11
TOTAL	**4.56**	**5.35**	**4.96**	**11**

Table 5.2.5 Fourier self-deconvolution and secondary derivative of FTIR peaks in figure5.2.3. Values were reported as secondary structure percentage detected in samples.

Sample	α-Helix (%)	β-Sheet (%)	Random (%)	β-Turn (%)	
BSA lyophilized powder	38±2	44±1	3±1	15±1	
Stoichiometric BSA-Chrysotile adducts	37±2	11±1	4±1	48±2	37±2
BSA-Fe (0.52 wt %) Chrysotile adducts	18±2	7±2	17±3	58±2	18±2
BSA-Fe (1.87 wt %) Chrysotile adducts	31±2	4±1	14±3	51±2	

Figure 5.2.1. GC-MS trace (total ion) of the solution obtained after off-line pyrolysis at 500 °C of BSA. Peak numbers correspond to compounds listed in tables 5.2.1.

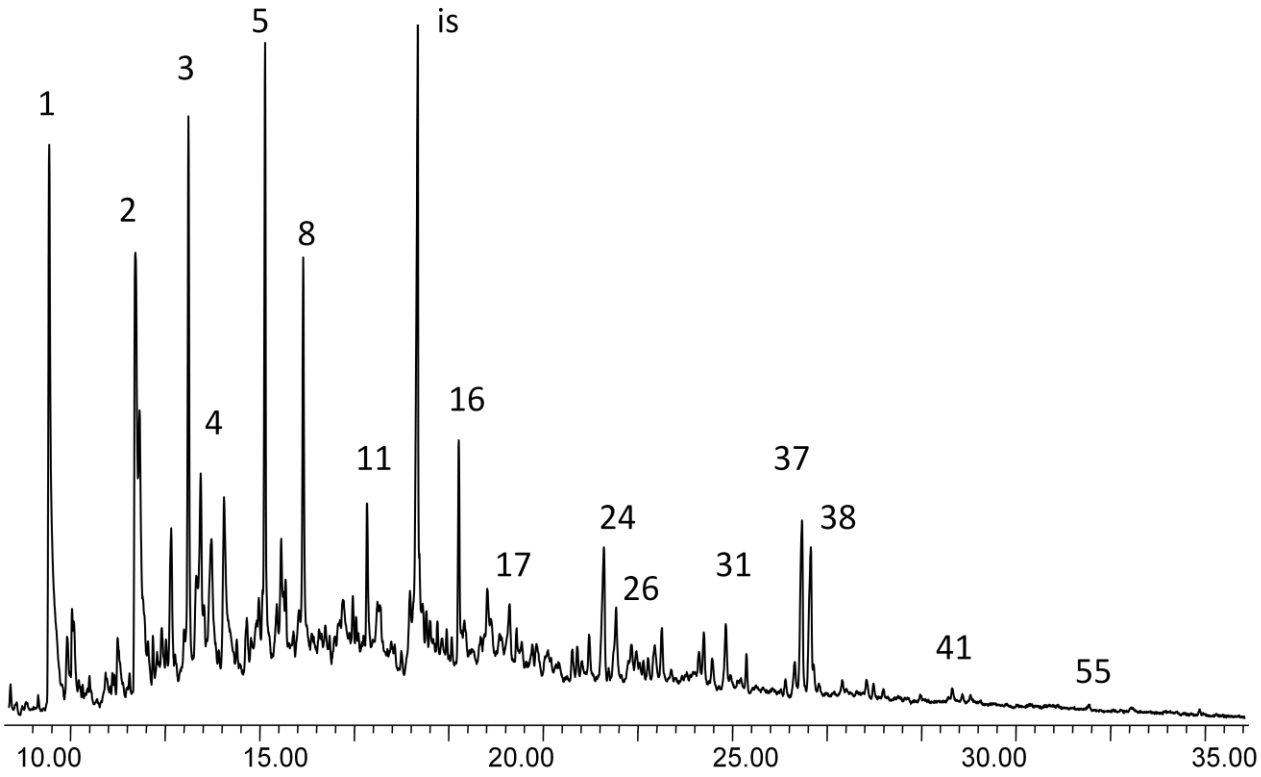

Figue 5.2.2 GC-MS trace (total ion) of the silylated solution obtained after off-line pyrolysis at 500 °C of BSA. Peak numbers correspond to compounds listed in tables 5.2.2.

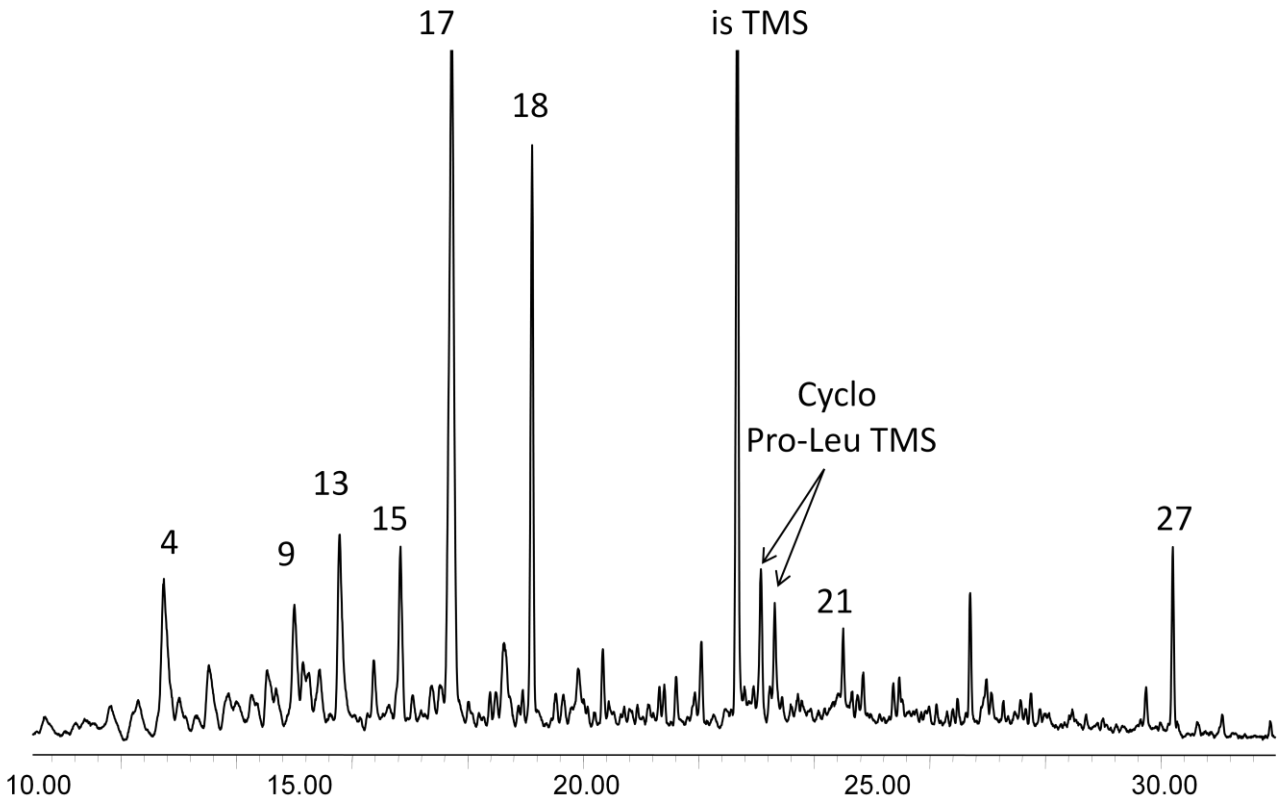

Figure 5.2.3 FTIR analysis of BSA (a), BSA chrysotile adducts at 0% (b), 0.52% (c) and 1.78% (d) of iron content.

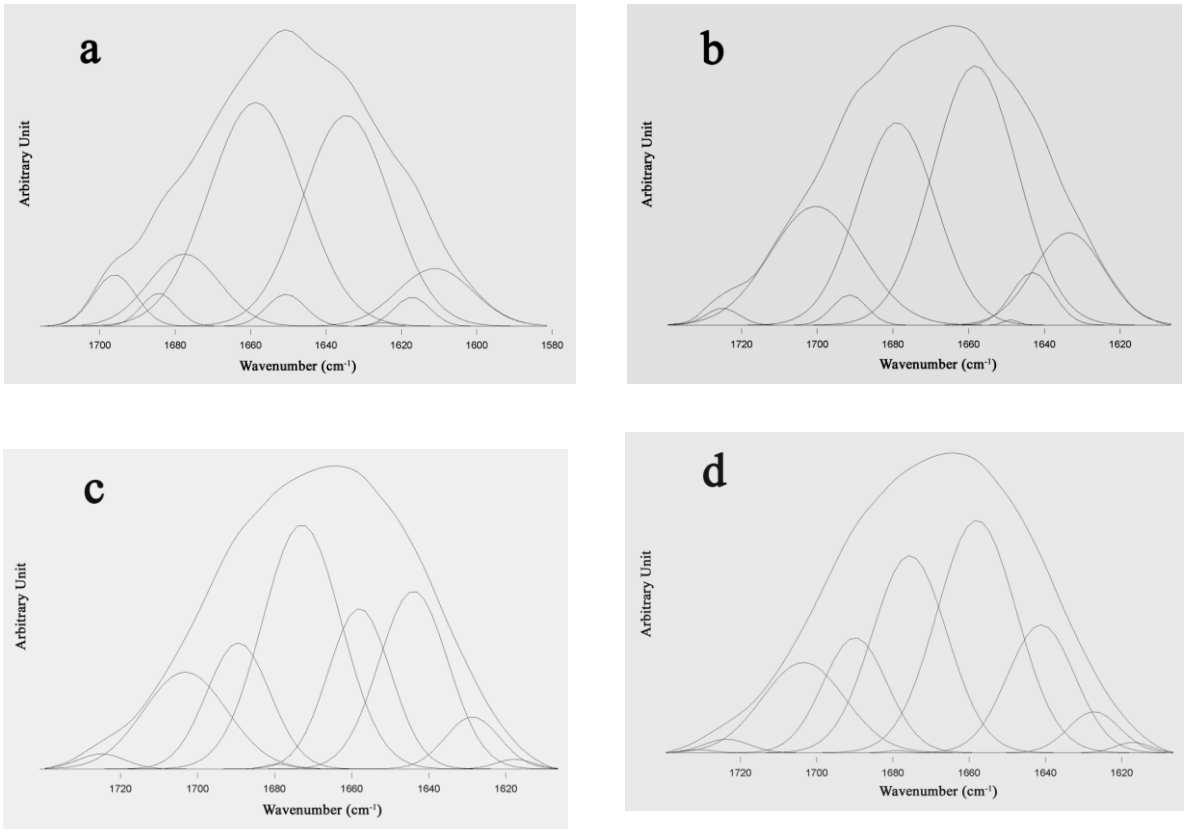

Figure 5.2.4 TGA analysis of bovine serum albumin/chrysotile adducts at different iron percentages.

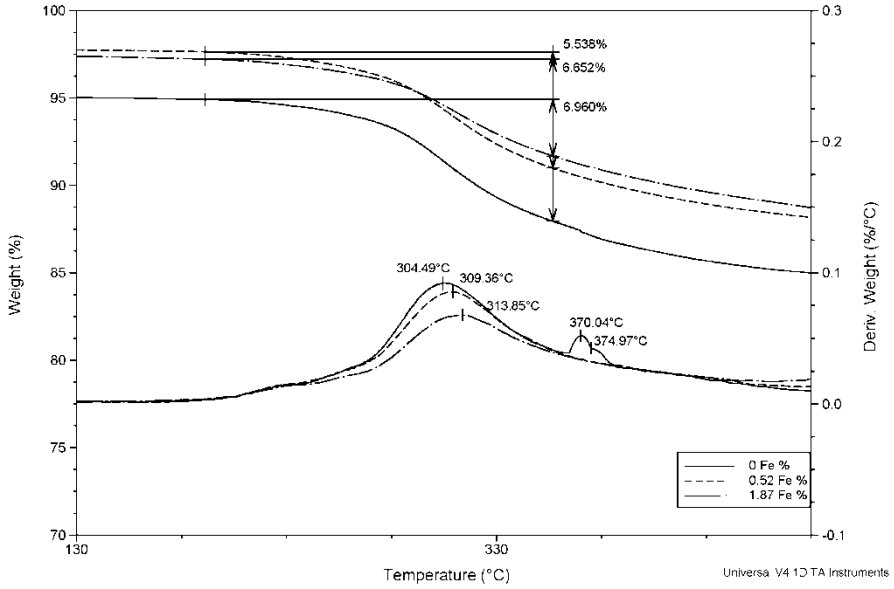

Figure 5.2.5 TGA analysis of pure bovine serum albumin (BSA).

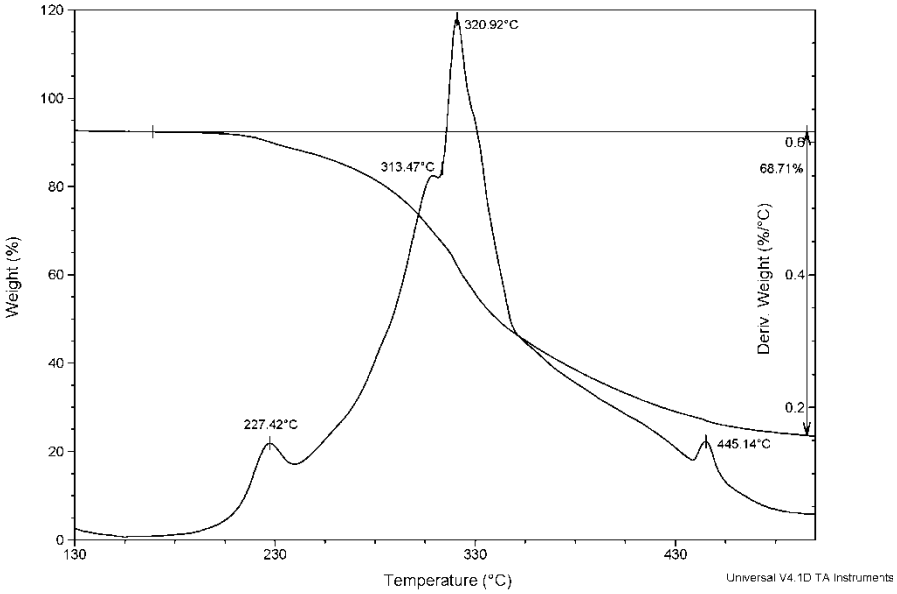

Figure 5.2.6 GC-MS trace (total ion) of the silylated solution obtained after off-line pyrolysis at 500 °C of nanofibers doped with iron at 1.78% and BSA adduct. Peak numbers correspond to compounds listed in tables 5.2.1.

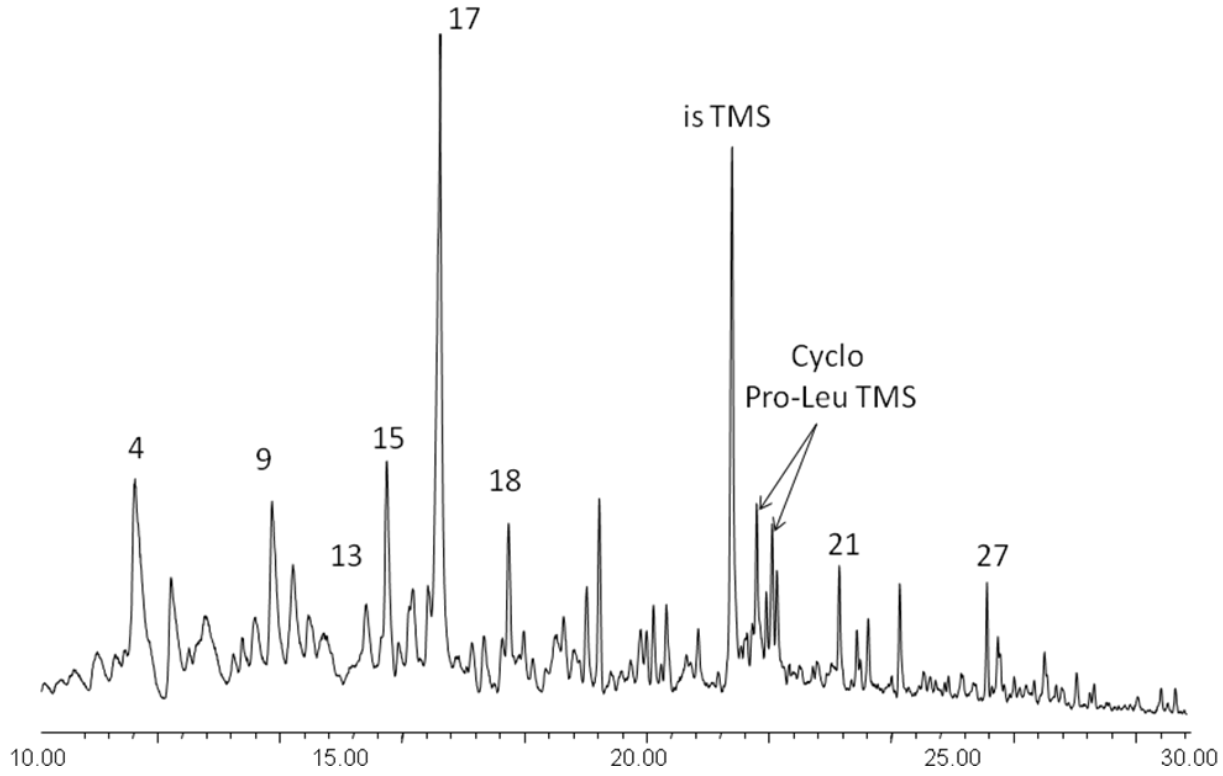

Figure 5.2.7 GC-MS trace (total ion) of the silylated solution obtained after off-line pyrolysis at 500 °C of nanofibers doped with iron at 1.78% and BSA adduct. Peak numbers correspond to compounds listed in tables 5.2.2.

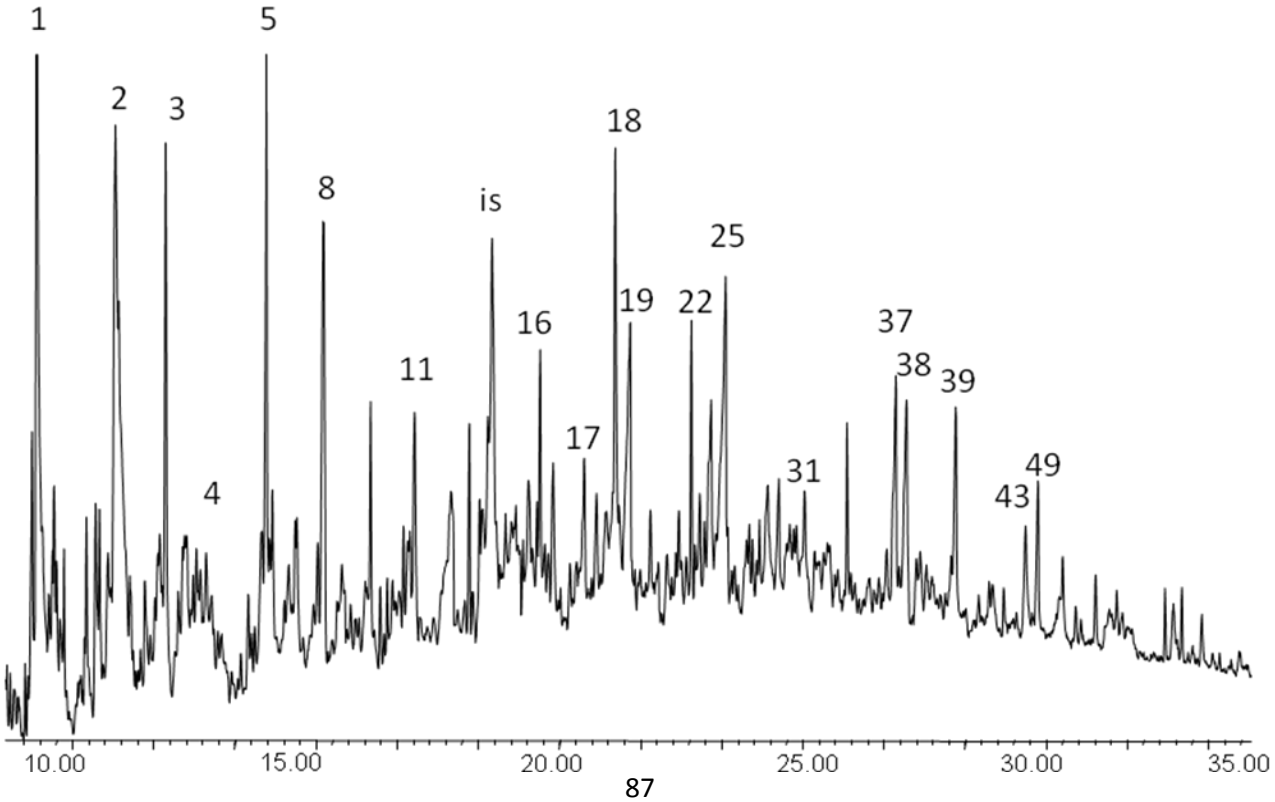

Figure 5.2.8 DKPs yields in pure and silylated pyrolysates. Data are expressed as $Wg_{DKP} / Wg_{ads.\ BSA}$*100. DKPs detected in the silylated form are marked by an asterisk (*).

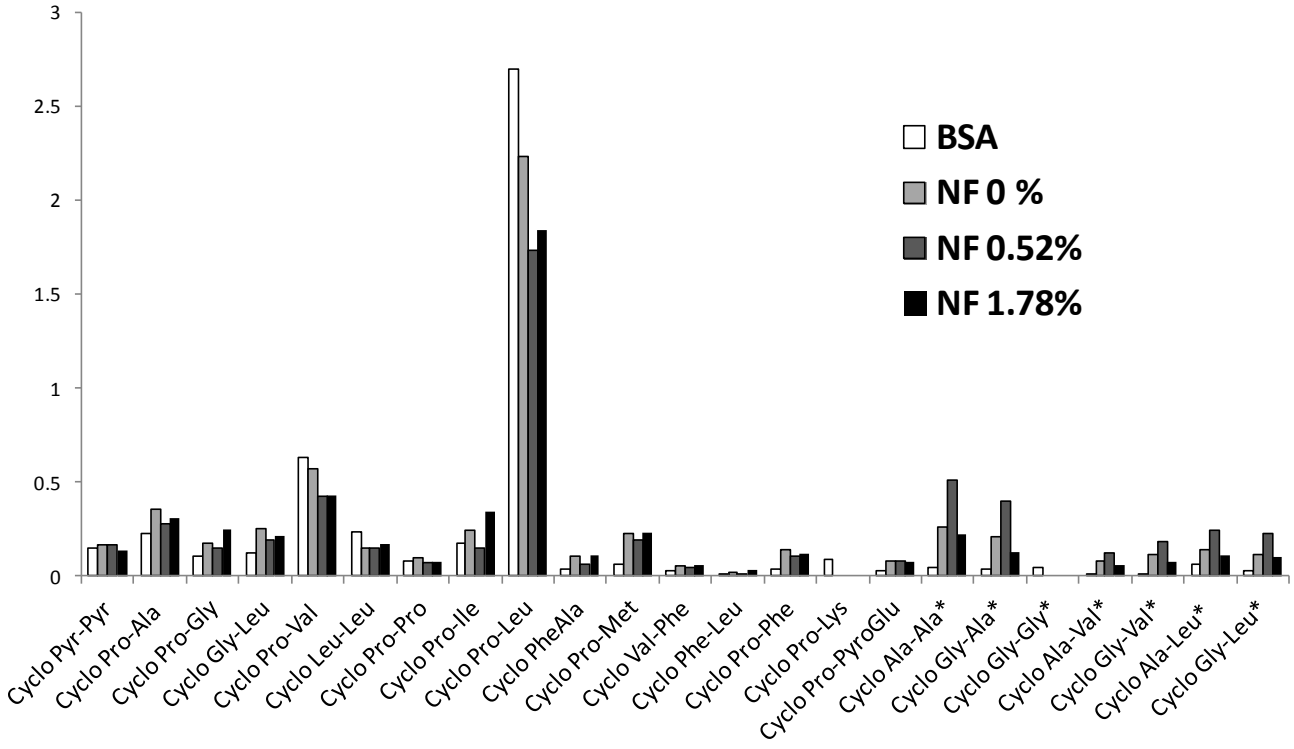

Figure 5.2.9. Lateral chain fragmentation products yields in pure pyrolysates. Data are expressed as $Wg_{DKP} / Wg_{ads.\ BSA}$*100

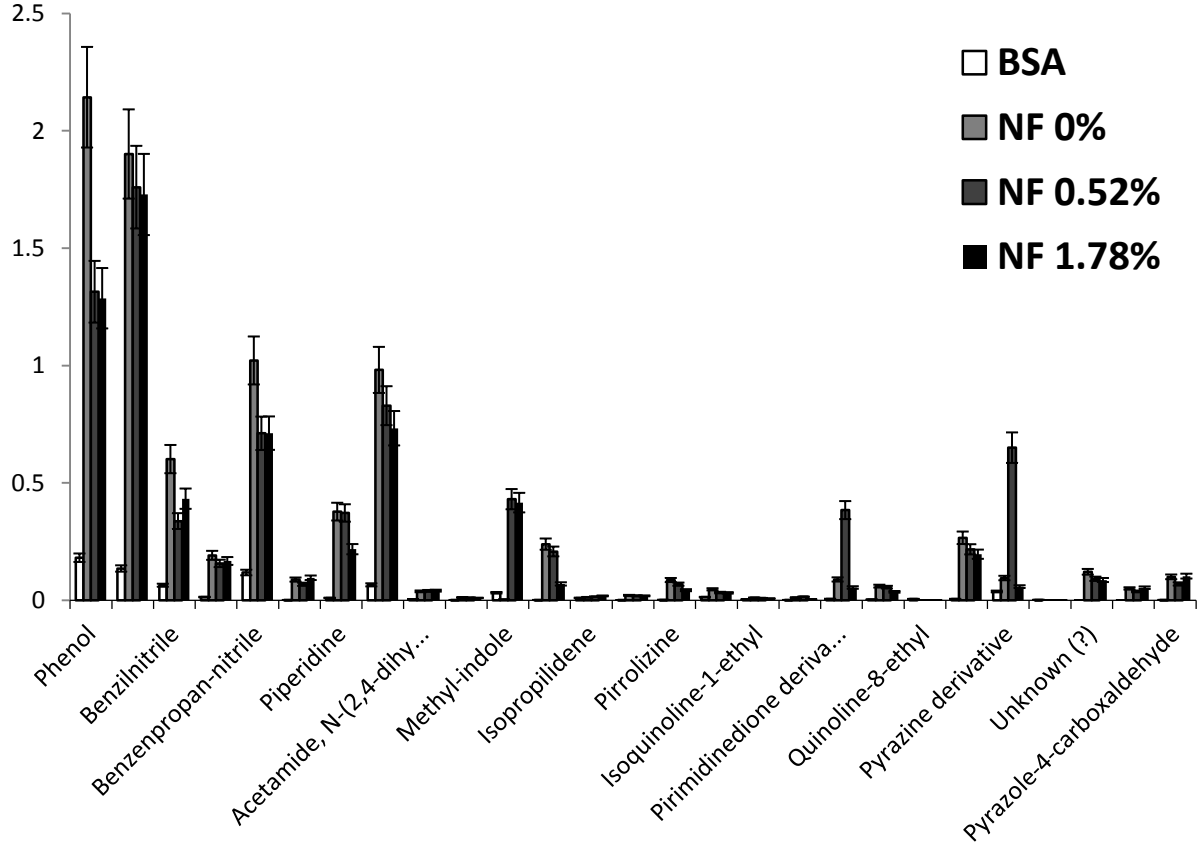

Figure 5.2.10 Lateral chain fragmentation products yields in silylated pyrolysates. Data are expressed as $Wg_{DKP} / Wg_{ads.\ BSA} * 100$

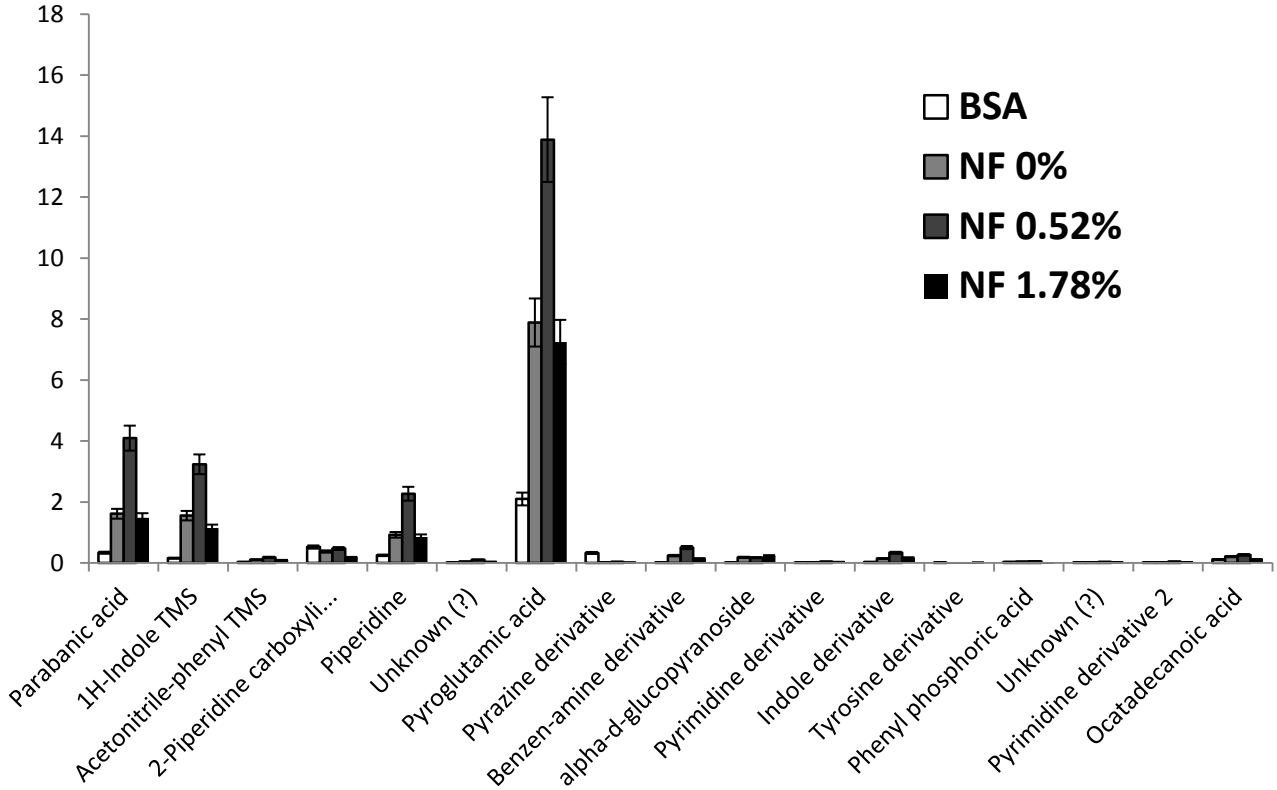

5.3 Pyrolysis of archaeological bones from Vicenne Necropolis – Molise (Italy)

5.3.1 Introduction

Collagen triplex molecule is a heteropolymer consisting of two a1 chains and an a2 chain in which each collagen polypeptidic chain contains a helical domain and non-helical N and C terminal domains (telopeptides). The non-helical regions can be compared with flexible arms, which bear the functional groups for the intermolecular bonds. The triple helical region on one hand controls the formation and stabilization of the triple helix and, on the other hand, is responsible for the self-assembly of the molecules to fibrillar structures with a characteristic pattern. These are rigidly held by strong hydrogen bond interactions between the hydroxyl group of hydroxyproline and the amino function of adjacent glycine residues effectively forming a rod-like crystalline phase [149]. Ultrastructural studies of the collagen and hydroxyapatite crystals in bone show that they are intimately associated [150], and for this characteristic collagen peptides are preserved in fossil bones several thousands or millions of years old [151]. Broadly speaking, collagen content in bone declines with time since deposition, and the loss of nitrogen (collagen representing >95% of the nitrogen in bones) has been used as a crude dating tool [152]. Collagen degradation in bone begins already during life [153], with increasing numbers of crosslinks leading to increased brittleness and fragility of the collagen molecule. The absence of an unique trend in collagen degradation during bones burial, emphasizes that other factors have important roles to play [154]. The phase transition from insoluble collagen to resulting soluble gelatine (more biodegradable) due to weathering and microbiological activities that occur on bone organic fraction, has an impact upon the physical properties of bone [155,156] and the survival of bone proteins, but it is retarded by the presence of mineral [158] and close packing of the fibrils [149]. Many studies [158-161] on archaeological bones are focused to elucidate degradation mechanisms of the organic fraction, in relation to the burial environment, or the fossilisation process of the bioapatite. Many others [154,162,163] have as object the investigation of the relation between diet, age at death and bone composition, and the radiocarbon dating. However, fewer studies [164-168] were aimed to establish a connection between collagen degradation and mineral fossilisation, though their intimate structural aggregation is well known. Species, age at death, cultural practices and mode of death will all play a part during diagenesis, with biomolecular deterioration still remains a largely unexplored aspect of bone [164]. The precise structural relationship between collagen molecules and apatite in bone is still debated [163] but the ageing process is understood as affecting either the crystalline collagen filaments or the amorphous matrix, or both, with corresponding changes of the interface phase [169]. Studies reported in the literature [170,171] have showed that the information contained in pyrolysis

fingerprints can be used for the evaluation of chemical and rheological parameters of collagen-rich tissues in a single measurement. Analyses of bone collagen require the destruction of material, so that it is essential to optimize the qualitative and quantitative performances of the extraction procedures used [151]. At this regard analytical pyrolysis, both in on-line and off-line configurations, is undoubtedly a very attractive technique for the ability to perform semi-quantitative (on-line) and quantitative (off-line) analysis on very small amounts of sample. In previous studies [170] Curie point/GC-MS analytical pyrolysis was used to evaluate the content of collagen in lamb meat. Thermogravimetric techniques are reported in the literature as useful tools in the forensic field, on bone samples which have not undergone diagenetic processes, to characterize bone fragments [172] and to examine specimens of different post-mortem age [173]. The mineral deposited in the bone is formed by plate-like nano-crystals of carbonated hydroxylapatite (cHA) having a low degree of crystallinity. A measure of fossilization of cHA in bone is given by the increase its degree of crystallinity, at which is associated a higher carbonation. This measure was carried out by FTIR spectroscopy and X-ray diffraction. The use of FTIR spectra was based on the so-called "splitting factor" to semi-quantitatively estimate relative cHA crystallinity [174]. The evaluation of the degree of crystallinity by X-ray diffraction pattern analysis is based on the peak broadening of the diagnostic reflections of cHA [175]. The increase of crystallinity in cHA requires a ripening process that necessary involves dissolution and re-precipitation steps. It was proposed that this process can start only when the collageneous matrix has reached a threshold level of degradation, so to leave free volume to host water and start ripening processes. Thus, a deep understand of the bone diagenesis requires an accurate study on the correlation between organic matrix, mainly collagen, degradation and cHA fossilization. Since TGA analysis only give information on the organic matter content, pyrolysis was used to elucidate the nature of the organic matrix with qualitative and quantitative analysis in order to determine the presence and the amount of collagen in the archaeological samples. We considered the relations between thermal data of the organic fraction (TGA and Py-GC/MS) on one hand and the spectroscopic and diffractiometric data on the mineral fraction (cHA) degree of crystallinity on the other, to evaluate the conservation state of five archaeological human bone samples from the Vicenne Necropolis (Molise – Italy). Quantitative analysis from archaeological samples was achieved paying particular attention to collagen typical markers such as cyclo (Pro-Hyp) [176]. This compound belong to a class of molecules called diketopiperazine (DKP), which are produced in pyrolysis by dimerisation of two amino acidic moieties linked together in the peptidic chain. The most important among collagen pyrolysis products are the cyclic dipeptides obtained by dimerisation of proline with other amino acid, such as proline itself, hydroxyproline and glycine, which are the most abundant amino acid of collagen sequence [176]. Moreover, cyclo(Pro-Hyp) is a

unique marker of collagen pyrolysis, as hydroxyproline was detected in few proteins other than collagen [177]. The aim was to compare spectroscopic, diffractometric and thermogravimetric data to understand the relations between mineral composition, cHA degree of crystallinity and collagen stretch content in bones subjected to diagenesis.

5.3.2 Materials and methods

Sample preparation

The five archaeological human bone samples (T67, T98, T139, T150, T165) came from Vicenne Necropolis, in Molise (Italy). The soil matrix, in which the complete skeleton were buried and of which the bones were clothed, was removed from the samples by means of a brush with soft bristles and placed in a vial. The samples were dried at 70°C for 2 hours under vacuum and then cleaned again with the brush. The dried samples were minced in a ceramic mortar and the obtained powder placed in a crucible. The specimens were then placed in an heater at 100°C until reaching a constant weight. A piece of bovine bone from a local butcher shop was used for samples comparison. The fresh bone sample was boiled in water for 4 hours. The flash was removed mechanically and the bone was then subjected, with slightly modifications, to the cleaning procedure reported by DePaula et al. [178]. The sample was immerse in a 3% hydrogen peroxide aqueous solution and heated at 70°C for 4 hours. The cleaned bone was finally minced and air dried as already described for the human bone samples. The obtained fresh bone powder was called BB.

Off-line pyrolysis

The apparatus employed for off-line pyrolysis experiments was described in detail elsewhere [147]. Briefly, it consists in a pyrolysis chamber fitted for a pyroprobe model 1000 (CDS Analytical Inc.) equipped with a resistively heated platinum filament. A sample holder quartz tube containing an exactly weighed amount of sample (about 9-12 mg) was introduced into the platinum coil and the probe was in turn inserted into the pyrolysis chamber. The apparatus was fluxed with a nitrogen stream at 200 mL min^{-1} prior to pyrolysis. The exit of the pyrolysis chamber was connected through a Tygon tube to a cartridge for air monitoring containing a XAD-2 resin as adsorbent (orbo-43) purchased from Supelco. In order to collect higher amounts of pyrolysis products, from 3 to 4 pyrolysis were performed with the same cartridge until pyrolysis of 30 - 45 mg for each sample was achieved. The cartridge was then eluted with 5 mL of acetonitrile. The solutions were collected, concentrated under a gentle nitrogen stream and spiked with 0.1 mL of 250 mg l^{-1} of sarcosine anhydride solution in ACN before being analyzed in GC-MS. In the case of archaeological finds, samples were pyrolysed consecutively for 3/4 times and pyrolysis products collectively trapped on

the same cartridge. 8.3 mg of collagen were pyrolysed in order to collect retention times and mass spectra of the major products produced during its thermal degradation. 10-15 mg of bovine bones (BB) were pyrolysed in order to highlight matrix effects, due to the strong interaction between collagen fibrils and hydroxyl-apatite inside bone.

Silylation

An aliquot of the acetonitrile used to elute the adsorbent cartridge was placed in a vial with 0.1 mL of 1-benzo-3-oxo-piperazine at 250 mg l^{-1} as silylation internal standard. The obtained solution was then spiked with 60 μL of bis(trimethylsilyl)trifluoroacetamide (BSTFA) containing 1% trimethylchlorosilane. The vial was placed in a heater at 60°C for 2 hours before being analysed in GC-MS.

GC–MS

Sample solutions were injected under splitless conditions into the injector port of an Agilent 6850 gas chromatograph connected to an Agilent 5975 quadrupole mass spectrometer. Analytes were separated by a DB-5HT (Agilent Technology) fused-silica capillary column (stationary phase poly (5% diphenyl/ 95% dimethyl) siloxane, 30 m, 0.25 mm i.d., 0.25 μm film thickness) using helium as carrier gas (at constant pressure, 33 cm s^{-1} linear velocity at 200 °C). The underivatised solutions were separated with the following temperature programs: from 50 °C to 300 °C (held 5 min) at 5°C min-1, with GC injector port maintained at 260°C. The silylated solutions were separated with the following temperature programs: from 100 °C (held 5 min) to 310 °C at 5°C min-1, with GC injection port maintained at 280 °C. GC-MS interface and quadrupole were maintained at 280 and 250 °C, respectively for all the analysis. Mass spectra were recorded in the full scan acquisition mode under electron ionisation (70 eV) at 1 scan s^{-1} in the 35–650 m/z range.

Quantitative analysis

The quantity of DKPs was calculated from GC peak area integrated in the total ion chromatogram and the peak area of the internal standard (sarcosine anhydride for the underivatised solutions and the persilylatedderivative of 1-oxo-3-benzo-piperazine for the derivatised ones). A single point calibration was performed using cyclo (Gly-Leu) for the underivatised solutions as quantitation standard while for the silylated was used its persilylated derivative. Yields are reported in table 5.3.3 and 5.3.4.

RSD

The relative standard deviations reported in tables 5.3.1 and 5.3.2 were obtained on three replicate pyrolysis respectively on standard collagen, BB and sample T67. This specimen was the only find for which a sufficient amount of sample was available in order to obtain three replicates, while only single pyrolysis was possible for the other archaeological samples

.

Blank analysis

A blank sample of quartz was pyrolysed using the same method as a negative control. In addition, the soil present on the bone samples was collected and pyrolysed in order to detect target analytes produced from other proteinaceous matrices than collagen. The blank analyses did not yield any signal from target analytes.

TGA analyses

Thermogravimetric investigations were carried out on dried samples using a TA instrument. Heating of about 5 mg of sample was performed in flowing nitrogen (100 cm^3 min^{-1}) using a ceramic crucible at a rate of 10 °C min^{-1} up to 900 °C.

FTIR analyses

FTIR spectra of samples in KBr disks were collected at room temperature by using a FTIR Nicolet 380 Thermo Electron Corporation working in the range of wavenumbers 4000–400 cm^{-1} at a resolution of 2 cm^{-1}. A finely ground, approximately 1% (*w*/*w*) mixture of the sample in KBr was pressed into a transparent disk using a hydraulic press and applying a pressure of 48.6 tsi (670.2 MPa). The splitting factor (SF) was calculated according to the method of Weiner and Bar-Yosef (1990) [174]. After a baseline correction between 1200 and 250 cm^{-1}, the intensity of the two $\nu_4(PO_4)^{3-}$ vibration bands at 565 and 605 cm^{-1} in the absorbance mode was measured and their sum was then divided by the intensity of the valley between these absorption bands and the baseline. The SF values have an error of ±0.1.

XRD analysis

X-ray powder diffraction patterns were collected using a PanAnalytical X'Pert Pro equipped with X'Celerator detector powder diffractometer using Cu Kα radiation generated at 40 kV and 40 mA. The diffraction patterns were collected within the 2θ range from 10° to 60° with a step size (Δ2θ) of 0.02° and a counting time of 1200 s. The instrument was configured with a 1/16° divergence and

1/16° antiscattering slits. A standard quartz sample holder 1 mm deep, 20 mm high and 15 mm wide was used. The crystallization index (CI) was determined using the semi-quantitative method of Person et al. (1996) [179]: CI = (h(202) + h(300) + h(112))/h(211). The heights of the (202), (300) and (112) hydroxylapatite peaks were measured as the difference between the average intensity recorded at the top of the peak and the intensity of the valley separating the peak from the previous one; or, for (211), as the height from the baseline between 32° and 43° 2Θ. The CI was the average value of two or three measurements with an error of ±0.01. The crystallite domains size was semi-quantitatively estimated by the Scherrer equation [180]: $D= (K\lambda 57.3/ \beta_{1/2} (\cos\theta)$ Here, D is the average domain size (roughly the crystallite size), ; K is a constant that was set to 1 (as often done), $\beta_{1/2}$ is the peak width (as full-width at half maximum) in °2Θ, λ is the X-ray wavelength in Å and Θ is the diffraction angle of the corresponding reflex. This equation gives an estimate of the crystallite size. It should be noted, however, that structural disorder and strain phenomena, e.g. caused by carbonate substitution, can also lead to a peak broadening effect [180]. Therefore, the given values should be mainly used for comparison among the samples. A Rietveld program (Quanto) for quantitative phase analysis of polycrystalline mixtures from powder diffraction data was used to quantify mineral phases and to evaluate the unit cell parameters [181].

5.3.3 Results

Qualitative analysis

Figure 5.3.1 shows the GC-MS trace of pyrolysate of sample T67. Structural assignments of numbered peaks are reported in table 5.3.1. Also listed are the retention times, mass spectra and molecular attributions. In particular, the attributions were based on studies reported in the literature about pyrolysis products of some oligo-peptides [98,186], collagen in human tissue [176] and protein markers detected in cooked meat [77], and on data reported in chapter 4 on the pyrolysis of model compounds. The first elution region of the chromatogram is occupied by peaks associated to thermal degradation products of side chains of amino acids (peaks from #1 to #12). At higher times the GC trace is featured by the elution of cyclo dipeptides. The same DKPs were identified in the pyrolysates of collagen and BB. Since the peak shape of relatively polar cyclo (Pro-Gly) and cyclo (Pro-Hyp) was broad (large and asymmetric peaks) a sylilation procedure was performed. Figure 5.3.2. shows the GC-MS trace of the silylated pyrolysate of sample T67. Structural assignments of numbered peaks are reported in table 5.3.2 together with retention times. The identification of TMS derivatives was made in a recent study on pyrolysis of model [182]. DKPs found in collagen and BB (table 5.3.3) were selected for quantitation. Molecular attributions of thermal fragments (from peak #1 to #11 – table 5.3.1) considered less specific of collagen were based on studies reporting

pyrolysis products of amino acids (Stankiewicz et al 1997) [177], dipeptides (Smith 1988) [83] and soil humic substances [183], or attribution was uncertain (NIST).

Quantitative analysis

More polar DKPs – cyclo (Pro-Gly), (Pro-Hyp), (Ala-Ala), (Gly-Ala), (Gly-Val) and -(Gly-Leu) - were quantified in the silylated form (see table 5.3.2 and table 5.3.4). DKP yields from pure collagen pyrolysis were in the 9.5% - 7.5% (w/w) range. Lower DKP yields values were obtained from BB (2.4% - 3.5%) and T67 (0.5% - 0.7%) pyrolysis due to the presence of inorganic matrix. The results are reported in detail in table 5.3.3, in which the DKPs quantified from the silylated solutions are marked by an asterisk. The mean value of RSD calculated for all the analytes result to be 20%, which is a typical error value of quantitative methods in off-line pyrolysis for the evaluation of collagen presence [170]. The most abundant DKPs from archaeological finds resulted to be diketodipyrrole and cyclo(Pro-Gly), which are also among the most abundant products from collagen pyrolysis. Cyclo(Hyp-Pro), the importance of which has been discussed already, has been detected in low amounts (0.01 % yield), with an RSD value of 30%. Matrix effects were highlighted by comparing DKP yields of standard collagen with that of BB and the archaeological sample T67 (table 5.3.3). In figure 5.3.3 the DKPs relative abundances of BB, collagen and the archaeological sample T67 are reported. The yields of DKPs produced from the pyrolysis of archaeological samples are reported in table 5.3.4.

Fourier Transform Infra Red spectra.

Part of the information provided by FTIR spectra of bones relates to the degree of crystallinity of the cHA crystals. This is a function of the extent of splitting of the two phosphate absorption bands at 603 and 565 cm^{-1} and reflects a combination of the relative sizes of the crystals and the extent to which the atoms in the lattice are ordered. As recrystallization proceeds, these two absorption peaks become increasingly separated from one another. The extent of this process is therefore measured by the SF, an average of the heights of the two peaks (baseline drawn between 495–750 cm^{-1}) divided by the height of the low point between them. The higher the SF value, the larger and/or more ordered are the crystals: hence, this crystallinity index is always lowest for fresh bone (e.g. SF=2.5–2.9) and highest for highly fossilized (or calcined) bone (e.g. SF=7.0) [174]. Figure 5.3.4 shows spectra for the archaeological bones and BB and their corresponding SFs are reported in table 5.3.5. The SF from BB sample was equal to 2.8. The samples T98 and T139 showed a SF of 4.0, while a SF of 3.2 was associated to the sample T165, being the formers the most and the latter the lowest fossilized

samples. The samples T67 and T150 gave both a SF value of 3.6. Interesting all the FTIR spectra from archaeological bones showed an absorption band at 1654 cm^{-1}, which could be associated to the amide I vibration mode typical of proteins. In the samples T98 and T139 this band overlaps with the one associated to water (1630 cm^{-1}) giving an apparent shift to lower wavenumbers.

X-ray powder diffraction patterns.

X-ray powder diffraction patterns were all characterized by the predominant presence of diffraction peaks of cHA. However, the crystallinity of the cHA varied among the different samples. It was evaluated both by estimating the CI that the crystalline domains size ($D_{(002)}$) along the crystallographic c-axis direction (table 5.3.5). These values in sample T165, CI equal to 0.02 and $D_{(002)}$ equal to 69.7 nm, are the closest to those ones in BB , CI equal to 0.01 and $D_{(002)}$ equal to 54.2 nm. Samples T98 and T139 showed the highest values of CI, 0.14 and 0.15 respectively, and the highest crystalline domains, 90.3 and 87.1 nm respectively. The samples T67 and T150 showed intermediate values of CI and $D_{(002)}$. It is worth of note the presence in all the archaeological samples of trace amounts of quartz, about 0.1% (*w*/*w*) unless the sample T98 (0.9%). Calcite was detected in the samples T67, T98 and T150 in quantity of 0.8, 1.4 and 5.1 respectively.

Thermogravimetric analyses.

The thermo gravimetric profile of sample T165, elected as example, is illustrated in figure 5.3.5. Two main weight loss regions were detected in all samples. The one in the range 250-500 °C was used to have relative estimation of the content (weight %) of organic material, while the one between 600 °C and 900 °C to assess carbonate content. All measures wee replicate three times. The results are reported in table 5.3.6. The relative content of organic material in archaeological samples ranges between 19% (T165) and 9% (T139) and is always lower than that of bovine bone, equal to 25.3%. Since the TGA analyses were carried out under a nitrogen flow the reported values of organic material do not represent the absolute values, being the organic material not completely burned.

5.3.4 Discussion

Pure collagen

Major constituents of specimens pyrolysates are DKPs, phenols and indoles produced from thermochemical degradation of bone proteins (table 5.3.1 and 5.3.2). Collagen, which constitutes more than the 90% of bones organic fraction, is made of three polypeptide chains composed mainly of glycine (*ca*. 33%), alanine (*ca*. 10%), proline (*ca*. 12%) and hydroxyproline (*ca*. 10%). The

presence of pyrolysis products originated from these amino acid is due to thermal degradation of protein content (fraction) in archaeological specimens; however, this information was not sufficient to evaluate collagen preservation as the presence in the pyrolysate patterns of amino acids markers can be due to denatured or hydrolyzed collagen (gelatin) inside bones. For this reason, only DKP yields together with TGA, FT-IR and XRD results, were considered to assess the conservation status of the analyzed specimens. As reported by previous studies [176], DKP formation from bone pyrolysis is an index of collagen preservation since the larger is the peptidic chain, the more DKPs will be formed under thermochemical treating (higher number of contiguous amino acid moieties). Cyclo (Pro-Hyp) (2.4%), cyclo (Pro-Gly), Diketodipyrrole and cyclo (Gly-Ala) were the main pyrolysis products obtained from collagen (see table 5.3.3). The amino acidic moieties of these cyclic dipeptides are the most abundant in collagen sequences and are often contiguous in collagen peptidic chain (37 linked pairs for Pro-Pro, Hyp-Hyp and Pro-Hyp , 42 for Pro-Ala and 103 for Gly-Ala, permutation of positions was considered). A recent pyrolytic study on proline containing dipeptides and collagen [182] showed proline to be one of the most prone amino acid to give cyclic dipeptides. Again, in this study proline pyrolysis derivatives, especially DKPs, were found to be the most abundant products in all the analysed pyrolysates (table 5.3.3 and table 5.3.4).

Bovine Bone (BB)

Type I collagen (the only type present in bone) is characterised by its fibrous nature, as its polypeptide chains are wound together in a triple helix to give a single fibril strictly associated with hydroxylapatatite [164]. Therefore bone mineral phase could play an important role during pyrolysis, being intimately bonded with collagen fibrils. This matrix effect was investigated by comparing DKPs relative abundances obtained from BB with that obtained from pure collagen (see fig5.3.3), calculated as DKP_i yield/ $\sum_i DKP_i$ yield * 100. The biggest difference between the samples were found for cyclo (Hyp-Pro) yields, which is the most abundant DKP evolved from pure collagen pyrolysis and its specific marker. This cyclic dipeptide gave the highest yield from the standard protein while was detected as a minor product in BB pyrolysate. Matrix effect seemed to affect also diketodipyrrole and cyclo (Pro-Pyr) formation, having both higher relative abundances in BB than in collagen pyrolysates. As reported by Smith et al. [184] pyrrole (Pyr) is one of the major pyrolysis product of hydroxyproline, and is produced by Hyp dehydration followed by dehydrogenation, being both common pyrolysis reactions [59, 185,186]. However, pyrrole can be also originated by simple dehydrogenation of proline. Since no big differences in relative abundances of proline, alanine and glycine containing DKPs could be noticed between pure collagen and BB, it is reasonable to assert that hydroxyproline moieties are the most involved in the interaction with bones inorganic phase. As

in the case of BB, the main constituent of mineral phases of the analysed archaeological specimens was hydroxylapatite. Small amounts of calcite were detected only for sample T67, T98 and T150. The DKPs relative abundances detected in specimens pyrolysates were similar to that found in BB.

Archaeological specimens

Among the analysed samples, the highest DKP yields were detected in T165 pyrolysates, followed by T150, T67, T139 and T98. This trend is in accordance with FT-IR and XRD analysis results (table 5.3.5) which were found in direct correlation. Infra red splitting factor and crystallinity index ranged respectively from 3.2 for T165 to 4.0 for T98 and T139, and from 0.02 for T165 to 0.15 for T139. If IR-SF of bones increases with increasing exposure and weathering, as suggested by Trueman et al [187] and confirmed by fresh bones analysis (BB, see table 5.3.5), the inorganic matrix of samples T98 and T139 should be the worst preserved or the most degraded, followed in order of increasing conservation status by samples T67 and T150 (same index values), and T165 (table 5.3.5). Cyclo (Pro-Gly) and Diketodipyrrole were the DKPs with the highest pyrolysis yields for all the samples, being the obtained data in the range 0.11% (T139) to 0.52% (T165) for the former and from 0.17% (T139) to 0.43% (T165) for the latter (table 5.3.4). Specimens T165 and T67 were the only archaeological samples for which higher quantities of cyclo (Pro-Gly) – 0.52% and 0.22% – were recorded respect to Diketodipyrrole – 0.43% and 0.18% – which is the most abundant DKP in BB pyrolysate. In addition T165 pyrolysates was the only sample for which cyclo (Pro-Ile) was detected, but not cyclo (Pro-Leu). Total DKP yields obtained by means of analytical pyrolysis and archaeological bones organic contents, detected by means of TGA analysis, are summarized in table 5.3.6. Data were found in complete agreement, giving a correlation coefficient of 0.98. This, together with observed DKP relative abundances, indicated that the organic matter content detected by TGA consisted mainly of well preserved collagen. The samples for which the lowest DKP yields have been recorded were in order T139 (0.54%), T67 (0.65% for n=3) and T98 (0.67%). While pyrolysis data suggested T165 to be the best preserved sample, in accordance with spectroscopic and thermogravimetric analyses, for samples T67 there is not such accordance among thermal and spectroscopic data. This specimen gave lower CI and IRSF indexes than T98 (figure 5.3.5) in accordance with a higher organic matter content, but not with DKP total yields (table 5.3.5). This may be due to the presence of other organic fraction than collagen (especially soil humic substances), or to hydrolyzed collagen. Hydroxylapatite was found to be the main constituent of the mineral phases of all the archaeological samples by means of diffractometric analysis (table 5.3.5). Low amounts of calcite were positively identified in T98, T139 and T150, the latter having an anomalous

5.3% of calcite content. In addition, sample T150 showed a perfect accordance between both thermal data (TGA and Py-GC/MS) but not between index D from XRD and IRSF from FT-IR analysis.

5.3.5 Conclusions

The high correlation between TGA data and DKP yields provided evidence on the presence of well preserved collagen inside the analysed samples. Low amounts of minerals others than hydroxylapatite were detected inside the specimens, except for sample T150 for which an anomalous amount of calcite was detected. Crystallinity index and IR-SF showed inverse correlation with bone organic matter content, so that increasing values of the latter are related to decreasing values of the former and hence to decreasing values of bone collagen content. Archaeological samples were classified by comparing all the achieved results in the following order (from best to worst preserved sample): T165, T150, T67 and jointly T98 and T139. Average domain size $D_{(002)}$ is in accordance with this results except for sample T150 for which, despite a high collagen content and a low hydroxylapatite crystallinity degree was recorded a 81.2 value, which is higher respect to that recorded for sample T67. Pyrolysis GC-MS was proved to be a very reliable method to assess and quantify collagen presence inside bones by comparison with TGA, XRD and FT-IR results. In particular, quantified DKPs showed to have a very conservative distribution pattern among all the pyrolysed collagenous samples and were therefore suitable for collagen assessment inside archaeological specimens.

Figure 5.3.1. Total ion chromatogram of the pyrolysate of sample T67 Peak numbers refer to compounds listed in table 5.3.1

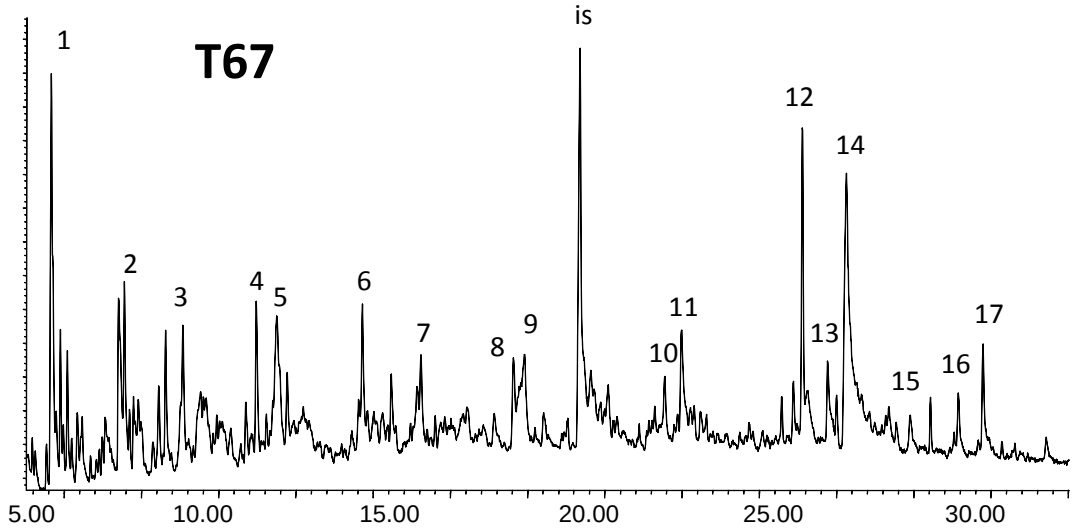

Figure 5.3.2. Total ion chromatogram of the silylated (SYL) pyrolysate of sample T67
Peak numbers refer to compounds listed in table 5.3.2

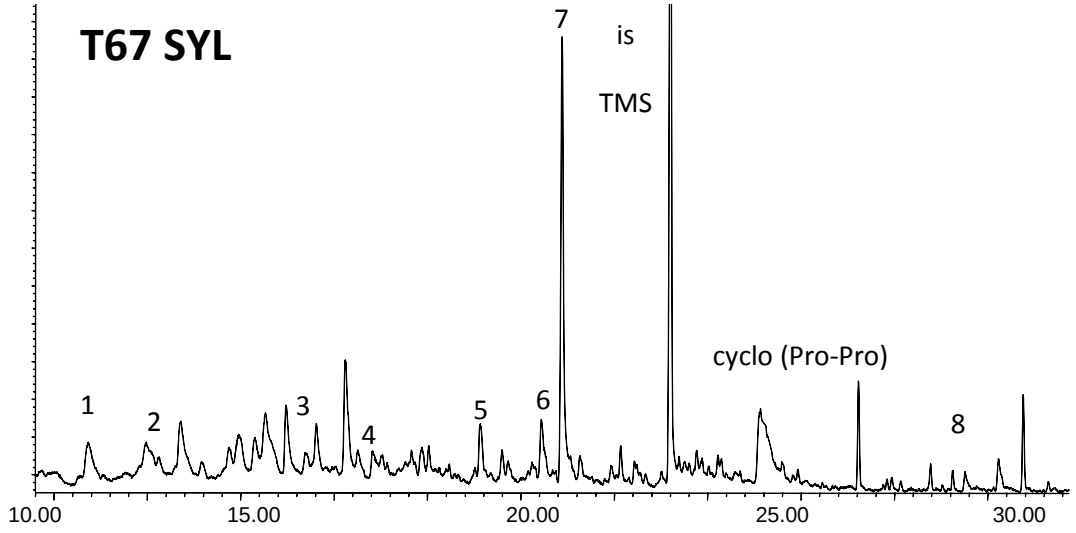

Table 5.3.1. GC-MS characterisation of compounds tentatively identified in the pyrolysate of archaeological samples

N°	Compound	RT (min)	m/z
1	4-hydroxy-pyrimidine	4.14	44, 53, 67, **80**, 95
2	pyrrole	5.68	40, 53, **80**, 81
3	pyridinamine	7.43	67, **94**
4	1H-pyrrole, 2,3,4,5-tetramethyl-	11.03	108, 109, **122**, 123, 138
5	benzylnitrile	11.33	51, 89, **90**, 116, 117
6	benzen-propan-nitrile	14.08	65, 90, **91**, 131
7	indole	15.25	63, 89, **90**, 117
8	methyl-indole	17.67	77, 103, **130**, 131
9	methyl-pyrimidone	17.93	54, 69, 111, **138**
is	sarcosine anhydride (is)	19.37	57, 85, 113, 142
10	phenyl-pyrrole	21.55,	89 , 115, 116, 143
11	diethyl-pyrazine	22.00	**136**, 108, 107, 80, 53
12	diketodipyrrole	25.11	65, 93, 130, ***186***
13	cyclo(Pro-Ala)	25.24	44, **91,** 127,*218*
14	cyclo(Pro-Gly)	26.23	83, 98, **111**, *154*
15	cyclo(Pro-Val)	27.91	**70**, 72, 125, **154**, *(196)*
16	cyclo(Pro-Pyr)	29.17	70, 94, **191**, 192
17	cyclo(Pro-Pro)	29.79	**70**, 96, 138, 166, ***194***

Table 5.3.2. GC-MS characterisation of compounds tentatively identified in the silylated pyrolysate of archaeological samples

N°	Compound	RT (min)	m/z
1	cyclo(Ala-Ala) TMS	11.57	156, 171, 255, **271**, *286*
2	cyclo(Gly-Ala) TMS	12.76	129, 142, 241, **257**, *272*
3	cyclo(Gly-Val) TMS	15.45	142, 170, 257, **285**, *300*
4	cyclo(Gly-Leu) TMS	16.83	156, **257**, 271, 299, *314*
5	cyclo(Pro-Ala) I TMS	19.10	70, 97, 170, 225,***240***
6	cyclo(Pro-Ala) II TMS	20.38	70, 97, 170, 225,***240***
7	cyclo(Pro-Gly) TMS	20.89	70, 83, 183, 211, ***226***
is TMS	1,3 benzyl-oxo-piperazine (OPI) (is) TMS	23.12	73, 91, **171**, 247, *262*
8	cyclo (Pro-Hyp) TMS	30.20	70, 124, 156, **267**, *282*

Table 5.3.3. Calculated DKP yields (% w_{dkp} / w_{sample}). Compound marked with the asterisk were quantified in silylated pyrolysates.

	BB (n=3)	RSD	Collagen (n=3)	RSD
diketodipyrrole	0.97	15	1.32	6
cyclo(Pro-Ala)	0.17	5	0.42	5
cyclo(Pro-Gly)*	0.74	28	1.68	10
cyclo(Pro-Val)	0.10	16	0.26	3
cyclo(Pro-Pyr)	0.20	18	0.11	3
cyclo(Pro-Pro)	0.14	24	0.29	1
cyclo(Pro-Ile)	0.03	14	0.05	13
cyclo(Pro-Leu)	0.03	13	0.24	14
cyclo(Ala-Ala) *	0.07	13	0.25	24
cyclo(Gly-Ala)*	0.30	16	1.00	15
cyclo(Gly-Val *	0.03	31	0.18	44
cyclo(Gly-Leu)*	0.04	41	0.23	48
cyclo(Hyp-Pro)*	0.12	11	2.48	13

Table 5.3.4. Calculated DKP yields (% w_{dkp} / w_{sample})

	T67	T98	T139	T150	T165	RSD (from T67 n=3)
diketodipyrrole	0.18	0.23	0.17	0.24	0.43	14
cyclo(Pro-Ala)	0.05	0.05	0.05	0.06	0.12	11
cyclo(Pro-Gly)*	0.22	0.15	0.11	0.20	0.52	19
cyclo(Pro-Val)	0.04	0.05	0.04	0.06	0.10	25
cyclo(Pro-Pyr)	0.02	0.02	0.02	0.02	0.01	5
cyclo(Pro-Pro)	0.04	0.04	0.05	0.04	0.09	25
cyclo(Pro-Ile)	0.00	0.00	0.00	0.00	0.07	-
cyclo(Pro-Leu)	0.03	0.03	0.02	0.03	0.00	5
cyclo(Ala-Ala) *	0.01	0.01	0.01	0.02	0.03	36
cyclo(Gly-Ala)*	0.02	0.04	0.04	0.05	0.11	30
cyclo(Gly-Val *	0.00	0.01	0.01	0.01	0.02	34
cyclo(Gly-Leu)*	0.00	0.01	0.01	0.01	0.02	33
cyclo(Hyp-Pro)*	0.01	0.01	0.01	0.02	0.03	30

Figure 5.3.3 Relative DKP yields of collagen and osteological samples
DKP_i Yield/ $\sum_i DKP_i$ Yield * 100

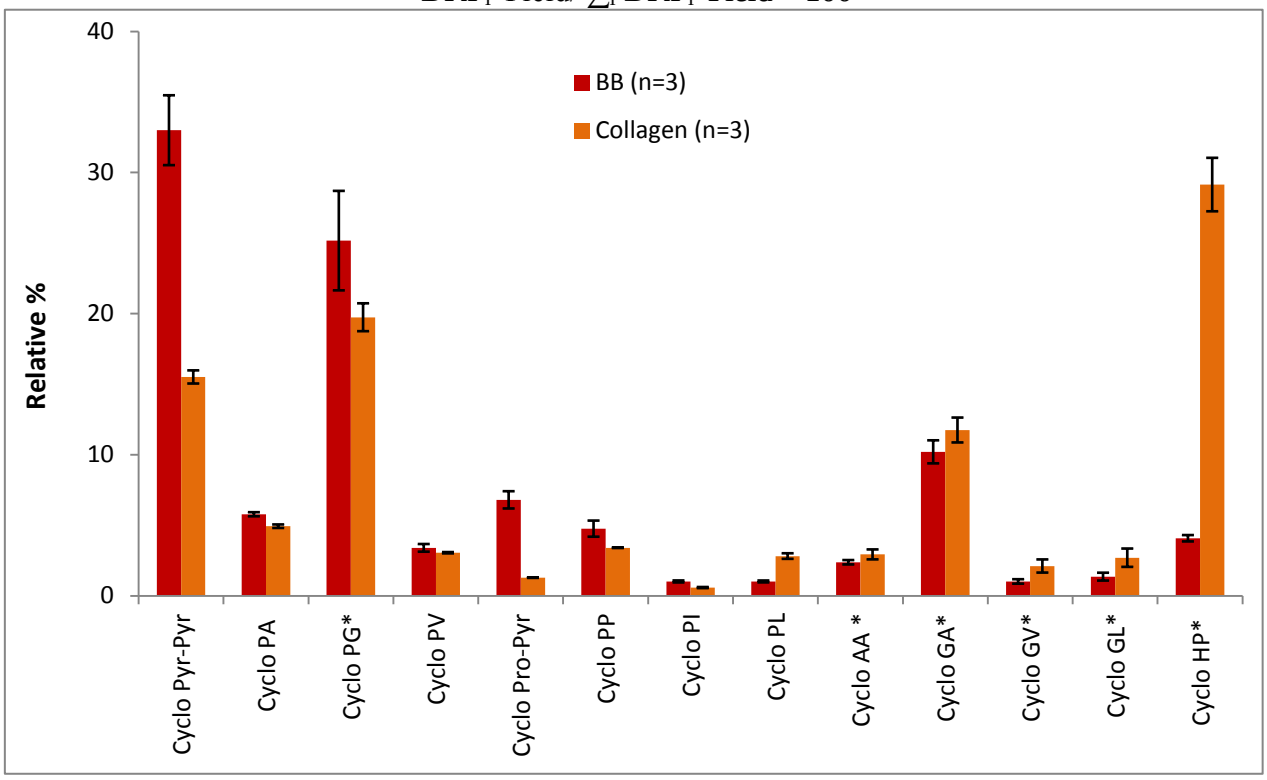

Figure 5.3.4 XRD FTIR. *Left* X-ray diffraction patterns of archaeological bone samples (T67, T98, T139, T150 and T165) and bovine bone (BB). The diffraction peaks of calcite (Cal) and quartz (Qtz) are indicated. The Miller index of the diagnostic diffraction peaks for cHA are reported above the BB diffraction pattern. *Right* FTIR spectra of archaeological bone samples (T67, T98, T139, T150 and T165) and bovine bone (BB). The proteic bands amide I and amide II, and the carbonatic band, are indicated. The phosphate bands used for the SF calculation are squared.

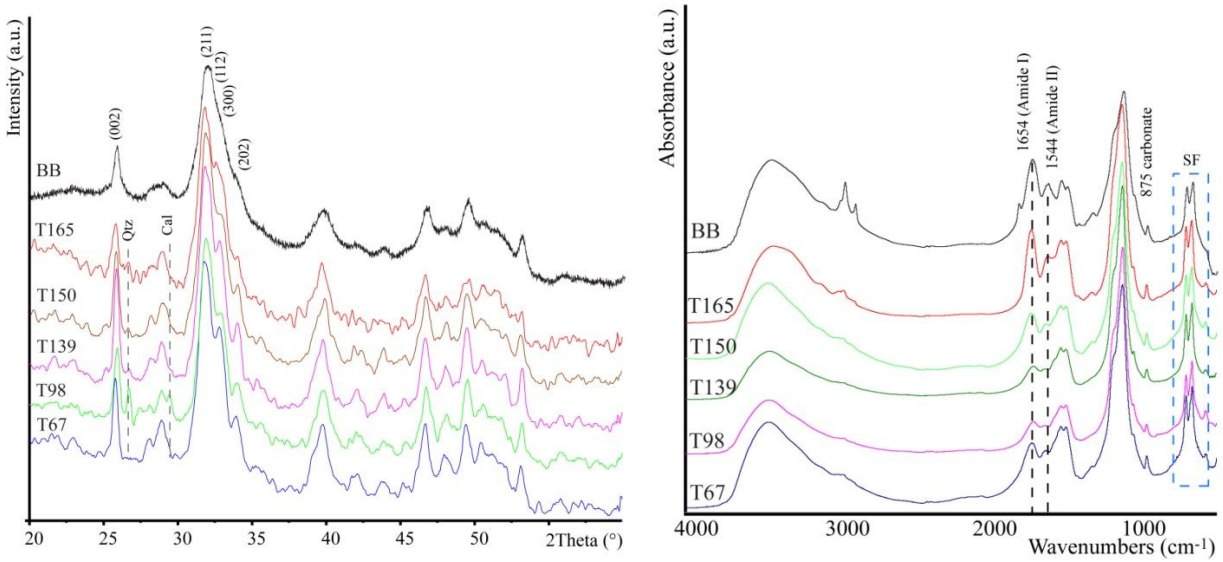

Figure 5.3.5 TGA. Thermogravimetric profile obtained from sample T 165. The weight loss is attributed to specimen organic fraction

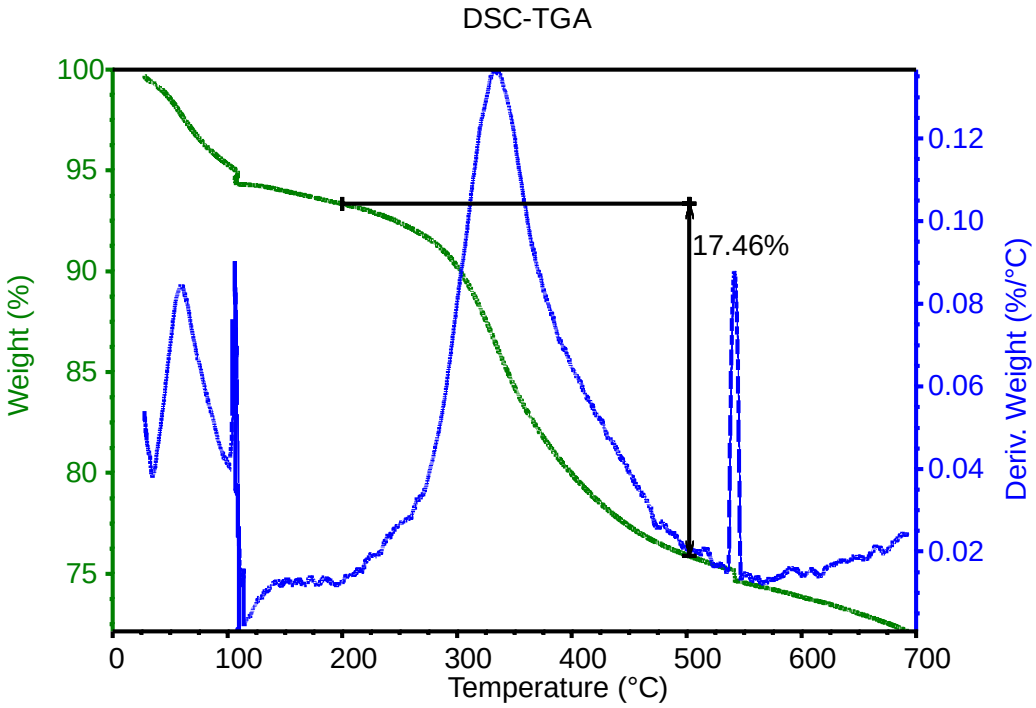

Table 5.3.5 Characterization of minerals associated to bones

Samples	XRD					FTIR
	cHA*	calcite	quartz	$D_{(002)\,(nm)}$	CI	SF
T67	99.1	0.8	0.1	78.65	0.12	3.6
T98	97.7	1.4	0.9	90.30	0.14	4.0
T139	99.9	-	0.1	87.07	0.15	4.0
T150	94.8	5.1	0.1	81.27	0.08	3.6
T165	99.9	-	0.1	69.66	0.02	3.2
Bovine bone (BB)	100.0	-	-	54.18	$0.01^{-\varsigma}$	2.8

* mineral (%) composition in bones evaluated by X-ray powder diffraction; $^{-\varsigma}$ not exactly estimable

Table 5.3.6

Organic contents (%) by TGA and DKP yields (%) by analytical pyrolysis in archaeological specimens

Samples	Organic matter	$\sum_i$ DKP$_i$ % yields
T67	10.9	0.62
T98	10.0	0.65
T139	9.1	0.54
T150	12.7	0.76
T165	19.2	1.55
Bovine bone (BB)	25.3	2.94

5.4 Intrinsecally unfolded protein

5.4.1 Introduction

Biomineralization is the process by which living organisms produce hard tissues such as bones, teeth and shells [188]. Crystals deposited by organism are characterized by high degree of control over the location, size, structure, shape and orientation. For many years, it has been widely believed that the exquisitely precise nature of crystal formation in biological tissues is the result of stereochemically specific interactions between growing crystals and extracellular matrix proteins [189; 190]. That is, the ability of many mineralized tissue proteins to adsorb particular faces of biominerals has been attributed to a steric and electrical complementarity between periodic regions of the polypeptide chain and arrays of ions on the crystal face. In recent years, however, evidence has accumulated that many mineral-associated proteins lack periodic structure, when dissolved in solution. This has suggested that mineral associated proteins can be part of the class of intrinsically unstructured proteins (IUPs) and that they eventually assume an order conformation only when interacting with crystalline faces of minerals. Ameloblastin, a calcium phosphate interacting protein, is suggested to be a (IUPs) having two domains, one of which binds calcium [191]. Amelogenin, the protein responsible for enamel formation, has been also supposed to belong to the IUPs class [192]. Statherin, a protein present in saliva, undergoes a structural reorganization when adsorbed on apatite crystals [193]. Amos and Evans [194] have demonstrated that the AP7 proteic fragment from the nacre induces the precipitation of aragonite and reorganized its structure. A recent research has also demonstrated that specific acidic polypetides assume a helical conformation when interacting with calcium carbonate or calcium oxalate crystalline planes [195]. Moreover, it has proposed that the interaction is mainly governed by electrostatic interactions. Parallel studies on the kinetics of polyelectrolyte adsorption on calcite achieved the same conclusions [196]. In the shell of the gastropod mollusc *Haliotis rufescens* (red abalone) green organic sheets are interspersed through the nacre at irregular intervals [197]. Recently, it has been shown that the green sheet shares common features with the organic matrix present in the nacre and the periostracum has functions similar to those of the myostracum [198]. Thus, although the green sheet is reported to be unique to the abalone shell, it represents an interesting model for the study of molluscan shell biomineralization processes. It was reported that after a harsh alkaline digestion of the green layer a water soluble polypeptide (GP) of about 6.5 kDa remained. GP had a amino acid composition similar to that of the parent green sheet and showed similar spectroscopic properties [198]. Thus, it has the potentiality to be used as a soluble analogous of the nucleating green sheet [199]. The aim of this work was to get structural information on GP, as it can be of great importance for the understanding of their

interaction with growing calcium carbonate crystals and their ability to govern its crystallization process.

5.4.2 Materials and methods

Chemicals

The dipeptides were purchased from GenScript, USA Inc. Sarcosine anhydride, 1-oxo-3-benzopiperazine and N,O-bis-(trimethylsilyl)-trifluoroacetamide (BSTFA) were purchased from Sigma-Aldrich.

Pyrolysis

Off-line pyrolysis experiments were conducted with a heated platinum filament coil of the pyroprobe model 1000 (CDS Analytical Inc.) utilising the apparatus described in previous publications [D. Fabbri]. 1.25 mg of samples were pyrolysed at 500 °C (measured temperature) for 100 s at the maximum heating rate (20 °C ms^{-1}) under nitrogen flux (200 mL min-1). The thermocouple (Delta OHM HD 2108.1 – Tessid S.r.l.) used to measure the effective temperature was placed in the sample holder during a pyrolysis simulation. Pyrolysis products were trapped onto a XAD-2 resin (orbo-43) purchased from Supelco. After pyrolysis, the cartridge was eluted with 5 mL of acetonitrile. The solutions were collected, concentrated under a gentle nitrogen stream and spiked with 0.1 mL of 250 mg l^{-1} of sarcosine anhydride solution in ACN before being analyzed in GC-MS. An aliquot (0.1 mL) was withdrawn from the solution and subjected to the derivatisation procedure for the conversion into the trimethylsilyl (TMS) derivatives as follows. The aliquot was placed in a vial and added with 0.05 mL of 250 mg L^{l-} of 1-oxo-3-benzopiperazine (internal standard for silylation) in ACN and 0.03 mL of N,O-bis-(trimethylsilyl) trifluoroacetamide (BSTFA) plus 1% trimethylchlorosilane (TMCS). The reaction of the extract aliquot with N,O-bis-(trimethylsilyl) trifluoroacetamide was carried out at 60 °C for approximately 3h prior to analysis.

GC-MS analysis

Sample solutions were injected under splitless conditions into the injector port of an Agilent 6850 gas chromatograph connected to an Agilent 5975 quadrupole mass spectrometer. Analytes were separated by a DB-5HT (Agilent Technology) fused-silica capillary column (stationary phase poly (5% diphenyl/ 95% dimethyl) siloxane, 30 m, 0.25 mm i.d., 0.10 μm film thickness) using helium as carrier gas (at constant pressure, 33 cm s^{-1} linear velocity at 200 °C). The underivitized solutions were separated with the following temperature programs: from 50 °C to 300 °C (held 5 min) at 5°C min-1, with GC injector port maintained at 260°C. The silylated solutions were separated with the following temperature programs: from 100 °C (held 5 min) to 310 °C at 5°C min-1, with GC

injection port maintained at 280 °C. GC-MS interface, and quadrupole were maintained at 280 and 250 °C, respectively for all the analysis. Mass spectra were recorded in the full scan acquisition mode under electron ionisation (70 eV) at 1 scan s^{-1} in the 35–650 m/z range.

Figure 5.4.1 Total ion chromatogram (bottom) and extracted mass chromatogram at m/z 70 (top) obtained from Py-GC-MS of GP. Peak numbers correspond to compounds listed in table 5.4.1.

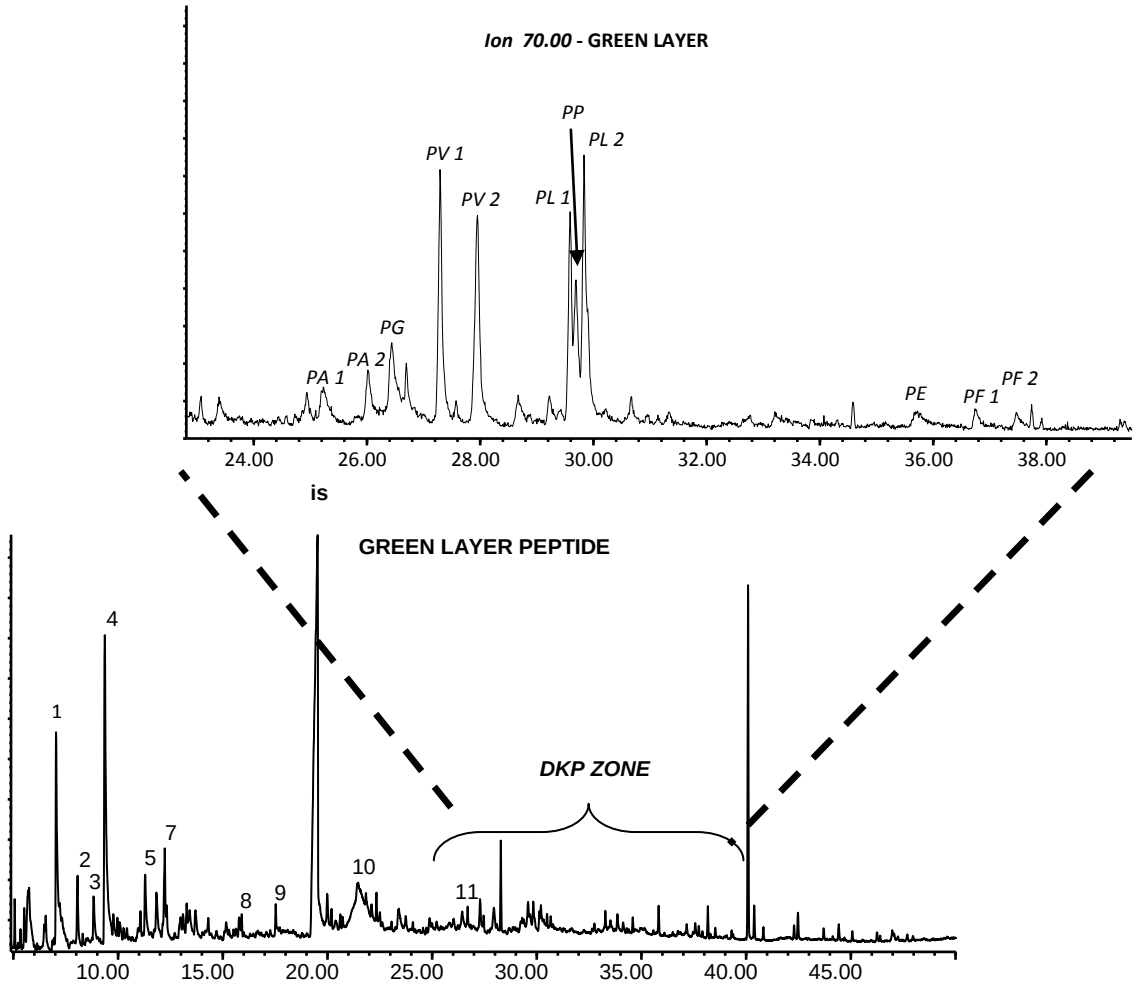

Figure 5.4.2 – Green layer total ion pyrogram. Peaks marked by an asterisk are likely to correspond to Tyr-Tyr thermal degradation products (see chapter 4 paragraph 4.2.8 and figure 4.2.3) .

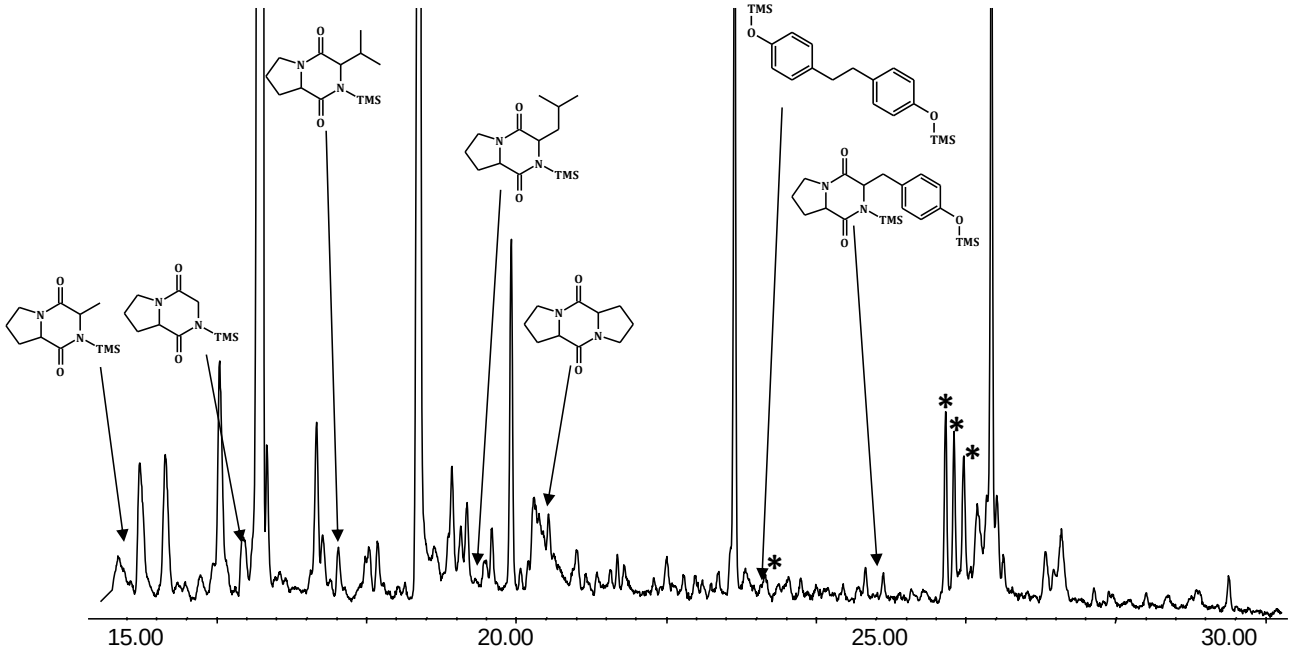

Table 5.4.1 Major pyrolysis products of green layer peptide

Peak n°	Compound	Retention Time	Ions
1	phenol	7.06	***94***,66,65
2	cyclopentanedione,3-methyl	8.07	***112***, 55, 69, 83
3	4-methyl-phenol	8.83	***108***, 107,77, 90
4	3-methyl-phenol	9.36	**107**, *108*,77, 90
5	dimethyl-phenol	11.30	***122***, 107, 77, 91
6	ethyl-phenol	11.84	**122**, *107*, 77, 91
7	unknown	12.24	**69**, 57, 85, 70, 116
8	indole	15.17	***117***, 90, 63, 89
9	methyl-indole	17.52	**130**, *131*, 77, 103
10	anhydro sugar	21.55	**60**, 73, 57, 143
11	cyclo(Pro-Gly)	26.477	**83**, 111, *154*, 70

5.4.3 Results and Discussion

All the attempts conducted to obtain information of the primary structure of GP, or even the N-terminal sequence, failed. Only analytical flash pyrolysis combined with GC–MS analysis [176] succeeded to give info. The pyrolysate of GP was dominated by phenol derivatives arising from the thermal degradation of tyrosine residues. Several cyclodipeptides (2,5-diketopiperazines, DKPs) were identified as typical cyclyzation products of two adjacent residues. In accordance with their abundance, the recovered DKPs were indicative of peptide pairs of Pro with Gly, Ala, Val, Leu and Ile, as well as Val-Gly and Val-Val (figure 5.4.1). A silylation procedure was found to be necessary

since some phenol derivatives from tyrosine exhibit predominance in the pyrogram, while others like tyrosine containing DKPs eluded GC-MS detection. The analysis of the derivatized solution provided evidence for the existence of peptide pairs Tyr-Tyr, with three intense ion peaks at m/z 179 (peaks marked by an asterisk in figure 5.4.2) also present in the silylated pyrolysate obtained from the pure dipeptide, and Pro-Tyr (silylated DKP).

6. Conlcuding remarks

A quali-quantitative analytical method based on analytical flash pyrolysis with a resistively heated platinum filament followed by gas chromatography-mass spectrometry (GC-MS) was developed to study the thermal degradation products of proteins. The method was focused to the determination of cyclic dipetides (2,5-diketopiperazine, DKPs), since these compounds are largely recognized as characteristic markers of protein pyrolysis and are reported in the literature to be formed from the pyrolysis of a great number of proteins. In addition, these compounds can provide information regarding amino acid connectivity inside the peptide chain from which they originated. The method developed in this thesis consisted in the pyrolysis at 500 °C of a tiny amount of sample (1-10 mg) under nitrogen, trapping the evolved products in a adsorbent, elution of the DKPs and other products with acetonitrile. The solution added with a standard was then subjected to GC-MS analysis. The GC-MS determination of polar DKPs was improved by trimethylsilylation of the piperazinic nitrogen atoms and side chains bearing polar functionalities, such as amino, hydroxyl and carboxylic groups.

The structural identification of DKPs was performed by the analysis of several linear dipeptides, in particular those containing proline and/or polar amino acids, such as glutamic and aspartic acids. In fact, literature data regarding the formation of DKPs from polar amino acids were scant. More than 80 DKPs, original or trimethylsilylated, were tentatively identified including DKPs not previously reported in the literature. Among these novel DKPs, the structure of cyclo(pyroGlu-Pro) could be successfully confirmed by NMR analysis of the compound isolated from the pyrolysate of the dipeptide Pro-Glu. This DKP was then identified in the pyrolysates of proteins, such as serum bovine albumin (BSA) and collagen. Several DKPs containing a butenyl-type structure joined to the piperazine ring were revealed from the pyrolysis of Lys containing peptides and were assumed to be specific markers of Pro-Lys units.

The formation of cyclo(Pro-Glu), cyclo(Pro-Lys), cyclo(Pro-Gln) and cyclo(Pro-Asp) could be tentatively confirmed by the MS fragmentation pattern of the silylated derivatives formed from the corresponding linear dipeptides. However, these DKPs could not be revealed in the pyrolysate BSA and collagen, probably because of the intrinsic low yields of DKP formation.

Besides qualitative analysis, the developed procedure enabled the estimation of the yields of DKPs produced upon pyrolysis. The yields occurred in the range of parte per mil in the case of BSA or % in the case of collagen for the most abundant DKPs.

This study confirmed the well known fact that DKPs are promptly formed from the pyrolysis of peptides and proteins. In accordance, DKPs were identified as important components in bio-oils resulting from the pyrolysis of microalgae. In particular, DKPs are among the principal compound

classes and the most important nitrogen-containing fraction in bio-oils of both *Nannochloropsis* and *Desmodesmus*. Bio-oil from *Desmodesmus* contained a greater DKPs content of DKPs with respect to *Nannochloropsis*; similarly the content of nitrogen from elemental analysis was higher in the bio-oil from *Desmodesmus* . However, DKPs were not detected in the bio-oil of *Botryococcus braunii*, which was found to consist mainly of hydrocarbons.

It was postulated that the yields of DKPs could be affected by interaction of protein with active solids. On this hypothesis, the analytical method was applied to investigate surface interaction between BSA and synthetic chrysotile nanofiber undoped and doped with iron content (0.52, 1.78%) based on the different evolution of DKPs from the corresponding protein/chrysothile adducts. Qualitatively the DKP distribution was not affected, however changes were registered in their quantitative production. The yield of cyclo(Pro-Leu) decreased in the order neat BSA, BSA adsorbed onto pure chrysothile and BSA adsorbed onto iron doped chrysotile. The yield of cyclo(Ala-Ala) and cyclo(Ala-Gly) as well as that of pyroglutamic acid were maximised for the BSA adducts with chrysotile doped with 0.52% iron. These results suggested different degrees of surface interactions of BSA with chrysotiles and were confirmed by FTIR analysis showing variation in the contribution of secondary structures of BSA adsorbed onto chrysotile nanofibers doped with iron.

The determination of thermally produced DKPs was used to evaluate the conservation status of archaeological bones found in Vicenne Necropolis (Molise – Italy). A quantitative method of DKPs evolved from pure collagen pyrolysis was applied to five archaeological samples. These data were compared to those obtained from thermogravimetry (TGA), showing a strong correlation between DKPs amount and bones organic matter content ($R2 = 0.98$), confirming that the organic matter of the samples was largely collagen. In addition, FTIR and XRD analysis were performed on the samples to evaluate the conservation status of bones inorganic matrix (mainly hydroxyl apatite).

The case study investigated in this thesis showed that the GC-MS determination of DKPs evolved from pyrolysis of proteinaceous materials provided information consistent with the results obtained from complementary techniques. The GC-MS data set collected in this study from the pyrolysis of several model compounds could be usefully employed to identify DKPs in samples formed from the thermal treatment of protein-containing materials, such as food, cigarette smoke, bio-oil, and so forth.

References

[1] Labeit S and Kolmerer B. Titins: Giant Proteins in Charge of Muscle Ultrastructure and Elasticity. *Science,* 1995, 270 (5234): 293-296.

[2] Venkatachalam CM. Stereochemical criteria for polypeptides and proteins. V.. Conformation of a system of three linked peptide units. *Biopolymers,* 1968, 6 (10): 1425-1436.

[3] Mathews DH. Revolutions in RNA Secondary Structure Prediction. *Journal of molecular biology,* 2006, 359 (3): 526-532.

[4] Dreizen P, Geirshman LC, Trotta PP and Stracher A. Myosin Subunits and their interactions. *Journal of General Physiology,* 1967: 85-118.

[5] Od T, Iwasa M, Aihara T, Maéda Y, Narita A. The nature of the globular-to fibrous-actin transition. *Nature,* 2009, 457: 441-445.

[6] Anson ML and Mirsky AE. The estimation of pepsin with hemoglobin. *The Journal of general physiology*, 1932: 59-63.

[7] Mirsky AE and Pauling L. On the Structure of Native, Denatured, and Coagulated Proteins. *Proceedings of the National Academy of of Sciences of the United States of America*, 1936 22(7): 439–447.

[8] Neurath H, Greenstein JP, Putnam FW, Erickson JA. The Chemistry of Protein Denaturation. *Chemistry Reviews,* 1944, 34 (2): 157–265.

[9] Tanford C. Protein Denaturation. *Advances in Protein Chemistry,* 1968, 23: 121–282.

[10] Wright PE and Dyson HJ. Intrinsically unstructured proteins: re-assessing the protein structure-function paradigm. *Journal of molecular biology*, 1999, 293(2): 321-331.

[11] Belcher AM, Wu XH, Christensen RJ, Hansma P K., Stucky GD, Morse DE. Control of crystal phase switching and orientation by soluble mollusc-shell proteins. *Nature,* 1996, 381: 56 - 58

[12] Erasmus J, Cook PA and Sweid N. Internal shell structure and growth lines in the scell of the Abalone, Haliotis midae. *Journal of Shellfish Research,* 1994, 13 (2): 493-501

[13] Wilt FH, Killian CE and Livingston BT. Development of calcareous skeletal elements in invertebrates. *Delta*, 2003*:* 237-250.

[14] Werkstoffe K and Klopferspitz A. The nacre protein perlucin nucleates growth of calcium. *Journal of Microscopy,* 2003, 212: 280-291 .

[15] Su XW, Belcher AM, Zaremba CM, Morse DE, Stucky GD and Heuer AH. Structural and microstructural characterization of the growth lines and prismatic microarchitecture in red abalone shell and the microstructures of abalone "flat pearls". *Chemistry of Materials,* 2002 14: 3106-3117.

[16] Falini G *et al.* The interstitial crystal-nucleating sheet in molluscan Haliotis rufescens shell : A bio-polymeric composite. *Journal of Structural Biology*, 2011 173: 128-137.

[17] Salas C, Rojas OJ, Lucia L, Hubbe M and Genzer J. Adsorption of Glycinin and β-Conglycinin on Silica and Cellulose: Surface Interactions as a Function of Denaturation, pH, and Electrolytes. *Biomacromolecules*, 2012. doi:10.1021/bm2014153

[18] Drummond TG, Hill MG and Barton JK. Electrochemical DNA sensors. *Nature biotechnology*, 2003, 21: 1192-9.

[19] Pereiradeabreu D, Paseirolosada P, Angulo I and Cruz J. Development of new polyolefin films with nanoclays for application in food packaging. *European Polymer Journal*, 2007, 43: 2229-2243.

[20] Colvin VL. The potential environmental impact of engineered nanomaterials. *Nature biotechnology*, 2003, 21: 1166-70.

[21 a] Limbach LK, Li Y, Grass RN et al. Oxide nanoparticle uptake in human lung fibroblasts: effects of particle size, agglomeration, and diffusion at low concentrations. *Environmental science & technology*, 2005, 39(23): 9370-6.

[21 b] Limbach LK, Ludwig K, Wick P, Manser P, Grass RN., Bruinink A.,Stark, Wendelin J.. Exposure of engineered nanoparticles to human lung epithelial cells: influence of chemical composition and catalytic activity on oxidative stress. *Environmental science & technology*, 2007, 41: 4158-63.

[22] Lin W, Huang YW, Zhou XD and Ma Y. In vitro toxicity of silica nanoparticles in human lung cancer cells. *Toxicology and applied pharmacology*, 2006, 217: 252-9.

[23] Drescher D, Orts-Gil G, Laube G et al. Toxicity of amorphous silica nanoparticles on eukaryotic cell model is determined by particle agglomeration and serum protein adsorption effects. *Analytical and bioanalytical chemistry*, 2011, 400(5):1367-73.

[24] García A et al. Acute toxicity of cerium oxide, titanium oxide and iron oxide nanoparticles using standardized tests. *Desalination, 2011,* 269: 136-141.

[25] Kyung Eun CHA., Myung H. Cytotoxic Effects of Nanoparticles Assessed In Vitro and In Vivo. *Journal Microbiology and Biotechnology*, 2007, 17 (9): 1573–1578.

[26] Yu KO, Grabinski CM, Schrand AM et al. Toxicity of amorphous silica nanoparticles in mouse keratinocytes. *Journal of Nanoparticle Research*, 2008, 11(1):15-24.

[27] Pan Y, Neuss S, Leifert A et al. Size-dependent cytotoxicity of gold nanoparticles. *Small (Weinheim an der Bergstrasse, Germany*), 2007, 3(11):1941-9.

[28] McDonald JC, Liddell FD, Gibbs GW, Eyssen GE, McDonald D. Dust exposure and mortality in chrysotile mining, 1910-75. *British journal of industrial medicine,* 1993, 50(12): 1058-72.

[29] Goodglick LA, Kane AB. Role of Reactive Oxygen Metabolites in Crocidolite Asbestos Toxicity to Mouse Macrophages. *Cancer research*, 1986, 46: 5558-5566.

[30] Huang SXL, Jaurand MC, Kamp DW, Whysner J, Hei TK. Role of mutagenicity in asbestos fiber-induced carcinogenicity and other diseases. *Journal of toxicology and environmental health. Part B, Critical reviews*, 2011, 14(1-4): 179-245.
[31] Belgorodsky B, Fadeev L, Kolsenik J, and Gozin M. Formation of a soluble stable complex between pristine C60-fullerene and a native blood protein. *Chembiochem*, 2006, 7: 1783–1789.
[32] Matsuura K, Saito T, Okazaki T, Oshshima S, Yumura M, and Iijima S. Selectivity of water-soluble proteins in single-walled carbon nanotube dispersions. *Chemical Physical Letters*, 2006, 429: 497–502.
[33] Dutta D, Sundaram SK, Teeguarden JG et al. Adsorbed proteins influence the biological activity and molecular targeting of nanomaterials. *Toxicological sciences : an official journal of the Society of Toxicology*, 2007, 100(1): 303-15.
[34] Cedervall T, Lynch I, Foy M et al. Detailed identification of plasma proteins adsorbed on copolymer nanoparticles. *Angewandte Chemie (International ed. in English)*, 2007 46(30): 5754-6.
[35] Gray JJ. The interaction of proteins with solid surfaces. *Current opinion in structural biology*, 2004, 14(1): 110-5.
[36] Roveri N, Falini G, Foresti E et al. Geoinspired synthetic chrysotile nanotubes. *Journal of Material Science*, 2006, 21 (11): 2711-2725.
[37] Gazzano E, Foresti E, Lesci IG et al. Different cellular responses evoked by natural and stoichiometric synthetic chrysotile asbestos. *Toxicology and applied pharmacology*, 2005, 206(3): 356-64.
[38] Foresti E, Fornero E, Lesci IG et al. Asbestos health hazard: a spectroscopic study of synthetic geoinspired Fe-doped chrysotile. *Journal of hazardous materials*, 2009, 167(1-3): 1070-9.
[39] Yamaguchi K.. Recent advances in microalgal bioscience in Japan, with special reference to utilization of biomass and metabolites: a review. *Journal of Applied Phycology*,1997, 8 (6): 487-502.
[40] Spolaore P, Joannis-Cassan C, Duran E, Isambert A. Commercial applications of microalgae. *Journal of bioscience and bioengineering*, 2006, 101(2): 87-96.
[41] Borowitzka MA. Commercial production of microalgae: ponds, tanks, and fermenters. *Journal of Biotechnology*, 1999, 35: 313–321.
[42] Malcata FX. Microalgae and biofuels: A promising partnership? *Trends in biotechnology*, 2011, 29(11): 542-549.
[43] Torri C, Samorì C, Adamiano A et al. Preliminary investigation on the production of fuels and bio-char from *Chlamydomonas reinhardtii* biomass residue after bio-hydrogen production. *Bioresource technology*, 2011, 102(18): 8707-13.

[44] Metzger MP. Botryococcus braunii : a rich source for hydrocarbons and related ether lipids. *Applied Microbiology*, 2005: 486-496.
[45] Alba LG, Torri C, Samorì C et al. Hydrothermal Treatment (HTT) of Microalgae : Evaluation of the Process As Conversion Method in an Algae Biorefinery Concept. *Energy & Fuels*, 2012: 642-657.
[46] Torri C, Alba LG, Samorì C, Fabbri D, Brilman DWFW. Hydrothermal Treatment (HTT) of Microalgae : Detailed Molecular Characterization of HTT Oil in View of HTT Mechanism Elucidation. *Energy & Fuels*, 2012:658-671.
[47] Huntley ME, Redalje DG. CO2 Mitigation and Renewable Oil from Photosynthetic Microbes: A New Appraisal. *Mitigation and Adaptation Strategies for Global Change,* 2007, 12: 573–608.
[48] Chisti Y. Biodiesel from microalgae. *Biotechnology advances*, 2007, 25(3): 294-306.
[49] Kovacevic V, Wesseler J. Cost-effectiveness analysis of algae energy production in the EU. *Energy Policy*, 2010, 38(10): 5749-5757.
[50] Grobbelaar J, Nedbal L and Tichy V. Influence of high frequency light/dark fluctuations on photosynthetic characteristics of microalgae photo acclimated to different light intensities and implications for mass algal cultivation. *Journal of Applied Phycology*, 1996, 8: 335–43.
[51] Phang SM, Miah MS, Yeoh BG and Hashim MA. Spirulina cultivation in digested sago starch factory wastewater. *Journal of Applied Phycology*, 2000, 12(3): 395–400
[52] Mullen CA, Boateng AA. Production and Analysis of Fast Pyrolysis Oils from Proteinaceous Biomass. *Bioenergy Resource*, 2011, 4: 303–311.
[53] Gouveia L, Cristina A. Microalgae as a raw material for biofuels production. *Journal Of Industrial Microbiology*, 2009: 269-274.
[54] Ju Y, Ryu C, Jeon J-ki et al. The characteristics of bio-oil produced from the pyrolysis of three marine macroalgae. *Bioresource Technology*, 2011, 102(3): 3512-3520.
[55] Grierson S, Strezov V, Ellem G, Mcgregor R and Herbertson J. Thermal characterisation of microalgae under slow pyrolysis conditions. *Journal of Analytical and Applied Pyrolysis*, 2009, 85(1-2): 118-123.
[56] Agblevor F, Beis S, Kim SS, Tarrant R, Mante NO. Biocrude oils from the fast pyrolysis of poultry litter and hardwood. *Waste management (New York, N.Y.)*, 2010, 30(2): 298-307.
[57] Chiavari G, Galletti G, Pyrolysis-gas chromatography/mass spectrometry of amino acids. *Journal of Analytical and Applied Pyrolysis*, 1992, 24: 123-137.
[58] Chiavari G, Fabbri D, Prati S. Gas chromatographic-mass spectrometric analysis of products arising from pyrolysis of amino acids in the presence of hexamethyldisilazane, Journal of.Chromatography A, 2001, 922: 235-241.

[59] Douda J, Basiuk V. Pyrolysis of amino acids: recovery of starting materials and yields of condensation products. *Journal of Analytical and Applied Pyrolysis*, 2000, 56(1): 113-121.
[60] Ratcliff M, Medley EE, Simmonds PG. Pyrolysis of amino acids. Mechanistic considerations. *The Journal of organic chemistry*, 1974, 39(11): 1481-90.
[61] White JL, Conner BT, Perfetti T, et al. Effect of pyrolysis temperature on the mutagenicity of tobacco smoke condensate. *Food and chemical toxicology : an international journal,* 2001, 39(5): 499-505.
[62] Sharma RK, Chan WG, Wang J, Waymack BE, Wooten JB, Seeman JI, Hajaligol MR. On the role of peptides in the pyrolysis of amino acids. *Journal of Analytical and Applied Pyrolysis*, 2004, 72: 153-163.
[63] Kanai Y, Wada O, Manabe S. Detection of carcinogenic glutamic acid pyrolysis products in cigarette smoke condensate. *Carcinogenesis,* 1990, 11(6): 1001-1003.
[64] Sharma RK, Chan WG, Seeman JI, Hajaligol MR. Formation of low molecular weight heterocycles and polycyclic aromatic compounds (PACs) in the pyrolysis of [alpha]-amino acids. *Journal of analytical and applied pyrolysis*, 2003, 66(1-2): 97–121.
[65] Roedern EGV, Lohof E, Hessler G, Hoffmann M, Kessler H. Synthesis and Conformational Analysis of Linear and Cyclic Peptides Containing Sugar Amino Acids. *Journal Of The Pharmaceutical Society Of Japan*, 1996, 7863(96): 10156-10167.
[66] Long DD, Tennant-Eyles RJ, Estevez JC, et al. Carbopeptoids: peptides and diketopiperazines incorporating the anomeric centre of mannopyranose. *Journal of the Chemical Society, Perkin Transactions 1*, 2001, (8): 807-813.
[67] Hwang IK, Go VLW, Harris DM, et al. Effects of cyclo (his – pro) plus zinc on glucose metabolism in genetically diabetic obese mice. *Science And Technology*, 2003: 317-324.
[68] Martins MB, Carvalho I. Diketopiperazines: biological activity and synthesis. *Tetrahedron*, 2007, 63(40): 9923-9932.
[69] Prasad C. Bioactive cyclic dipeptides. *Peptides*, 1995, 16(1): 151-164.
[70] Fischer PM. Diketopiperazines in Peptides and Combinatorial Chemistry, *Journal of Peptide Science*, 2003, 9: 9-35.
[71] Martins MB, Carvalho I. Diketopiperazines: biological activity and synthesis. *Tetrahedron*, 2007, 63: 9923-9932.
[72] You S, Park W, Lee HT, Ueom J, Jang, Lee K, Lim D. Synthesis and Conformational Study of Ser and Cys Derivatives of N-Hydroxy Diketopiperazine, *Bulletin of Korean Chemical Society*. 2007, 28 (12): 2414-18.

[72 b] Liu CL, Basile F. Intermolecular condensations products formed during the pyrolysis of peptide *J.Anal.Appl.Pyrol.* 2011, 92: 217-223.
[73] Boon JJ, J.W. de Leeuw. Amino acid sequence information in proteins and complex proteinaceous material revealed by pyrolysis-capillary gas chromatography –low and high resolution mass spectrometry. *J.Anal.Appl.Pyrol.* 1987, 11: 313-327.
[74] Fabbri D, Adamiano A, Torri C. Pyrolysis of proteins in the presence of active inorganic solids. *18th European Biomass Conference & Exhibition. From Research to Industry and Markets*. J.Spitzer et al. Eds. Lyon, Fr. 3-7 Maggio 2010. ISBN: 978-88-89407-56-5. Firenze: ETA - Florence Renewables Energy, pp.1498-1500.
[75] Ginz M, Engelhardt UH. Identification of new diketopiperazines in roasted coffee, *Eur.Food Res. Technol*. 2001, 213: 8-11.
[76] Chen YH, Liou SE, Chen CC. Two-step mass spectrometric approach for the identification of diketopiperazines in chicken essence, *Eur.Food Res. Technol*. 2004, 218: 589-597.
[77] Chen MZ, Dewis ML, Kraut K, Merritt D, Reiber L, Trinnaman L, Da Costa NC. 2,5-Diketopiperazines (Cyclic Dipeptides) in Beef: Identification, Synthesis, and Sensory Evaluation, *Journal of.Food Science.* 2009, 74: C100-C105.
[78] Hansson KM, Samuelsson J. Formation of HNCO, HCN, and NH3 from the pyrolysis of bark and nitrogen-containing model compounds, *Combus.Flame*. 2004, 137: 265–277.
[79] Giuntoli J, Gout J, Verkooijen AHM, W. de Jong, Characterization of Fast Pyrolysis of Dry Distiller's Grains (DDGS) and Palm Kernel Cake Using a Heated Foil Reactor: Nitrogen Chemistry and Basic Reactor Modeling. *Ind.Eng.Chem.Res*. 2011, 50: 4286-4300.
[80] Hendricker AD, Voorhees KJ. Amino acid and oligopeptide analysis using Curie-point pyrolysis mass spectrometry with in-situ thermal hydrolysis and methylation: mechanistic considerations, *J.Anal.Appl.Pyrol*. 1998, 48: 17-33.
[81] Gallois N, Templier J, Derenne S. Pyrolysis-gas chromatography-mass spectrometry of the 20 amino acids in the presence of TMAH. *J.Anal.Appl.Pyrol*. 2007, 80: 216-230.
[82] Choi SS, Ko JE. Dimerization reactions of amino acids by pyrolysis. *J.Anal.Appl.Pyrol*. 2010, 89: 74-86.
[83] Smith GG, Reddy GS, Boon JJ. Gas Chromatogrphic-Mass Spectrometric Analysis of the Curie-poit Pyrolysis Products of Some Dipeptides and their Diketopiperazines, *J.Chem.Soc.Perkin Trans. II*, 1988: 203-211.
[84] Svec HJ, Junk GA. The Mass Spectra of Dipeptides, *J.Am.Chem.Soc*. 1964, 86: 2278-2282.
[85] Hendricker AD, Voorhees KJ. An investigation into Curie-point pyrolysis-mass spectrometry of glycyl dipeptides, *J.Anal.Appl.Pyrol*. 1996, 36: 51-70.

[86] Noguerola AS, Murugaverl B, Voorhees KJ. An Investigation of Dipeptides Containing Polar and Nonpolar Side Groups by Curie-Point Pyrolysis Tandem Mass Spectrometry. *J.Am.Soc.Mass Spectrom*. 1992, 3: 750-756.
[87] Voorhees KJ, Zhang W, Hendricker AD, Murugavrel B. An investigation of the pyrolysis of oligopeptides by Curie-point pyrolysis-tandem mass spectrometry. *J.Anal.Appl.Pyrol.* 1994, 30: 1-16.
[88] Stankiewicz BA, Hutchins JC, Thompson R, Briggs DEG, Evershed RP. Assessment of Bog-body Tissue Preservation by Pyrolsyis-Gas Chromatography/Mass Spectrometry, *Rapid Commun.MassSpectrom.* 1997, 11: 1884-1890.
[89] Johnstone RAW, Povall TJ. Methods of peptide sequencing. Part I. Conversion of Oligopeptides into Cyclic Dipeptides: a Gas Chromatographic-Mass spectrometric Study. *JCS Perkin I,* 1975: 1297-1300.
[90] Pierce AE. Silylation of organic compounds. A technique for gas-phase analysis. Ch. 4. Theoretical aspects of silylation. 4.4 The special case of N- vs. O- silylation. Pp. 63-71. *Pierce Chemical Company. Rockford, Illinois,1968.*
[91] Meetani MA, Zhaid OK, ConlonJM. Investigation of the pyrolysis products of methioniner-enkephalin-Arg-Gly-Leu using liquid chromatography-tandem mass spectrometry. *J.Mass Spectrom.* 2010, 45: 1320-1331.
[92] Schumacher JN, Green CR, Best FW, Newel1 MP. Smoke Composition. An Extensive Investigation of the Water-Soluble Portion of Cigarette Smoke, *J. Agric. Food Chem*. 1977, 25: 310-320.
[93] Richmond-Aylor A, Bell S, Callery P, Morris K. Thermal Degradation Analysis of Amino Acids in Fingerprint Residue by Pyrolysis GC–MS to Develop New Latent Fingerprint Developing Reagents. *Journal of Forensic Sciences*, 2007, 52 (2): 380-2.
[94] Wang Z. REACTION MECHANISMS OF HYDROTHERMAL LIQUEFACTION OF MODEL. 2011, PhD Thesis, University of Illinois. Available online at: https://www.ideals.illinois.edu/bitstream/handle/2142/26090/Wang_Zhichao.pdf?sequence=1
[95] Fabbri D, Adamiano A, Torri C. Pyrolysis of proteins in the presence of active inorganic solids. *18th European Biomass Conference & Exhibition. From Research to Industry and Markets*. J.Spitzer et al. Eds. Lyon, Fr. 3-7 Maggio 2010. ISBN: 978-88-89407-56-5. Firenze: ETA - Florence Renewables Energy, pp.1498-1500.
[96] Kurata S, Ichikawa K. Identification of small bits of natural leather by pyrolysis gas chromatography/mass spectrometry, *Bunseki Kagaku.* 2008, 57: 563-569.

[97] Wang JH, Quan CS, Qi XH, Li X, Fan SD. Determination of diketopiperazines of *Burkholderiacepacia* CF-66 by gas-chromatography mass spectrometry, *Anal. Bioanal. Chem.* 2010, 396: 1773-1779.
[98] Chisti Y. Biodiesel from microalgae beats bioethanol. *Trends in biotechnology*. 2008;26(3):126-31.
[99] Lehmann J. *Biochar for environmental management.* Earthscan
[100] Gudin C, Bernard A, Chaumont DT et al. *World Biotech. Rep.* 1984, 1: 541.
[101] Banerjee A, Sharma R, Chisti Y, Banerjree UC. *Critical Reviews in Biotechnology*. 2002, 22: 245-279.
[102] Mulbry W, Kondrad S, Buyer J, Luthria DL. Comparison of several methods for effective lipid extraction from microalgae. *J Am Oil ChemSoc.* 2009, 86: 909-915.
[103] Graham LE, Wilcox LW, Graham JM. 2000. *In Pearson Hall, Benjamin Cummings* (ed), *Algae*. San Francisco, CA.
[104] Fabbri D, Bevoni V, Notari M, Rivetti F. *Fuel*. 2007, 87: 690–697.
[105] Ross M. *Mineralogy Rev. Miner*. 9A: 1981: 279
[106] Wicks J, Mineralogy, chemistry and crystallography of chrysotile asbestos. In R. L. Ledoux, Ed., Mineralogical Techniques of Asbestos Determination, 35-78, Mineral Assoc. Canada, Montreal Quebec.
[107] Viti C, Mellini M. *Eur. J. Mineral*. 1997, 9: 585.
[108] Yada K, *Acta Crystallogr., Sect A*, 1971, 27: 659-664.
[109] Whittaker EJW, Wicks FJ. *J. Am. Mineral.* 1970, 55: 1025-1047.
[110] Stroink G, Hutt D, Lim D, Dunlap RA. *IEEE Trans. Magnetics*, 1985, 21: 2074-2076.
[111] Schreier H. In Asbestos in the Natural Environment, *Elsevier: New York.* 1989, 159.
[112] Kamp DW, Weitzman SA. The molecular basis of asbestos induced lung injury, *Thorax*. 1999 54: 638-652.
[113] Fubini B, Otero-Aréan C. Chemical aspects of the toxicity of inhaled mineral Dusts, *Chem. Soc. Rev.* 1999, 28: 373-381.
[114] Jurinski J, Rimstidt JD, *Am. Mineral*. 2001, 86: 392 – 399.
[115] Davis JM, Addison J, Bolton RE, Donaldson K, Jones AD, Smith T, *Br. J. Exp. Pathol.* 1986, 67: 415 –430.
[116] Miller K, *Crit. Rev. Toxicol.* 1978, 5: 319 –354.
[117] Valerio F, De Ferrari M, Ottaggio L, Repetto E, Santi L, *Mutat. Res.* 1980, 122: 397 – 402.
[119] Kamp DW, Panduri V, Weitzman SA, Chandel N, *Mol. Cell. Biochem.* 2002, 234–235, 153 – 160.

[120] Wu J, Liu W, Koenig K, Idell S, Broaddus VC, *Am. J. Physiol*. 2000, 279: 916–923.
[121] McLachlan D, Walker JE, *J. Mol. Biol.* 1977, 112: 543 –548.
[122] Brown JR, Shockley P. Lipid–Protein Interactions Vol. 1 (Eds.:P. Jost, O. H. Griffith), Wiley, New York, 1982, pp. 25 –68.
[123] He XM, Carter DC, *Nature* 1992, 358: 209 – 215.
[124] Sugio S, Kashima A, Mochizuki S, Noda M, Kobayashi K, Protein Eng. 1999: 439 – 446.
[125] Pierini F, Foresti E, Fracasso G, Lesci IG and Roveri N. Potential Technological Applications of Synthetic Geomimetic Nanotubes. *Isr.J. Chem*. 2010,50,484-49
[126] Falini G, Foresti E, Lesci IG and Roveri N. Structural and morphological characterization of synthetic chrysotile single crystals. *Chem. Commun.* 2002, 14: 1512–1513.
[127] Falini G, Foresti E, Gazzano M, Gualtieri A F, Leoni M, Lesci I G & Roveri N. Tubular-shaped stoichiometric chrysotile nanocrystals. *Chem. Eur. J.*2004, 10: 3043–3049.
[128] Gazzano E, Foresti E, Lesci IG, Tomatis M, Riganti C, Fubini B, Roveri N, Ghigo D, Pharmacology, 2005, 206(3): 356.
[129] Kamp DW, Weitzman SA. The molecular basis of asbestos induced lung injury *Thorax* 1999, 54: 638-652.
[130] Xu L, Wu J, Santella RM, Hei TK, Cancer. Res. 59 5922-5926 1999
[131] Falini G, Foresti E, Lesci IG, Lunelli B, Roveri N and Sabatino P. Bovine serum albumin interaction with chrysotile: spectroscopic and morphological studies. *Chem. Eur. J.* 2006, 12: 1968–1974.
[132] Artali R, Del Pra A, Foresti E, Lesci IG, Roveri N and Sabatino P. Adsorption of human serum albumin on the chrysotile surface: a molecular dynamics and spectroscopic investigation. *J. R. Soc. Interface*, 2008, 5: 273–283
[133] Sabatino P, Casella L, Granata A, Iafisco M, Lesci GI, Monzani E and Roveri, N. Synthetic chrysothile nanocrystals as a reference standard to investigate surface induced serum albumin structural modifications. *J. Coll. Int. Sci.* 2007, 314: 389–397.
[134] Foresti E, Hochella MF, Kornishi H, Lesci IG, Madden AS, Roveri N and Xu H. *Adv. Funct. Mater.* 2005, 15: 1009-1016.
[135] Piperno S, Kaplan-Ashiri I, Cohen SR, Popovitz-Biro R, Wagner HD, Tenne R, Foresti E, Lesci IG and Roveri N, *Adv. Funct. Mater.* 2007, 17: 3332–3338.
[136] Gazzano E, Turci F, Foresti E, Putzu MG, Aldieri E, Silvagno F, Lesci IG, Tomatis M, Riganti C, Romano C, Fubini B, Roveri N and Ghigo D. Iron-loaded synthetic chrysotile: a new model solid for studying the role of iron in asbestos toxicity. *Chem. Res. Toxicol.* 2007, 20: 380–387.

[137] Kamp DW, Graceffa P, Prior WA, Weitzman SA. The role of free radicals in asbestos-induced diseases. *Free Radic. Biol. Med.*1992 12: 293–315.
[138] Hardy JA, Aust AE. Iron in asbestos chemistry and carcinogenicity, *Chem. Rev.* 1995, 95: 97–118.
[139] Kamp DW, Weitzman SA. The molecular basis of asbestos induced lung injury, *Thorax* 1999, 54: 638–652.
[140] Selikoff J, Lee DHK, "Asbestos and Disease" Academic Press, New York, 1978.
[141] Borghi E, Occhiuzzi M, Foresti E, Lesci IG, Roveri N. Spectroscopic characterization of Fe-doped synthetic chrysotile by EPR, DRS and magnetic susceptibility measurements. *Physical Chemistry Chemical Physics*. 2010, 12(1): 227-238.
[142] Turci F, Tomatis M, Lesci IG, Roveri N, and Fubini B.The Iron-Related Molecular Toxicity Mechanism of Synthetic Asbestos Nanofibres: A Model Study for High-Aspect-Ratio *Nanoparticles. Chem. Eur. J.* 2011, 17, 350 – 358.
[143] Ligth WG, Wei ET. *Environ. Res.* 1977, 13: 135.
[144] Iafisco M, Sabatino P, Lesci IG, Prat M, Rimondini L, Roveri N. *Colloids and Surfaces B: Biointerfaces.* 2010, 81: 274–284.
[145] Johnson WR, Kang JC. Mechanisms of Hydrogen Cyanide Formation from the Pyrolysis of Amino Acids and Related Compounds. *Journal of Organic Chemsitry*. 1971, 780(1): 5-8.
[146] Rimola A, Sodupe M, Ugliengo P. Affinity Scale for the Interaction of Amino Acids with Silica Surfaces. *Society*. 2009: 5741-5750.
[147] Fabbri D, Vassura I. Evaluating emission levels of polycyclic aromatic hydrocarbons from organic materials by analytical pyrolysis. *Journal of Analytical and Applied Pyrolysis*. 2006;75(2): 150-158.
[148] Knicker H, Rõâo JC, Hatcher PG, Minard RD. Identification of protein remnants in insoluble geopolymers using TMAH thermochemolysis / GC ± MS. *Organic Geochemistry*. 2001, 32: 397-409.
[149] Miles CA and Ghelashvili M. Polymer-in-a-box mechanism for the thermal stabilization of collagen molecules in fibers. *Biophysical Journal*. 1999, 76: 3243–52.
[150] Weiner S, Traub W. Organization of hydroxyapatite crystals within collagen fibrils. *FEBS letters*. 1986, 206(2): 262-6.
[151] Semal P and Orban R. Collagen Extraction from Recent and Fossil Bones : Quantitative and Qualitative Aspects. *Bone*. 1995: 463-467.
[152] Haddy A,and Hansen A. Research Notes and Application Reports Nitrogen and Fluorine Dating of Moundville Skeletal Samples. *Archaeometry*. 1982, 24 (1): 37–44,

[153] Bailey J, Paul RG and Knott L. Mechanisms of maturation and ageing of collagen. *Mechanisms of ageing and development*. 1998, 106(1-2): 1-56.
[154] Collins MJ, Nielsen-Marsh CM, Hiller J, et al. The survival of organic matter in bone: a review. *Archaeometry*. 2002, 44(3): 383-394.
[155] Wang X, Shen X, Li X, Agrawal CM. Age-related changes in the collagen network and toughness of bone. *Bone*. 2002, 31(1):1-7.
[156] Rho JY, Zioupos P, Currey JD, Pharr GM. Microstructural elasticity and regional heterogeneity in human femoral bone of various ages examined by nano-indentation. *Journal of biomechanics*. 2002, 35(2): 189-98.
[157] Kronick PL, and Cooke P. Thermal stabilization of collagen fibres by calcification, *Connective Tissue Research*, 1996, 33: 275–82
[158] Piga G, Santos-Cubedo A, Moya Solà S, et al. An X-ray Diffraction (XRD) and X-ray Fluorescence (XRF) investigation in human and animal fossil bones from Holocene to Middle Triassic. *Journal of Archaeological Science*. 2009, 36(9):1857-1868.
[159] Semal P, Rougier H, Crevecoeur I, et al. New data on the late Neandertals: direct dating of the Belgian Spy fossils. *American journal of physical anthropology*. 2009, 138(4): 421-8.
[160] Budrugeac P, Emandi A. The use of thermal analysis methods for conservation state determination of historical and/or cultural objects manufactured from lime tree wood. *Journal of Thermal Analysis and Calorimetry*. 2010, 101(3): 881-886.
[160] Lozano L, Pena-Rico M, Heredia A. Thermal analysis study of human bone. *Journal of materials*. 2003, 8:4777-4782.
[161] Todd TW. Age changes in the pubic bone. I. The male white pubis. *American Journal of Physical Anthropology*. 1920, 3 (3): 285–334.
[162] Ozaslan A, Işcan MY, Ozaslan I, Tuğcu H, Koç S. Estimation of stature from body parts. *Forensic science international*. 2003, 132(1): 40-5.
[163] Nudelman F, Pieterse K, George A, et al. The role of collagen in bone apatite formation in the presence of hydroxyapatite nucleation inhibitors. *Nature Materials*. 2010, 9(October): 9-14.
[164] Weiner S, Wagner HD. THE MATERIAL BONE: Structure-Mechanical Function Relations. *Annual Review of Materials Science*. 1998, 28(1): 271-298.
[165] Glimcher MJ. The possible role of collagen fibrils and collagen-phosphoprotein complexes in the calcification of bone in vitro and in vivo. *Biomaterials*, 1990, 11: 7-10.
[166] Lee DD, Glimcher MJ. Three-dimensional spatial relationship between the collagen fibrils and the inorganic calcium phosphate crystals of pickerel (Americanus americanus) and herring (Clupea harengus) bone. *Journal of Molecular Biology*. 1991,7 (3): 487–501.

[167] Fratzl P, Weinkamer R. Nature's hierarchical materials. *Progress in Materials Science*. 2007, 52(8): 1263-1334.
[168] Weiner S, Traub W, Wagner HD. Lamellar Bone : Structure – Function Relations. *Journal of Structural Biology*. 1999, 255: 241-255.
[169] Popescu C, Budrugeac P, Wortmann F-J, et al. Assessment of collagen-based materials which are supports of cultural and historical objects. *Polymer Degradation and Stability*. 2008, 93(5): 976-982.
[170] Sebastián I, Viallon-Fernandez C, Tournayre P, et al. Evaluation of collagen and lipid contents and texture of meat by Curie point pyrolysis–mass spectrometry. *Journal of Analytical and Applied Pyrolysis*. 2004, 72(2): 203-208.
[171] Andreotti A, Bonaduce I, Colombini MP, et al. Combined GC / MS Analytical Procedure for the Characterization of Glycerolipid , Waxy , Resinous , and Proteinaceous Materials in a Unique Paint Microsample of lipids , waxes , proteins , and resinous materials in the. *Society*. 2006, 78(13):4490-4500.
[172] Onishi A, Thomas PS, Stuart BH, Guerbois JP, Forbes S. TG-MS CHARACTERISATION OF PIG BONE IN AN INERT ATMOSPHERE. *Journal Of Thermal Analysis*. 2007, 88: 405-409.
[173] Raja S, Thomas PS, Stuart BH, Guerbois JP, O'Brien C. The estimation of pig bone age for forensic application using thermogravimetric analysis. *Journal of Thermal Analysis and Calorimetry*. 2009, 98(1): 173-176.
[174] Weiner S and Bar-Yosef O. States of preservation of bones from prehistoric sites in the Near East: a survey. *Journal of Archaeological Science*, 1990, 17: 187–196.
[175] Bartsiokas A, and Middleton AP. Characterization and dating of recent and fossil bone by X-ray diffraction. *Journal of Archaeological Science*, 1992, 19: 63–72.
[176] Stankiewicz B, Hutchins JC, Thomson R, Briggs DE, Evershed RP. Assessment of bog-body tissue preservation by pyrolysis-gas chromatography/mass spectrometry. *Rapid communications in mass spectrometry*. 1997;11(17): 1884-90.
[177] Cassab GI. Plant Cell Wall Proteins. *Annual review of plant physiology and plant molecular biology*. 1998, 49: 281-309.
[178] 1. DePaula C a, Truncale KG, Gertzman a a, Sunwoo MH, Dunn MG. Effects of hydrogen peroxide cleaning procedures on bone graft osteoinductivity and mechanical properties. *Cell and tissue banking*. 2005, 6(4): 287-98.
[179] Person A, Bocherens H, Mariotti A and Renard M. Diagenetic evolution and experimental heating of bone phosphate. *Palaeogeography, Palaeoclimatology, Palaeoecology.* 1996, 126: 135–49.

[180] Klug HP, Alexander LE. X-ray diffraction procedures for polycrystalline and amorphous materials. New York: Wiley-Interscience; 1974.
[181] Altomare A, Burla MC, Giacovazzo C, Guagliardi A, Molitemi AGG.; Polidori P, Rizzi R J. *Appl. Crystallogr*. 2001, 34: 392–399.
[182] Fabbri D, Adamiano A, Falini G, De Marco R and Mancini I. Analytical pyrolysis of dipeptides containing proline and amino acids with polar side chains. Novel 2,5-diketopiperazine markers in the pyrolysates of proteins. *Journal of Analytical and Applied Pyrolysis.* doi:10.1016/j.jaap.2012.02.001
[183] Bracewell JM, Robertson GW. Quantitative comparison of the nitrogen-containing pyrolysis products and amino acid composition of soil humic acids. *Journal of Analytical and Applied Pyrolysis.* 1984, 6 (1): 19–29.
[184] Smith RM, Shawkat SAK, and Hayes WP. Pyrolysis-gas chromatography of proline, hydroxyproline and related peptides. *Analyst*. 1980, 105: 1176-1181.
[185] Banciu MD, Simion A, Draghici C. Flow-vacuum pyrolysis of 5H-dibenzo [a , d] cyclohepten-5-one oxime and oxime. 2000, 53: 161-176.
[186] Ledesma EB, Kalish MA, Nelson PF, Wornat MJ, Mackie JC. Formation and fate of PAH during the pyrolysis and fuel-rich combustion of coal primary tar. *Fuel*. 2006, 79(2000): 1801-1814.
[187] Trueman C. Mineralogical and compositional changes in bones exposed on soil surfaces in Amboseli National Park, Kenya: diagenetic mechanisms and the role of sediment pore fluids. *Journal of Archaeological Science*. 2004, 31(6): 721-739.
[188] Mann, S. Biomineralization: Principles and Concepts in Bioinorganic Materials Chemistry; Oxford University Press: Oxford, 2001.
[189] Addadi L, Weiner S (1985) Interactions between acidic proteins and crystals: stereochemical requirements in biomineralization. *Proceedings of the National Accademy of Sciences of the United States of America.*
[190] Addadi L, Weiner S, Geva M. On how proteins interact with crystals and their effect on crystal formation. *Zeitschrift fur Kardiologie*, 2001, 90 Suppl 3: 92–98.
[191] Vymetal J, Slaby I, Spahr A, Vondrasek J and Lyngstadaas SP. Bioinformatic analysis and molecular modelling of human ameloblastin suggest a two-domain intrinsically unstructured calcium-binding protein, *Eur.J.Oral.Sci.* 2008, 116: 124–134.
[192] Delak K, Harcup C, Lakshminarayanan R, Sun Z, Fan Y, Moradian-Oldak J, Evans JS. The Tooth Enamel Protein, Porcine Amelogenin, Is an Intrinsically Disordered Protein with an Extended Molecular Configuration in the Monomeric Form. *Biochemistry*. 2009, 48(10): 2272–2281.

[193] Gibson JM, Popham JM, Raghunathan V, Stayton PS and Drobny GP. A solid-state NMR study of the dynamics and interactions of phenylalanine rings in a statherin fragment bound to hydroxyapatite crystals. *Journal of the American Chemical Society*, 2006, 128: 5364-5370.
[194] Amos FF, Evans JS. AP7, a partially disordered pseudo C-RING protein, is capable of forming stabilized aragonite in vitro. *Biochemistry*. 2009, 48: 1332-1339.
[195] Hunter J, O'Young BG, Karttunen M, Goldberg HA. The Flexible Polyelectrolyte Hypothesis of Protein−Biomineral Interaction. *Langmuir*, 2010, 26 (24): 18639–18646.
[196] Njegiä Džakula B, Brécevic L, Falini G, Kralj D. Calcite crystal growth kinetics in the presence of charged synthetic polypeptides. Crystal Growth & Design, 2009, 9: 2425-2434
[197] Erasmus J, Cook PA, Sweijd N. Internal shell structure and growth lines in the shell of the abalone Haliotis midae. *J. Shellfish Res.* 1994, 13: 493–501.
[198] Falini G, Sartor G, Fabbri D, Fermani S, Vergni P, Belcher AM, Stucky GD, Morse DE. The Interstitial Crystal-Nucleating Sheet in Molluscan Haliotis rufescens Shell: A Biopolymeric Composite. *Journal of Structural Biology*. 2011, 173(1): 128-137.
[199] Belcher AM, Wu XH, Christensen RJ, Hansma PK, Stucky GD, et al. Control of crystal phase switching and orientation by soluble mollusc-shell proteins. *Nature*, 1996, 381: 56–58.
[200] Munson TO, Fetterolf DD. Evidence for the formation of 2,4-imidazolidinediones and pyrrolidino[1,2a]-3,6-piperazinediones in human hair pyrolysate by pyrolysis-gas chromatography-mass spectrometry-mass spectrometry. *J.Anal.Appl.Pyrol.* 1987, 11: 15-24.
[201] Largeau C, Casadevall E, Berkaloff C, Dhamelincourt P. Sites of accumulation and composition of hydrocarbons in Botryococcus braunii. *Phytochemistry*, 1980, 19: 1043-51.
[202] Guillard RRL, Ryther JH. Studies of marine planktonic diatoms. I. Cyclotella nana Husted and Detonula confervacea Cleve. Can. J. *Microbiology*. 1962, 8: 229-239.
[203] Awile O, Krisko A, Sbalzarini IF,2, Zagrovic B. Intrinsically Disordered Regions May Lower the Hydration Free Energy in Proteins: A Case Study of Nudix Hydrolase in the Bacterium Deinococcus radiodurans. *PLoS Computational Biology*. 2010, 6(7).
[204] Mata TM, Martins A a., Caetano NS. Microalgae for biodiesel production and other applications: A review. *Renewable and Sustainable Energy Reviews*. 2010, 14(1): 217-232.
[205] Basiuk VA, Douda J. Pyrolysis of poly-glycine and poly- L -alanine : analysis of less-volatile products by gas chromatography / Fourier transform infrared spectroscopy / mass spectrometry. Journal of Analytical and Applied Pyrolysis. 2000, 55: 235-246.
[206] Wang DX, Liang MT, Tian GJ, Lin H, Liu HQ. A facile pathway to synthesize diketopiperazine derivatives. *Tetrahedron Letters*. 2002, 43(5): 865-867.

[207] Channiwala SA, Parikh PP. A unified correlation for estimating HHV of solid, liquid and gaseous fuels, *Fuel.* 2002, 81**:** 1051–1063

Acknowledgments

The research was partially conducted withn the MIUR PRIN 2007 (Nr. 2007498XRF_005) "Study of the mechanisms responsible for cytotoxicity and genotoxicity of silica nanoparticles of silica and nanomeric fibrous silicates having strictly controlled size, structure and composition". The research performed in paragraph 5.1 was supported by the Italian Ministry of Economic Development within the framework of the Program Agreement MiSE-CNR ''Ricerca di Sistema Elettrico".

I acknowledge Bioemco laboratories in Paris (UPMC-CNRS) and especially Sylvie Derenne, Joëlle Templier and Chrystelle Anquetil for hosting me and for supervising my work.

I would like to express my gratitude to all the professors, colleagues and students that contributed to the work presented in this thesis: Prof. Giuseppe Falini (Univerisity of Bologna, Department of Chemistry) for his precious help in experimental set-up and helpful discussions regarding protein structure and collagen preservation in bones, as well for XRD and FTIR analysis on archaeological samples, and for providing GP samples (paragraph 5.3 and 5.4), Prof. Maria Giovanna Belcastro for providing archaeological samples (paragraph 5.3), Prof. Ines Mancini (University of Trento) for NMR, ESI-MS and HPLC-MS analysis (chapter 4), Prof. Rossella Pistocchi for microalgae cultivation (paragraph 5.1), Prof. Luigi Gentiluci and Dr. Rossella De Marco (Univerisity of Bologna, Department of Chemistry) for tripeptides synthesis, Dr. Isidoro Giorgio Lesci (Univerisity of Bologna, Department of Chemistry) for synthesis and characterization of chrysotile nanofibers and for providing BSA/nanofibers adducts (paragraph 5.2), Prof. Barbara Bonelli (Polytechnic Univeristy of Torino) for SEM analysis of silica nanoparticles, Dr. Cristian Torri and Dr. Chiara Samorì (University of Bologna, CIRI) for their work in the field of microalgae characterization (paragraph 5.1), Dr. Danilo Malferrari (University of Bologna, CIRSA) for his precious advice on pyrolysis products separation (chapter 4), Dr. Giulia Samorì (University of Bologna, CIRSA) for providing microalgae samples, Giorgio Zattini, Helena Cordiani and Stefano Zannoni for their work on proteins pyrolysates characterization.

I would like to express my deepest gratitude to Prof. Daniele Fabbri, whose help, stimulating suggestions and encouragement helped me in all the time of research and writing of this thesis.

In the end, I would like to thank my family, my friends, and all those people who supported me with their love and comprehension.